2013

Manufacturing Of Single Solid Oxide Fuel Cells

Jonathan Torres-Caceres
University of Central Florida

STARS Citation

Torres-Caceres, Jonathan, "Manufacturing Of Single Solid Oxide Fuel Cells" (2013). *Electronic Theses and Dissertations, 2004-2019*. 2988.
https://stars.library.ucf.edu/etd/2988

MANUFACTURING OF SINGLE SOLID OXIDE FUEL CELLS

by

JONATHAN TORRES
B.S. University of Central Florida, 2011

A thesis submitted in partial fulfillment of the requirements
for the degree of Master of Science
in the Department of Mechanical & Aerospace Engineering
in the College of Engineering & Computer Science
at the University of Central Florida
Orlando, Florida

Summer Term
2013

Major Professor: Nina Orlovskaya

ABSTRACT

Solid oxide fuel cells (SOFCs) are devices that convert chemical energy into electrical energy and have the potential to become a reliable renewable energy source that can be used on a large scale. SOFCs have 3 main components; the electrolyte, the anode, and the cathode. Typically, SOFCs work by reducing oxygen at the cathode into O^{2-} ions which are then transported via the electrolyte to the anode to combine with a fuel such as hydrogen to produce electricity. Research into better materials and manufacturing methods is necessary to reduce costs and improve efficiency to make the technology commercially viable.

The goal of the research is to optimize and simplify the production of single SOFCs using high performance ceramics. This includes the use of 8mol% Y_2O_3-ZrO_2 (YSZ) and 10mol% Sc_2O_3-1mol%CeO_2-ZrO_2 (SCSZ) layered electrolytes which purport higher conductivity than traditional pure YSZ electrolytes. Prior to printing the electrodes onto the electrolyte, the cathode side of the electrolyte was coated with 20mol% Gd_2O_3-CeO_2 (GDC). The GDC coating prevents the formation of a nonconductive $La_2Zr_2O_7$ pyrochlore layer, which forms due to the interdiffusion of the YSZ electrolyte ceramic and the $(La_{0.6}Sr_{0.4})_{0.995}Fe_{0.8}Co_{0.2}O_3$ (LSCF) cathode ceramic during sintering. The GDC layer was deposited by spin coating a suspension of 10wt% GDC in ethanol onto the electrolyte. Variation of parameters such as time, speed, and ramp rate were tested. Deposition of the electrodes onto the electrolyte surface was done by screen printing. Ink was produced using a three roll mill from a mixture of ceramic electrode powder, terpineol, and a pore former. The pore former was selected based on its ability to form a uniform well-connected pore matrix within the anode samples that were pressed and sintered. Ink development involved the production of different ratios of powder-to-terpineol inks to vary the viscosity. The different inks were used to print electrodes onto the electrolytes to gauge print quality and consistency. Cells were produced with varying numbers of layers of prints to achieve a desirable thickness. Finally, the densification behaviors of the major materials used to produce the single cells were studied to determine the temperatures at which each component needs to be sintered to achieve the desired density and to determine the order of electrode application, so as to avoid over-densification of the electrodes. Complete cells were tested at the National Energy Technology Laboratory in Morgantown, WV. Cells were tested in a custom-built test stand under constant voltage at 800°C with 3% humidified hydrogen as the fuel. Both voltage-current response and impedance spectroscopy tests were conducted after initial startup and after 20 hours of operation. Impedance tests were performed at open circuit voltage and under varying loads in order to analyze the sources of resistance within the cell. A general increase in impedance was found after the 20h operation. Scanning electron micrographs of the cell microstructures found delamination and other defects which reduce performance. Suggestions for eradicating these issues and improving performance have been made.

This thesis is dedicated to my parents, Anibal and Sandra Torres, who have always inspired me to achieve more and have supported and guided me in my every decision. To my brother Anibal and his wife Leanne who always encourage me to keep on going but make me relax and have fun at the same time. Finally, to my fiancée Danielle Terry for her endless love, support, and boundless patience.

ACKNOWLEDGMENTS

This thesis is the result of Dr. Nina Orlovskaya's continued support and patience throughout the course of this project. I am grateful for having been given the opportunity to work on this project in an exciting area that I previously knew nothing of. Dr. Orlovskaya has always been available to answer any questions and point me in the right direction in my research, providing helpful suggestions or a good source when I was stuck during an experiment.

I would like to thank Kirk Gerdes, Shiwoo Lee, Gregory Hackett, and Harry Abernathy at the Department of Energy's (DoE) National Energy Technology Laboratory (NETL) in Morgantown, WV for their direct assistance in testing and analyzing complete single cells. I would like to thank the DoE and Oak Ridge Associated Universities for granting me the Mickey Leland Energy Fellowship which provided the opportunity to complete said testing at the NETL.

I would like to thank Dr. Yunjun Xu and Dr. Tuhin Das for serving on my thesis committee.

Finally, I would like to thank my family, friends, and colleagues who may have supported or assisted me at one time or another during the duration of the project. Their continued support has been vital to the completion of this thesis.

This project was funded by NSF projects DMR-0748364 and CMMI-1030833.

TABLE OF CONTENTS

LIST OF FIGURES

LIST OF TABLES

CHAPTER 1: INTRODUCTION

Solid Oxide Fuel Cells (SOFCs) present a clean, efficient source of producing renewable energy. Through the use of SOFCs, chemical energy can be converted directly to electrical energy with little or no harmful emissions depending on the fuel used and a very high efficiency, up to around 70% in a combined cycle system, and have been reported up to 90% efficiency with heat recovery [1-3]. This is especially valuable when compared to the efficiency and emissions output of other systems which convert chemical energy to electrical energy with the use of an intermediate combustion step, such as internal combustion engines or turbines. Eliminating the need for combustion or mechanical conversion steps, is what gives SOFCs much higher efficiencies than typical systems such as internal combustion engines, as illustrated in Figure 1. The lack of moving parts also eliminates the problem of energy-robbing friction which exists in mechanical energy conversion devices.

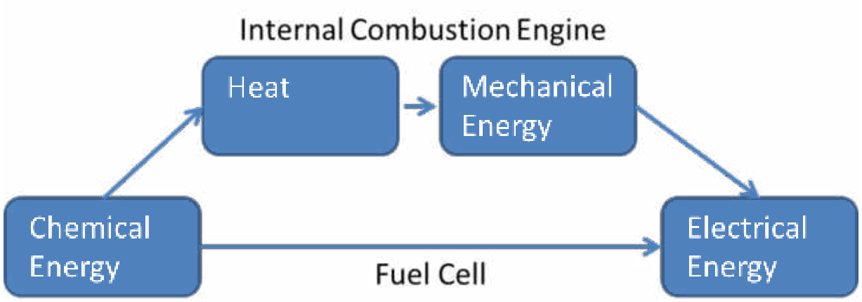

Figure 1 - Internal combustion engine vs. fuel cell energy conversion process [4].

Fuel cells are electrochemical energy conversion devices composed of three main parts which, when supplied with a gaseous fuel and an oxidant gas, generate electricity from chemical energy [1, 5]. Solid oxide fuel cells are composed of (a) the anode where the fuel oxidation reaction occurs, (b) the electrolyte which conducts oxygen ions, and (c) the cathode where the oxygen reduction reaction takes place. Figure 2 shows the schematic of a typical SOFC system. Although the ideal fuel for SOFCs is hydrogen, one of the main advantages of SOFCs over other types of fuel cells is their adaptability to use various fuels and withstand some level of impurities [2].

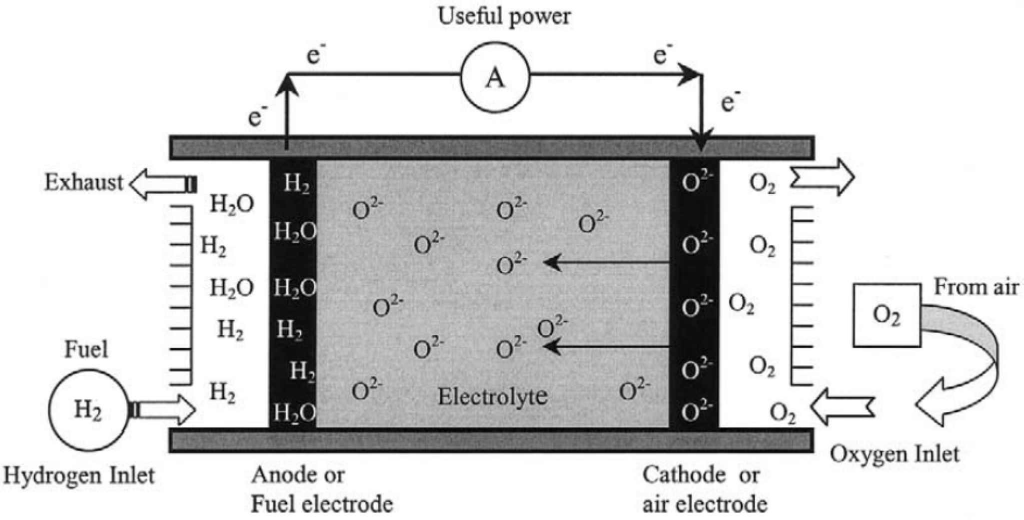

Figure 2 - Diagram of an oxygen-ion conducting SOFC [1].

Oxygen, or air, is supplied to the cathode side and a fuel, such as hydrogen, is supplied to the anode side. The oxygen gas flows through the pores of the cathode to reach the interface with the electrolyte. Here, at the triple-phase boundary (TPB) consisting of electronically conductive cathode such as a $LaMnO_3$ based perovskite, pores, and electrolyte, the oxygen which flows on the cathode surface is split into oxygen ions by way of reduction reaction where molecular O_2 is reduced into O^{2-} ions using electrons provided by the external circuit [6]. For mixed ionic electronic conductive (MIEC) cathode materials, such as $La_{1-x}Sr_xCo_{1-y}Fe_yO_{3-\delta}$ (LSCF), the TPB is extended beyond the cathode-electrolyte interface to the bulk of the cathode so that the electrochemical reaction rates are increased due to an increase in surface area of the reactive sites, increasing the overall performance of the cell [7]. The oxygen ions are transported through the dense electrolyte to reach the TPB at the anode side where the electron-producing electrochemical reaction occurs. Hydrogen, or another fuel such as methane or CO, is supplied to the anode and flows through the anode pores to be oxidized while combining with the oxygen ions to create water, in the case where hydrogen is used, and free electrons which are the source of the electricity supplied to the external circuit. The half reactions listed as Equations 1-3 explain the overall operating principles of a hydrogen-oxygen SOFC.

The oxidation half-reaction at the anode:

$$H_2 + O^{2-} \rightarrow H_2O + 2e^- \tag{1}$$

The reduction half-reaction at the cathode:

$$O_2 + 4e^- \rightarrow 2O^{2-} \tag{2}$$

The net reaction:

$$H_2 + \tfrac{1}{2}O_2 \rightarrow H_2O \tag{3}$$

Finally, the last step is to remove the products of the reaction, such as the water created on the anode side plus any unused reactants from either electrode. Figure 3 shows a schematic of the reaction sites in the anode, these are sites where connectivity of the electronic conductor, the electrolyte and the gas phase form the TPB.

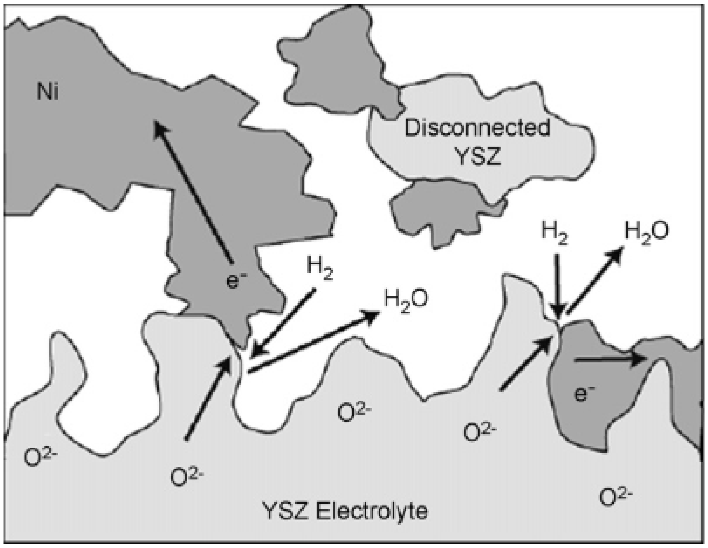

Figure 3 - Schematic of the popular nickel/yttria-stabilized zirconia (YSZ) anode three-phase boundary reaction sites [6].

Solid oxide fuel cells employ stable all-solid-state ceramic materials to electrochemically convert chemical energy into electrical energy [1]. Due to ionic conduction being a thermally activated process, the temperature at which the cell is operated is determined by the materials chosen for the electrolyte and at what temperature it is ionically conductive [8]. For SOFCs, this is typically in the range of 800-1000°C, though the trend is generally to aim for lower operating temperatures to reduce costs with the use of metallic interfaces and the successful operation of some SOFCs at temperatures of 350-650°C has been reported [9]. The requirements for the necessary attributes of each component of the SOFC are listed in Table 1. The use of solid oxides at high temperatures provides certain advantages over other types of cells, such as avoiding the need to use corrosive liquids like those used in the electrolytes of alkaline, phosphoric acid, or molten carbonate fuel cells, providing internal reforming of fuel, and production of high quality heat for subsequent use [1, 8, 10]. The need for high operating temperatures, however, makes it difficult to find suitable materials which have the thermal and chemical stability properties which are necessary for use in SOFC operating environments and also meet the component requirements noted in Table 1 [10]. The next and even more limiting reason is that the compatibility between the different materials can severely impact the performance of the fuel cell. A severe mismatch in thermal expansion coefficients between the electrolyte and cathode, for example, can lead to cracking of the cathode during sintering [1], or a weak bond between the cathode and electrolyte which could lead to delamination.

Table 1 - Required attributes of each SOFC component.

Component	Attributes	Porosity
Anode	High electronic conductivity High catalytic activity for fuel oxidation	Porous
Electrolyte	High ionic conductivity Negligible electronic conductivity High stability in both oxidizing and reducing environments	Fully dense
Cathode	High electronic conductivity Good ionic conductivity (mixed conducting perovskite) High catalytic activity for oxygen reduction	Porous

For SOFCs there exist three different configurations in which self-supported cells may be manufactured. These are, as shown in Figure 4, electrolyte supported, cathode supported, and anode supported.

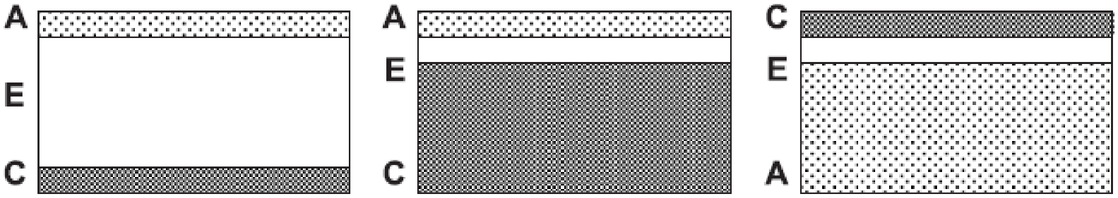

Figure 4 - Typical planar SOFC support structures. From left to right: electrolyte supported, cathode supported, anode supported [5].

There are certain advantages and disadvantages to each type. Table 2 below summarizes the most important of the properties which are important to consider when manufacturing SOFCs.

Table 2 - Properties of different SOFC support configurations [11].

Support	Advantages	Disadvantages
Anode	Highly conductive anode, lower operating temperature due to thin electrolyte	Potential anode reoxidation, gas transport can be impeded by thickness of anode
Electrolyte	Strong structural support, less susceptible to failure from anode reoxidation or cathode reduction	Higher resistance due to thick electrolytes, higher operating temperatures required to minimize ohmic losses
Cathode	No oxidation issues, lower operating temperature due to thin electrolyte	Lower conductivity, potential cathode reduction, gas transport can be limited by thickness of cathode

The main goal of this work is to establish and refine a manufacturing process for building electrolyte-supported Solid Oxide Fuel Cells designed around a novel electrolyte design developed by Yan Chen, a PhD graduate from our research group at the University of Central Florida (UCF). The manufacturing process established within this work is based on the most reliable and popularly used SOFC production technologies and methods available today. These processes have been adapted and refined for use with the materials chosen for production with an emphasis on reliability and reproducibility of methods so that the advancement of SOFCs may continue for years to come as researchers within the project change. Chapter 2 of this work will focus on a review of SOFC concepts and current technology, along with material properties and some popularly used manufacturing methods for each component from literature. Chapter 3 will divulge the details of the experimental methods and iterations for establishing each procedure in the multi-step cell production process. Chapter 4 will include the results and discussions of said iterations, followed by some suggestions for future work and conclusions in Chapters 5 and 6, respectively.

CHAPTER 2: LITERATURE REVIEW

As it was described in the introduction, SOFCs consist of three elements, namely the anode, electrolyte, and cathode. In this chapter we will provide an overview of each of these elements, their functions, the materials they are made of, their properties, and performance, as well as the commonly used manufacturing methods.

2.1 Anode

2.1.1 Function

Fuel oxidation occurs at the anode side of the cell as oxygen anions are transported from the cathode to the anode through the electrolyte, driven by the difference in oxygen chemical potential between the air and fuel environments of the cathode and anode [6]. The SOFC anode, therefore, is responsible for facilitating oxidation of the fuel and transportation of the electrons released in the fuel oxidation reaction from the electrode to the external circuit, along with allowing diffusion of the fuel gas to the interface of the anode and electrolyte and reaction products away from it [12]. Thus, the required properties for the SOFC anode, repeated from Table 1, are high electronic conductivity, high catalytic activity for fuel oxidation, chemical and thermal stability in the reducing environment, compatibility with the electrolyte, high porosity, and good adherence to the electrolyte. Conventional anodes are typically composed of ceramic and metal composites (cermet), with the universally accepted standard being nickel/yttria-stabilized zirconia-based (Ni/YSZ) cermet.

2.1.2 Materials

2.1.2.1 Metals

Theoretically, the requirements for operation of an SOFC anode can be met by pure porous metal, such as Ni, which has shown a high activity towards electrochemical oxidation of H_2 [13] and is, at the same time, electronically conductive. In practice, however, it has been shown that pure metal electrodes such as that composed of Ni will not work due to a relatively low sintering temperature which will lead to aggregation of Ni due to grain growth during operation of the cell and a corresponding reduction in porosity [12, 14]. The rapid grain growth of Ni and reduction in porosity will lead to a significant decrease in existing TPB sites at which the electrochemical reaction occurs and also impose limitations on fuel delivery to the reaction sites.

2.1.2.2 Cermets

Therefore, the function of the YSZ in the traditional Ni/YSZ cermet matrix is both structural and electrochemical. Structurally, the addition of YSZ to Ni provides a skeleton to separate Ni particles and prevent grain growth and subsequent pore closure [12]. Additionally, the YSZ helps to closely match the thermal-expansion coefficients of the anode and electrolyte, preventing cracking and delamination from thermal cycling [15], and helps to form a much stronger bond between the anode and conventional YSZ electrolytes, as the YSZ in the anode can sinter with the YSZ of the electrolyte leading to high structural stability. The presence of a well-connected matrix of YSZ particles within the anode also provides for an extension of the TPB away from the interface with the electrolyte into the bulk of the anode, significantly enhancing activity by extending the two-dimensional reaction zone into a three-dimensional one [14].

Figure 5 shows the electrochemical oxidation half reaction $H_2 + O^{2-} \rightarrow H_2O + 2e^-$ occurring at the triple-phase boundary within the anode. The YSZ acts as an ionic conductor for the oxygen ion to travel to the TPB and the Ni acts as a catalyst to promote fuel oxidation and then as an electrical conductor to guide the free electrons away from the interface to the external circuit.

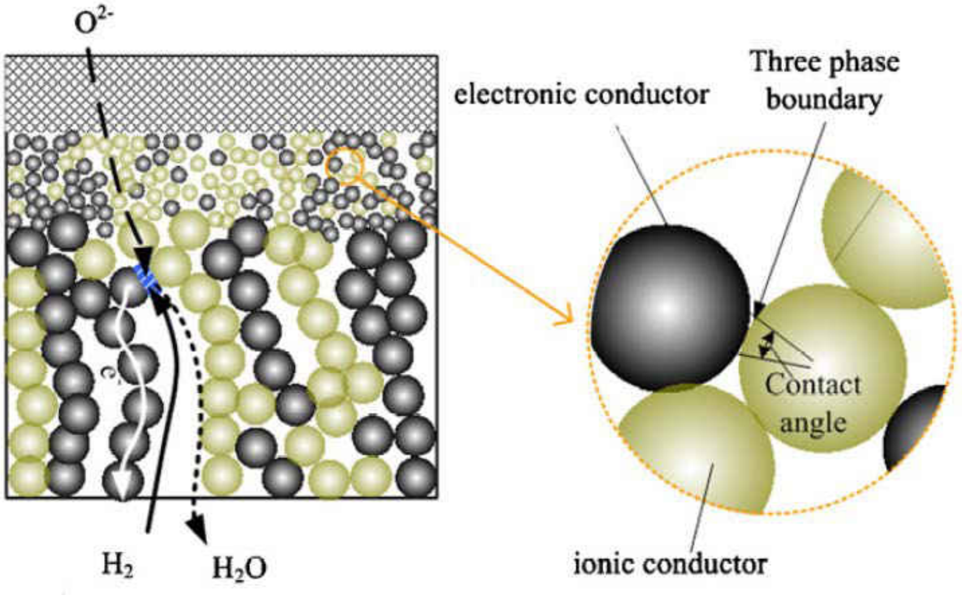

Figure 5 - Electrochemical reaction at the anode and structure of the YSZ (gold) and Ni (dark grey) matrices within it (electron flow shown as white arrow)[16].

As widely accepted as Ni/YSZ cermet is for its excellent hydrogen oxidation activity, good conductivity, and structural soundness, it does have drawbacks. Although the YSZ limits the growth of Ni agglomerates, Ni grain growth and agglomeration can continue at high temperatures during long-term performance and degrade performance, and the Ni/YSZ cermet exhibits low oxidation/reduction cycling stability [15, 17]. Figure 6 shows the growth and agglomeration of large Ni into a large particle in a 70vol% Ni/ 30vol% YSZ anode after sintering for 2000h in moist 10% H_2/ 90% N_2 at 1000°C, which demonstrates the fact that Ni agglomeration can still occur when using a Ni/YSZ cermet, rather than pure Ni [18].

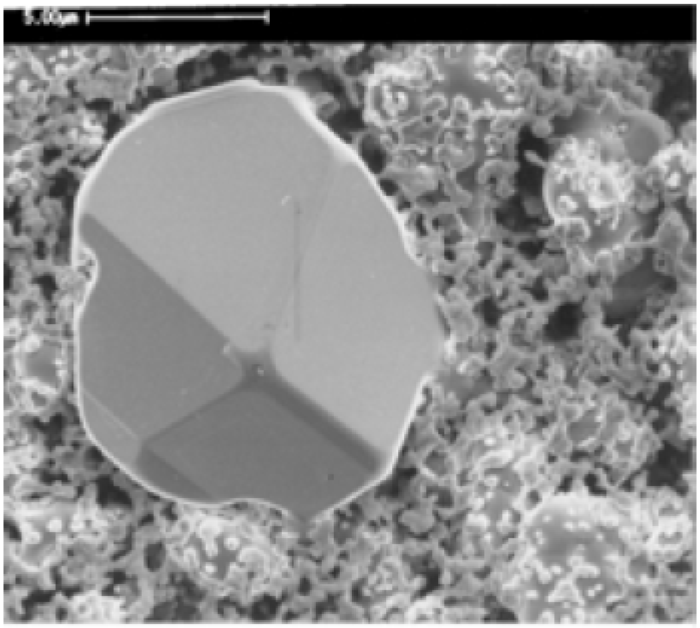

Figure 6 - Growth of Ni particles in Ni/YSZ anode after 2000h at 1000°C [18].

The most important drawback, however, extends from nickel being an excellent catalyst when considering the use of hydrocarbons as fuels. The Ni-YSZ cermet is sensitive to sulfur poisoning and is especially prone to carbon deposition when using hydrocarbon fuels, as it catalyzes the formation of carbon filaments under reducing conditions by promoting the cracking of hydrocarbons [12, 14, 15].

Improvements of the anode includes research into microstructural control of the Ni/YSZ cermet to promote activity and long-term stability, such as the use of composite particles, where Ni grains are covered in fine YSZ grain in order to inhibit Ni grain growth [17]. Alternatively, other materials have been explored to replace one or both components of the cermet with alternative materials which are catalytically active for the oxidation of hydrocarbons but will not promote carbon deposition, which rules out most transition metals [12]. Other oxides, namely ceria, titanate, and chromite-based oxides doped with rare earth metals such as lanthanum and samarium, have also been explored for use as anode materials due to high electrocatalytic activity, but suffer from mechanical degradation in reducing atmospheres and low electrical conductivity [14, 19].

2.1.2.3 Doping of Ni/YSZ cermet

Replacing or doping the YSZ in the Ni/YSZ cermet has also been investigated, using different materials to try to negate the effects of or minimize degradation of performance from carbon deposits. Using scandia stabilized zirconia cermets, for example, helps to inhibit coking better than Ni/YSZ, thus leading to better performance for an extended lifetime [20]. Studies have also shown that adding Cu and Ce to the typical Ni/YSZ cermet, rather than replacing them entirely, can have positive effects on conductivity and oxidation activity and a higher resistance to carbon deposition formation [15]. The addition of small amounts of metals such as gold to typical Ni/YSZ cermet anodes has proven to be an effective way to reduce carbon deposition and boost performance of anodes at lower temperatures, especially when using hydrocarbons, as Au will raise the energy barrier for dissociation of carbon [21].

2.1.2.4 Perovskites

Additionally, MIEC perovskites such as $La_{1-x}Sr_xCrO_3$ have been investigated for use as anodes as they promote high conductivity levels. Though they are not nearly as electrochemically active as Ni/YSZ for fuel oxidation, their conductive properties suggests that composites using these with a slight doping of Ni can promote catalysis while avoiding carbon deposition [12, 14].

Despite the drawbacks it may present, Ni/YSZ cermet remains the standard anode material due to its stability and good electrochemical properties. Many of the other materials studied do not meet the operating criteria for anodes as well as the Ni/YSZ cermet, either due to stability issues or poor oxidation activity by comparison, especially when utilizing H_2 as the fuel [6, 12].

2.1.3 Manufacturing

The manufacturing processes used for the different components of planar fuel cells depend on what portion of the cell acts as the supporting structure. Due to the desire to control size and thickness properties, processes are chosen depending on which component provides the support and can act as a substrate to apply the non-supportive components to. Conventional Ni/YSZ cermet anodes are typically made from commercial NiO/YSZ powders mixed or milled together, with a NiO content of at least ~30vol% necessary to promote the electronic conductivity of the anode, as this has been found to be the threshold for anode conductivity to switch from mainly ionic to electronic [22]. Though some porosity will be formed by the volumetric shrinkage that occurs when NiO is reduced to Ni, which will be explained further in section 2.1.4, pore formers can also be added to this mixture to ensure adequate porosity after sintering.

2.1.3.1 Anode-supported

For anode supported structures, substrates are predominantly produced by tape casting, calendaring, pressing, or a similarly scalable procedure onto which a functional layer of a few microns in thickness is then deposited to enhance activity [23]. This layer can be deposited in any number of ways, most of those also being used for applying anodes onto cells which are electrolyte or cathode supported. This graded structure is recommended for anode supported cells to promote both structural stability and catalytic activity. A thick, high porosity large grain substrate functions as the structural skeleton support bearing a finer-grained electrocatalytically active anode layer to contact with the electrolyte [12], such as that modeled in Figure 7. Anode supported cells are considered state-of-the-art due to high conductivity, an ability to operate at lower temperatures with a minimal impact on conductivity, and lower total resistance from using thin electrolytes [11]. Gas transport through a thick anode can limit performance, but the graded structure described previously helps to alleviate that issue and is also less of an issue with anode supported cells than it is with cathode supported cells, since the anode is supplied with 100% fuel, whereas the cathode is typically supplied with air which is only 21% oxygen. In the case where hydrocarbon fuels are used this can also prove an advantage, as the extensive time the fuel spends traveling through the anode can extend the catalytic interaction between the anode and the fuel [4].

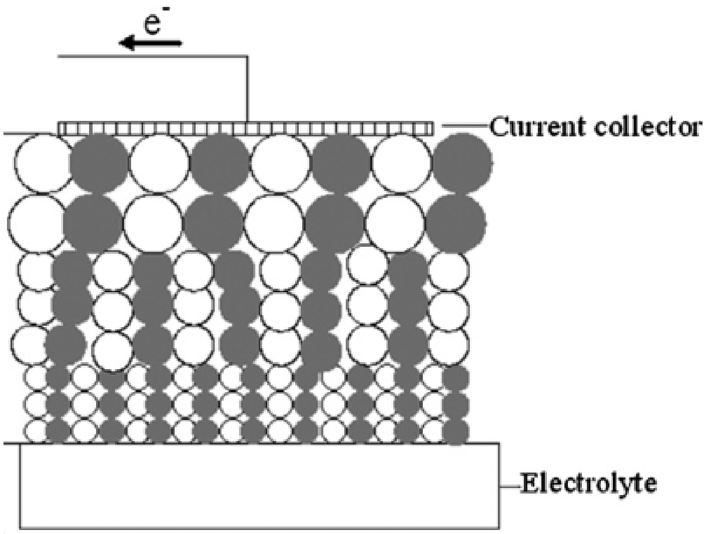

Figure 7 - Graded anode structure model with ionic conductors in black and electronic conductors in white [24].

The coarse grained outer structure not only helps to support the cell, but also allows for a high flow of gas into the electrode, while the finer grained structure provides for a highly active TPB zone at the electrolyte interface. This structure is visualized in the micrograph from [25] in Figure 8. Although the easily visible rounded pores of the outermost layers suggest isolated pores with tight access and poor connectivity between pores, the fabrication routine used to create a graded porous structure is shown to be a viable one. This sample was prepared by first uni-axially pressing disks with pore formers of varying particle sizes of 5 to 50 microns added to the NiO/YSZ mixture, laminating and pressing the 4 layers together, and finally co-sintering the 4 layers into one continuous structure.

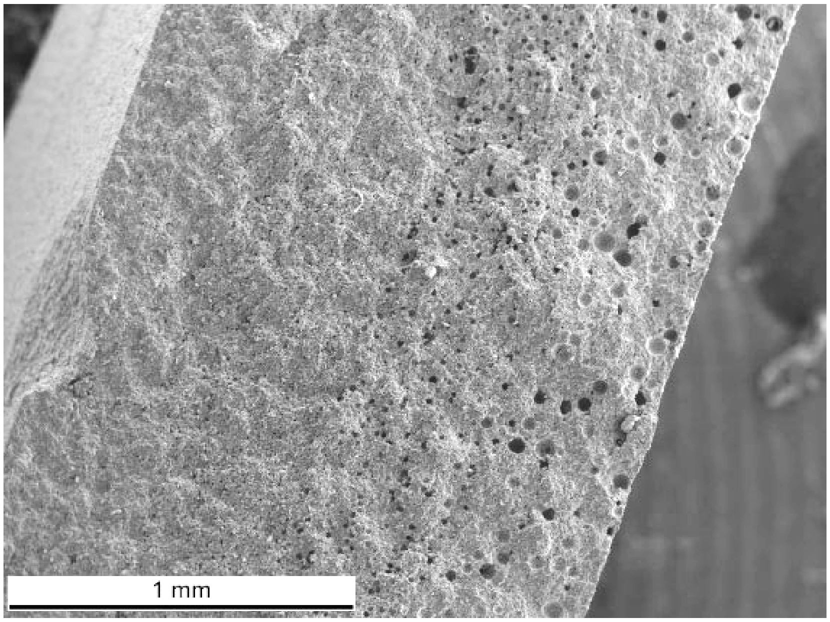

Figure 8 - Four layer anode support with graded porosity [25].

2.1.3.2 Non anode-supported

For cells in which the anode does not act as a support structure, methods such as slurry coating, vapor deposition, dip coating, and screen printing are all viable options, though screen printing is the most popular as it is easily scalable and has reasonable cycling times [26]. Table 3 shows various deposition processes which can be used to produce layers of various thicknesses on substrates [5]. Although this table mainly uses examples for YSZ being deposited on an anode or other substrate, the processes are also viable for depositing the anode and cathode onto the electrolyte.

Table 3 - Selected deposition methods [5].

Method	Example
Spin coating	0.2–2 µm YSZ films on porous or dense substrates
Vacuum evaporation	25 µm YSZ films on Ni foils
Sputtering	1–3 µm YSZ films on dense or porous substrates
Colloidal deposition	10 µm YSZ on porous NiO/ YSZ substrates
Plasma spraying	10 µm cathode, 220 µm electrolyte, 10 µm anode on porous metallic support
Spray pyrolysis	5–10 µm YSZ films on anode substrates
Sol-gel	YSZ films on porous LSM cathode substrates
Electrophoretic Deposition	YSZ less than 10 µm on porous NiO/Ca stabilized ZrO2 substrates
Electrostatic assisted vapor deposition	5–20 µm YSZ on NiO/YSZ substrates
Metal organic chemical vapor deposition (MOCVD)	YSZ thin films on fused silica substrates
Electrochemical vapor deposition (EVD)	Dense 40 µm YSZ layers on porous substrates
Laser deposition	0.5–0.7 µm YSZ films

2.1.3.3 Sintering

Deposition of the anode layer onto the electrolyte is then followed by sintering. It is also possible to co-sinter components, such as those produced by calendaring or pressing anode and electrolyte tapes together, but this can be made challenging by the differing thermal properties of the materials causing varying shrinkage rates [26]. Sintering temperatures for different systems will vary depending on the composition and powder properties of the cermet such as average particle size and size distribution, as well as the manufacturer, as some powders may be more active than others. This dictates that a characterization routine be used to determine the optimal particle size distribution and sintering temperature for anodes of each unique system. Powder treatments such as coarsening by heat treatment can often be used to control the size distribution and shrinkage profile, ensuring reproducibility. It is important to note , however, that processing parameters such as particle size and distribution, heat treatment, and sintering of the powders used for a Ni/YSZ cermet are closely inter-related, so their effect on the performance of the anode needs to be evaluated together, rather than independently [22].

2.1.4 Material Properties of Ni/YSZ

As previously described, manufacturing of Ni/YSZ anodes begins is done by using NiO powder to create the cermet mixture, which is later reduced to Ni under initial operation with the addition of fuel. The high temperature provides the energy necessary for the endothermic reaction which reduces NiO in the presence of a fuel such as hydrogen to Ni in the reaction in Equation 4.

$$NiO + H_2 \rightarrow Ni + H_2O \qquad \textbf{(4)}$$

Nickel oxide exists in a densely packed rock salt structure where the Ni and O atoms alternate. This creates significant voids within the lattice due to the difference in atomic radius between the two. The rock salt structure of NiO can be seen in Figure 1, in both unit cell and expanded forms, and its attributes are displayed in Table 4. The unit cell can be described as having the anions in an FCC structure with cations occupying all of the interstitial sites in between the anions.

Table 4 - NiO crystal structure properties [27, 28].

Material	Nickel Oxide, NiO
Chemical formula weight	74.69
System @ 23.5°C	Cubic
***a* (Å), *b* (Å), *c* (Å)**	4.178
Unit cell volume (Å^3)	72.9
Calculated density (g/cm^3)	6.80

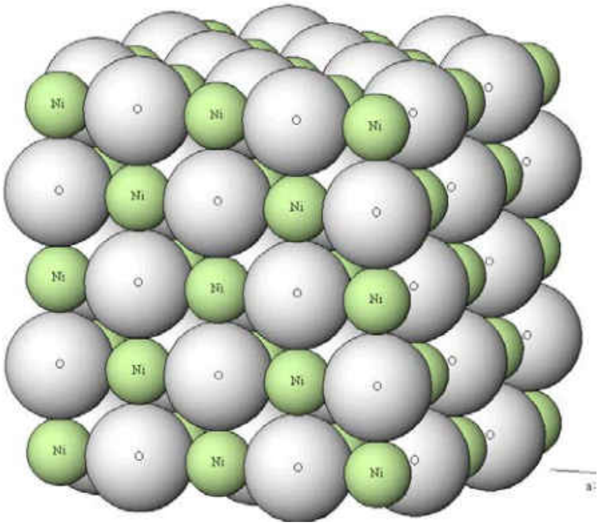

Figure 9 - Nickel oxide rock salt structure [27].

Once reduced, nickel will then form into an FCC structure and act as an electronic conductor to remove the free electrons produced in the electrochemical reaction from the anode-electrolyte interface and conduct them to the external circuit. The nickel FCC unit cell can be seen in Figure 10 and its properties in Table 5. Comparing Table 4 and Table 5 shows that the reduction of NiO to Ni is accompanied by a densification of the material and a significant decrease in unit cell volume characterized as shrinkage of the particles.

Table 5 - Ni crystal structure properties [27].

Material	Nickel, Ni
Chemical formula weight	58.69
System @ 25°C	Cubic
***a* (Å), *b* (Å), *c* (Å)**	3.5238
Unit cell volume (Å^3)	43.76
Calculated density (g/cm^3)	8.91

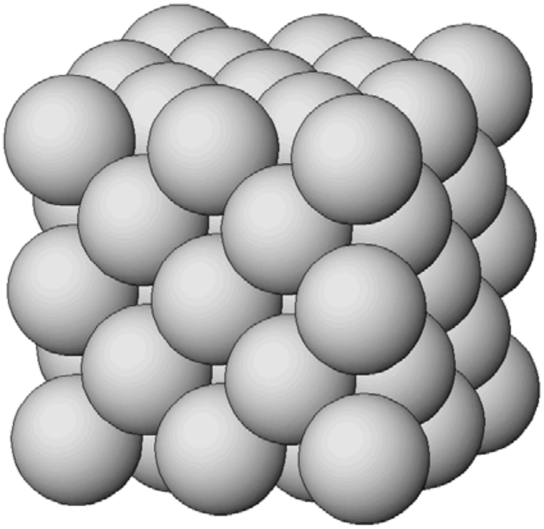

Figure 10 - Nickel FCC structure [27].

The presence of YSZ in the Ni/YSZ cermet matrix prevents the rapid shrinkage of the anode and evens out the coefficients of thermal expansion between the anode and electrolyte. This is especially important as there is a volume reduction of 25% when NiO is reduced to Ni, as shown in the micrographs of Figure 11 [14].

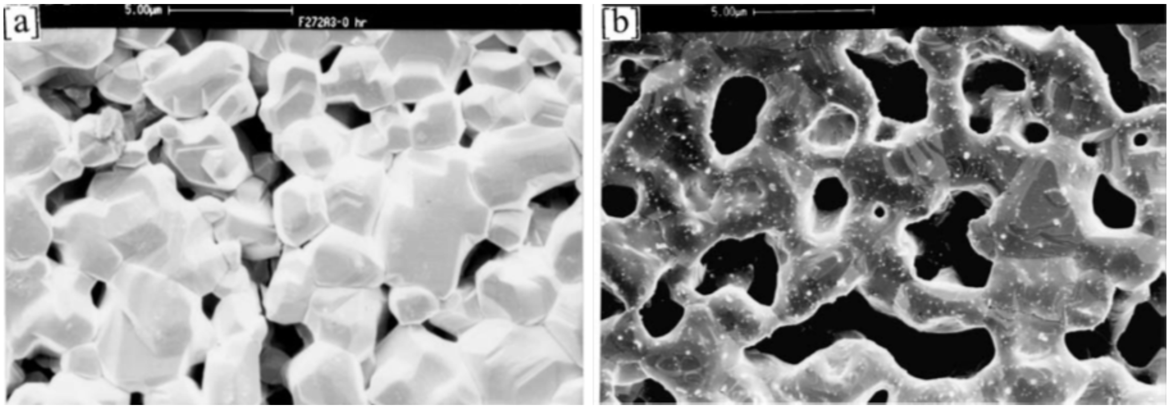

Figure 11 - Volumetric change of Ni (a) before and (b) after reducing in humidified 10%H_2/90%N_2 for 1h at 1000C [14].

The Ni and YSZ do not diffuse into each other to form a new interphase, however, as the two are basically insoluble in each other and non-reactive in a large temperature range [19]. This is what allows for Ni/YSZ cermet to be easily produced using processes that are easily scalable. The matrices of both exist within the anode as parallel networks of conductors, and together with the pore structure which allows for the fuel to diffuse into the anode towards the electrolyte interface, they form the electrochemically active triple-phase boundary.

2.2 Electrolyte

2.2.1 Function

The electrolyte of a solid oxide fuel cell acts as an ionic conductor for the oxygen ions to travel from the cathode interface of the cell to the anode interface so that the electrochemical reaction which creates electricity may be completed. Therefore, high ionic conductivity is a critical requirement in the selection of materials for fabrication of the electrolyte. Oxygen ion motion occurs through interstitial or vacancy hopping in the lattice, so material defects play a key role in conductivity[29]. The material chosen must also have mechanical strength, to lend the thin structures some measure of robustness in order to survive operating conditions. This is especially true when dealing with electrolyte-supported cells. Additionally, SOFC electrolytes must also have negligibly small electronic conductivity in order to prevent forming a partial internal electric short circuit within the cell which will reduce total electric output and overall cell performance [30], and stability in both reducing and oxidizing atmospheres, as the electrolyte is exposed to both the reducing and oxidizing environments during SOFC operation. There are several oxides which are commonly used as electrolytes for SOFCs. These include several stabilized-zirconia based and ceria based fluorite structures, $LaGaO_3$ based perovskites, and bismuth oxides. The ionic conductivities of some typical electrolyte compositions are presented in Figure 12 as a function of temperature.

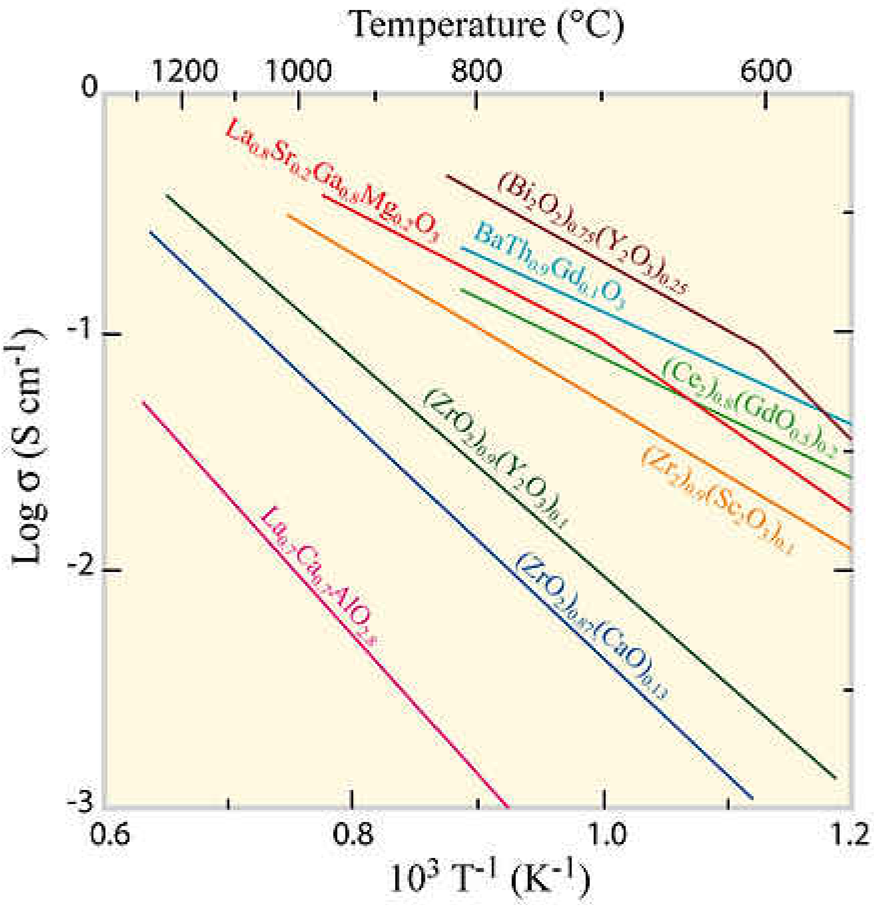

Figure 12 - Temperature vs. Ionic Conductivity of some popular SOFC electrolytes [11].

2.2.2 Materials

2.2.2.1 Stabilized Zirconia

Stabilized zirconia is typically accepted as a standard material for the fabrication of SOFC electrolytes. Stabilized zirconia is produced by doping ZrO_2 with divalent and trivalent metal oxides such as Y_2O_3, Yb_2O_3, Sc_2O_3, CaO, and others to stabilize the high temperature conductive phase and create oxygen vacancies of ions to move through, enhancing conductivity

[29]. Without the dopants, zirconia undergoes phase changes at several temperatures which are accompanied with volumetric changes, rendering it unstable under SOFC operating conditions. There is, however, an upper doping limit with all stabilized oxides at which the increased defect concentration impedes mobility and actually impedes conductivity [31]. The upper limits and the effects of over-doping on conductivity of stabilized zirconia with several dopants are shown in Figure 13. The most dramatic example of this concept is seen when using CaO as a dopant, as the conductivity increases rapidly until the sharp peak around 12 mol% and then decreases nearly as quickly.

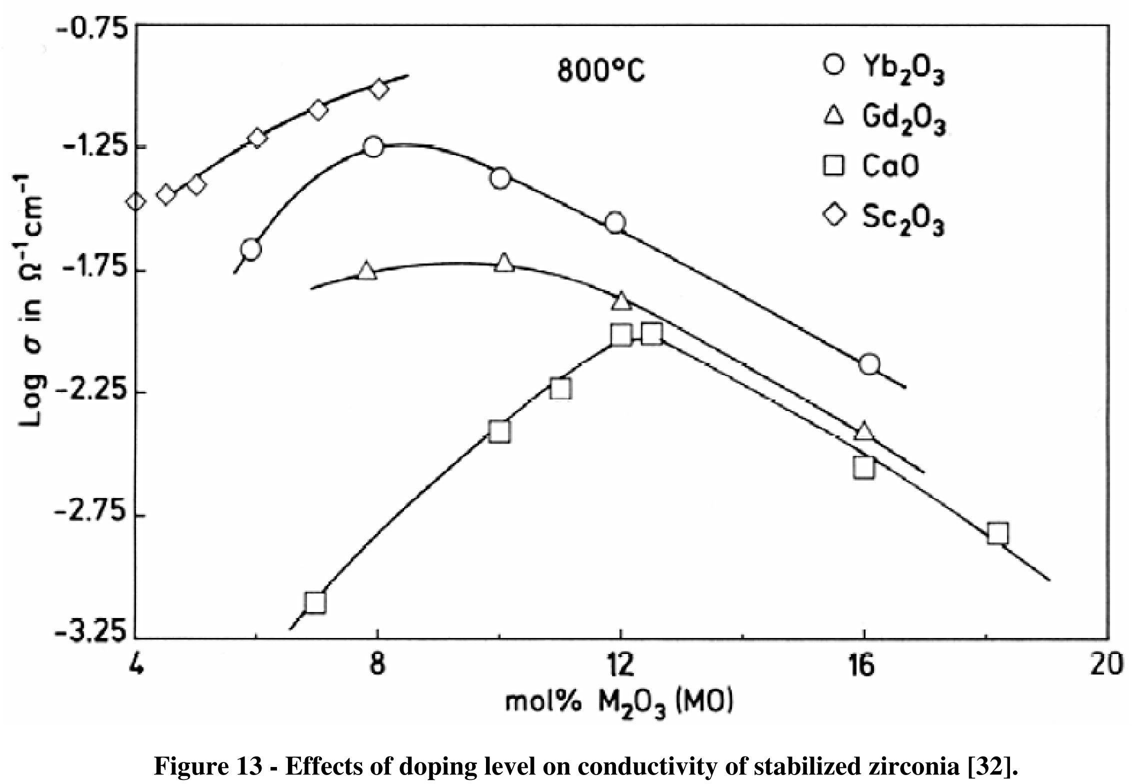

Figure 13 - Effects of doping level on conductivity of stabilized zirconia [32].

Stabilized zirconia is an electronic insulator at room temperature, an ionic conductor from 600–1000 °C and a mixed conductor (both electronic and ionic) at around 1500 °C [1]. This means zirconia based electrolytes have good ionic conductivity at SOFC operating temperatures (800-1000°C) and sufficient mechanical properties to withstand the rigors of operation. The most popularly used dopant and current standard is Y_2O_3. This is due to reasons of cost, availability, structural stability in a wide temperature range, chemical stability under both reducing and oxidizing conditions, and compatibility with other materials used in fuel cell components [1, 8]. There are two well-explored doping levels at which Y_2O_3 stabilizes ZrO_2 while at operating conditions; 3 mol% stabilizes the tetragonal phase and 8 mol% stabilizes the cubic phase [33]. The 8 mol% YSZ (8YSZ) is the preferred choice for most current SOFC manufacturing, as it offers the highest ionic conductivity for YSZ, around 0.15 S/cm at 1000°C as opposed to 0.055 S/cm at 1000°C for 3YSZ [34]. However, 3 mol% YSZ (3YSZ) offers higher toughness and thermal shock resistance than 8YSZ, making for an over-all stronger and more reliable electrolyte, especially when acting as the support structure [31].

Other dopants for stabilized zirconia have also met with some mixed success. Zirconia doped with Sc_2O_3 (SSZ) has shown to have very good conductivity, the highest in comparison to other doped zirconias, as show in Figure 13 above, and is considered a viable successor to YSZ. The highest conducting mixture, 10 mol% SSZ, has shown conductivity of up to 0.12 S/cm at 800°C, and doping with just 7 mol% Sc yields conductivities up to 0.20 S/cm at 1000°C, higher than the conductivity of 0.18 S/cm reported for 8YSZ [2, 31, 35]. However, SSZ exhibits poor phase stability, and a cubic-to-rhombohedral phase transition occurs at 300-500°C, causing a loss in stability which impacts the conductivity and structural integrity [36]. It is possible to stabilize the more conductive cubic phase of SCSZ by co-doping with CeO_2. In particular, 10mol%Sc_2O_3-1mol%CeO_2-ZrO_2 (SCSZ) electrolytes sintered at high temperatures yield a stable cubic structure and conductivity of 0.084S/cm at 800°C [37], which although lower than that of SSZ, is higher than YSZ. SCSZ has both rhombohedral and cubic phases present at room temperature. However, an increase in temperature shows a decrease of the presence of the rhombohedral phase, and only the cubic phase is present above 500°C [38]. Sintering at high temperatures (above 1300°C) results in entirely cubic SCSZ samples at room temperature. SCSZ electrolytes, however, are prone to destabilizing during normal SOFC operation due to a reversible cubic-to-rhombohedral phase transition at 300-400°C which makes working with SCSZ electrolytes comparatively harder than YSZ [39].

2.2.2.2 Ceria Oxides

Ceria-based oxides have shown some promise for lower temperature SOFCs as well, as the conductivity of doped ceria is around an order of magnitude larger than similarly doped stabilized zirconia [8]. This is largely due to the larger size of Ce ions in comparison to Zr ions. Although both oxides have a fluorite structure, the larger radius of the Ce ions produces a more open structure through which oxygen ions can diffuse [40]. Like zirconia, ceria is doped to promote both stability and conductivity. The most commonly used dopants for CeO_2 are Gd_2O_3, Sm_2O_3, and Y_2O_3 but ceria doped with 20 mol% Gd_2O_3 (GDC) has shown particularly promising high conductivity [41]. However, under reducing conditions some of the Ce^{4+} ions become partially reduced to Ce^{3+} ions and the ceria electrolyte becomes electrically conductive, which causes an internal shunt to develop within the cell and a lower transport number [42].

2.2.2.3 Perovskites

Perovskites based on $LaGaO_3$ have gained some attention within the last decade and show promisingly high conductivities. In particular, $La_{0.9}Sr_{0.1}Ga_{0.8}Mg_{0.2}O_{3-x}$ (LSGM), in which both the Sr and Mg doping generate oxygen vacancies is of high interest, with conductivities of 0.12 S/cm at 800°C and 0.32 S/cm at 1000°C reported [43]. Like doped ceria, LSGM is also a rather complex system, as seen in Figure 14, and undergoes phase transformations in the range of temperatures which it would experience under operating conditions and can react with some other materials commonly used in SOFCs to form new interphases, making it rather unstable [44, 45]. For example, it has been shown that LSGM can react with NiO and CeO_2 based materials to form the non-conductive phases of $LaSrGa(Ni)O_{4-\delta}$ and $LaSrGa_3O_7$, respectively [46, 47]. LSGM also suffers from low mechanical strength and flexural strength at SOFC operating temperatures as compared to stabilized zirconia electrolytes, so they would be a poor choice for electrolyte-supported designs [43].

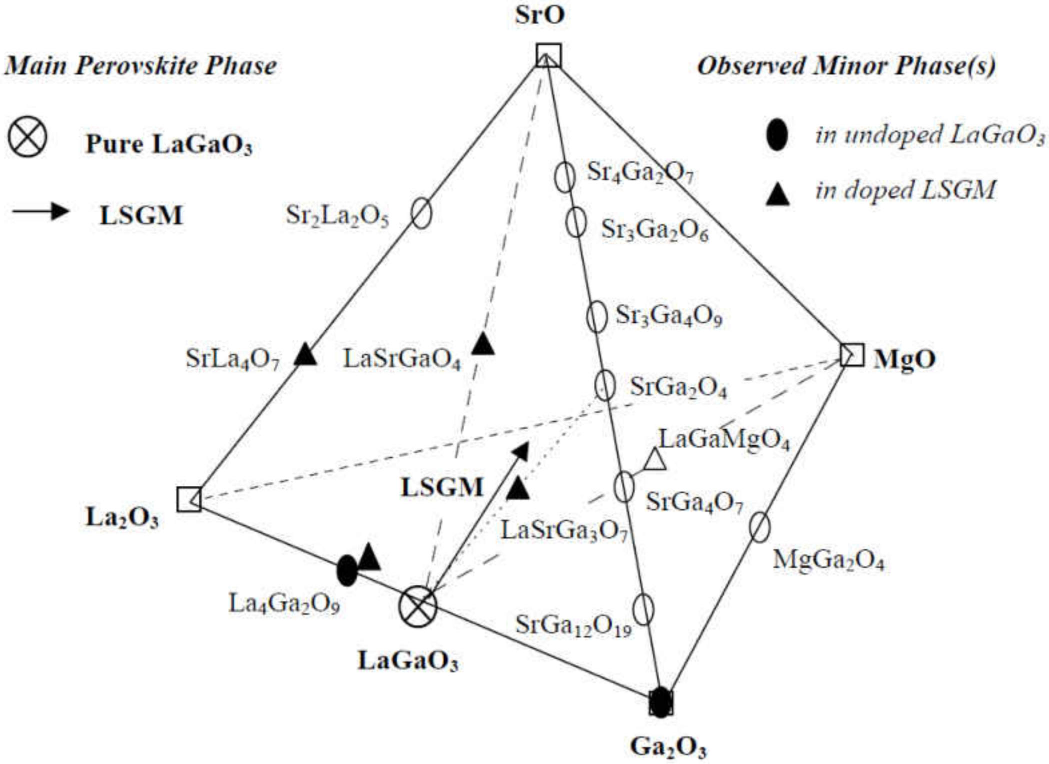

Figure 14 - The LSGM quaternary phase diagram at 1500 °C [44].

2.2.2.4 Bismuth Oxide

Doped bismuth oxides have received increased attention due to very high conductivity values. Examples of doped Bi_2O_3 can be seen in Table 6, which shows several dopants and their conductivities, shows that doped bismuth oxides have characteristically high conductivities at reduced operating temperatures. The main drawbacks of bismuth oxide are rather numerous, which prevents this material from being a contender with other materials. These limiting traits include easy reduction to bismuth metal in fuel containing atmospheres, high electronic conductivity, high reactivity, low stability, and very low strength and toughness [31, 48].

Table 6 - Conductivity values of some reduced temperature bismuth oxide electrolytes [48].

Composition	Temperature (°C)	Structure	Conductivity (S·cm^{-1})
Bi_2O_3	800	FCC	2.3
$Bi_{0.75}Y_{0.25}O_{1.5}$	600	FCC	$4.38x10^{-2}$
$Bi_{0.65}Y_{0.20}O_{1.5}$	600	FCC	$2.5x10^{-2}$
$Bi_{0.65}Gd_{0.35}O_{1.5}$	650	FCC	$5.6x10^{-2}$
$Bi_{0.8}Tb_{0.2}O_{1.5}$	650	FCC	0.28
$Bi_{0.715}Dy_{0.285}O_{1.5}$	700	FCC	0.14
$Bi_{0.75}Ho_{0.25}O_{1.5}$	650	FCC	0.17
$Bi_{0.80}Er_{0.20}O_{1.5}$	600	FCC	0.23
$Bi_{0.80}Er_{0.20}O_{1.5}$	700	FCC	0.37
$Bi_{0.75}Tm_{0.25}O_{1.5}$	650	FCC	$8.0x10^{-2}$
$Bi_{0.65}Yb_{0.35}O_{1.5}$	700	FCC	$6.3x10^{-2}$
$Bi_{0.7}Gd_{0.3}O_{1.5}$	700	FCC	$1.0x10^{-2}$
$Bi_{0.75}Lu_{0.25}O_{1.5}$	650	FCC	$3.7x10^{-2}$

2.2.2.5 Layered YSZ/SCSZ Composite

Although some of these electrolytes may have higher conductivities, stabilized zirconia, YSZ in particular, offers the most dependable combination of stability and conductivity, and as such it remains the electrolyte of choice for most manufacturers. This also coincides with the use of Ni/YSZ cermet in the anode, as the combined use of the two helps create a strong connection between electrolyte and electrode which raises performance.

Recently, a layered combination of YSZ and SCSZ has been studied [39]. The layered structure provides several advantages while compromising on the specific advantages of each material. The layered design can be seen in Figure 15, with the different material sections clearly labeled.

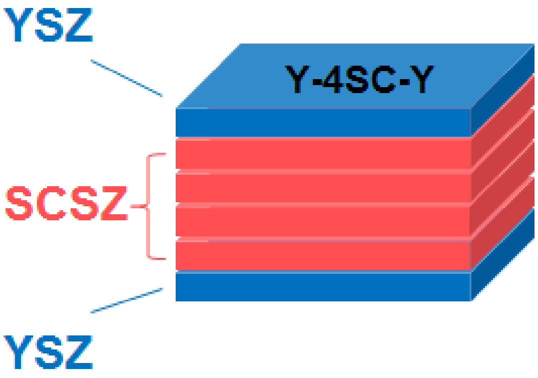

Figure 15 - The YSZ/SCSZ layered electrolyte can be seen here in their relative thickness ratios [39].

The layered YSZ/SCSZ/YSZ structure is constructed this way in order to achieve a balance of the advantages that each of the materials has to offer. Although the SCSZ has superior ionic conductivity as compared to that of YSZ, the mechanical strength of YSZ and phase stability is superior to that of SCSZ at high temperatures. The YSZ outer layers are used for stability and protection of the inner SCSZ layers and the SCSZ layers help raise the overall conductivity of the electrolyte structure. The outer layers of YSZ help to stabilize the SCSZ in its more stable and conductive cubic phase which is reached during the co-sintering of the YSZ/SCSZ layered structure at high temperatures. There is also a slight mismatch in thermal and mechanical properties which leads to residual stresses within the finished electrolyte. These stresses help to impart increased strength and toughness to the electrolyte structure, and actually enhance conductivity. At operating temperatures these compressive stresses also proved the layered composite electrolytes to be stronger than both pure SCSZ and YSZ electrolytes [39].

As previously mentioned, there are two choices when choosing the material for the outer layers of the electrolyte. Both 8YSZ and 3YSZ can be used to stabilize the inner layers of SCSZ, however 8YSZ will offer higher conductivity while utilizing 3YSZ will result in a tougher and stronger electrolyte. The difference in strengths of the layered structure is correlated with the properties of the individual materials, which are described in 2.2.4.

2.2.3 Manufacturing

When the electrolyte is acting as the supporting component in the cell, there are a number of manufacturing techniques available for use to produce a strong, supportive, homogeneous electrolyte base structure. These techniques include tape casting, slip casting, pressing, extrusion, calendaring, and dispensing, among others [5, 26, 49].

The general trend is to focus more on up-scalable methods which can be more easily commercialized and lead to high yield. This would allow for an easier transition to mass production and ultimately lower cost. Typically, the production processes which fit these criteria for production of planar SOFCs are tape casting, calendaring, and screen printing [50].

2.2.3.1 Tape Casting

The tape casting method uses slurry mixed by ball milling the base powder with binders and dispersants [49]. The slurry is then de-aired and tape casted using a doctor blade with a set height. The height of the doctor blade and the collection roller speed are determined by the properties of the slurry and the desired properties of the resulting tape. An up-scaled, high yield production method could resemble the one in Figure 16.

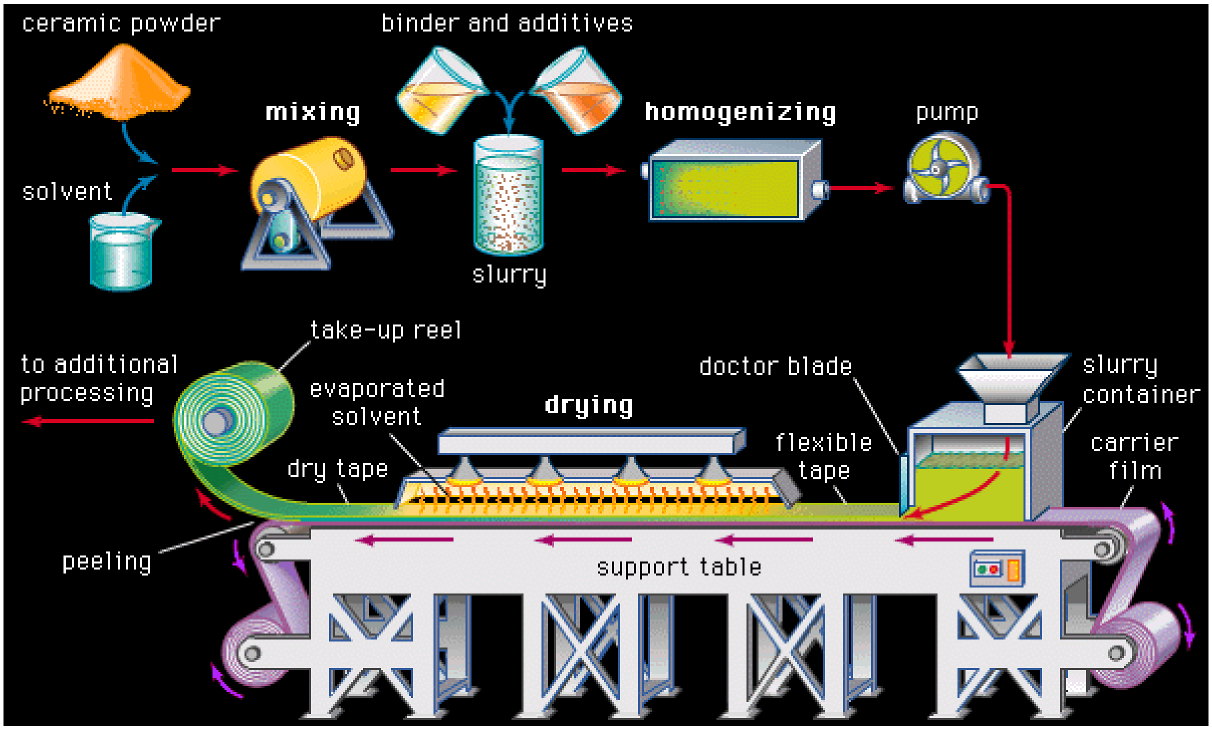

Figure 16 - Large-scale tape casting operation [51].

2.2.3.2 Calendaring

Thicker, multi-layer electrolytes and thin electrolytes which are not the support structure can be made by calendaring. In the calendaring process tapes are formed by forcing a homogenous mass formed in a high shear mixer through a set of rollers. The different rollers are then passed through another set of rollers to press the layers together, forming a multi-layer tape as in Figure 17. The tapes can then be punched and sintered. This can also be used to co-form multiple components into a single green tape, pressing the anode and electrolyte together and co-firing them to enhance the bonding strength between the two components [5]. The extrusion method is similar, where a plasticized mass is forced through a die to form the desired green shape.

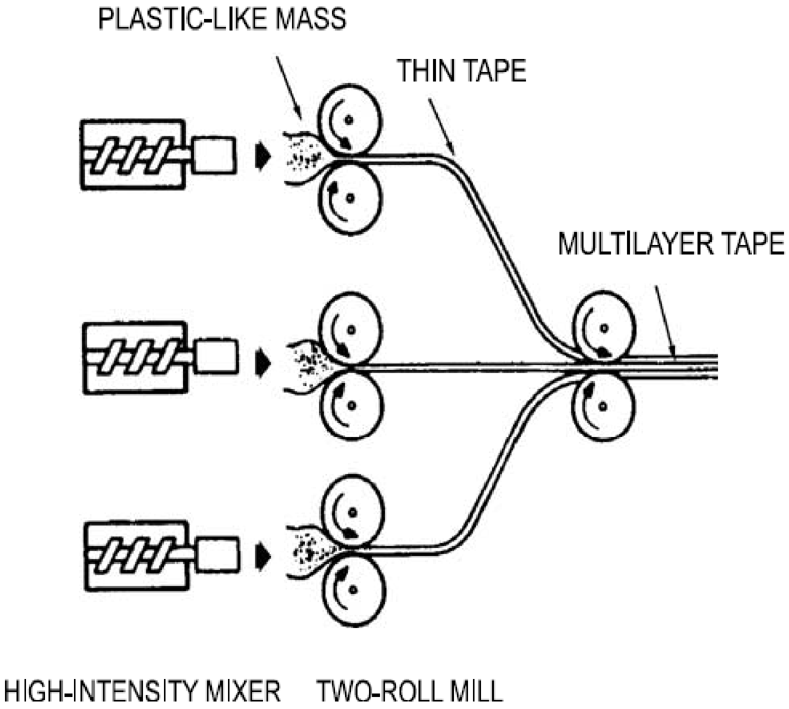

Figure 17 - Tape calendaring process [5].

2.2.3.3 Spin Coating

In non-electrolyte-supported cells, such as the popular anode-supported cells previously described, electrolytes are applied using thin film deposition techniques. Using thin films electrolytes reduces ohmic resistance in comparison to thick film electrolytes, even at reduced temperatures [52]. Although most of the techniques listed in Table 3 are viable methods, scalable methods which are more easily reproducible are likely to be used more often, such as spin coating and spray deposition. The spin coating method involves forming a suspension of the electrolyte powder in a solvent such as ethanol which is then dripped onto the surface of the substrate to flood it. The substrate is then spun at high speeds to leave a thin layer of deposited particles as the liquid flows radially outwards, owing to the centrifugal forces caused by the spinning [52, 53]. The final thickness and uniformity of the deposited film will depend on various variables of both the suspension (particle size, viscosity, solvent evaporation rate) and the spin recipe used (speed, acceleration) and is considered a multi-stage process involving both wet and dry states of the film in which it behaves differently [53, 54].

2.2.3.4 Spray Deposition

There are also various spray deposition techniques which can be used to apply thin, dense films onto substrates, such as for applying a thin electrolyte onto an anode support. For chemical spray deposition, a dilute solution of precursors which to make up the desired composition and solvents are sprayed onto the heated surface of the substrate, evaporating the solvents as the droplets reach the heated surface to create the thin film [55]. Electrostatic spray deposition (ESV) is similar; a solution is formed from precursors and solvents and then atomized by an electric field into an aerosol form which is then used to coat a heated substrate [56]. Both of these spray methods are good for thin film deposition due to the ease of setup, reproducibility, and controllability; ESV film properties and surface morphologies can be controlled and altered simply by adjusting substrate temperature and duration of deposition [57].

2.2.4 Structural and Mechanical Properties of YSZ and SCSZ

The mechanical properties of zirconia doped with 1% to 10% Y_2O_3 are typically generalized, as they do not vary very much at room temperature. For the given range of doping percentages, the Young’s modulus is often generalized around 205 GPa, with a Poisson’s ratio of

0.31 [58]. Experimental results obtained previously show the Young's modulus of SCSZ to be around 207 GPa, not showing much variation from Y_2O_3 doped ZrO_2 [59]. The fracture toughness of these materials has also been reported, with a varying range of values. It is worthy to note that the properties of these materials can vary depending on the properties of the powders, such as the grain size of the powders or being ceramics they can vary depending on the evaluation method used. Due to this discrepancy, some of the values presented here are averages of multiple sources. The value of fracture toughness for 3YSZ has been generally cited as around 10 $\mathrm{MPa}\sqrt{\mathrm{m}}$ and the variations in strength can depend on particle sizes and processing techniques [60]. The fracture toughness of 8YSZ varies less, from 1.3 to 1.7 $\mathrm{MPa}\sqrt{\mathrm{m}}$ [60, 61]. Fracture toughness values are given at room temperature.

The mechanical properties of these materials also depend on temperature, with the Young's modulus changing depending on the % of YSZ doping in the ZrO_2. Generally, the higher the amount of doping, the higher the drop in Young's modulus is at operating temperature. For 3YSZ the Young's modulus drops from 205 at room temperature (RT) to 170GPa at the operating temperature of 800°C (OT), from 202.4 to 140GPa for 8YSZ, and from ~201 at RT to ~155GPa at OT for SCSZ and has a sharp drop to below 100GPa around 400°C [58, 62]. These differences in strength will impact the final quality of single cells produced from layered electrolytes.

Table 7 - Summary of mechanical properties of electrolyte materials used in layered YSZ/SCSZ electrolyte.

	3YSZ	8YSZ	SCSZ
Young's modulus @ RT (GPa)	205	202.4	~210
Young's modulus @ OT (GPa)	170	140	~155
Poisson's ratio	0.31	0.31	0.31
Fracture toughness (MPa√m)	10	1.5	N/A

Zirconia oxide exists in a fluoride structure, represented in Figure 18, with properties listed in Table 8.

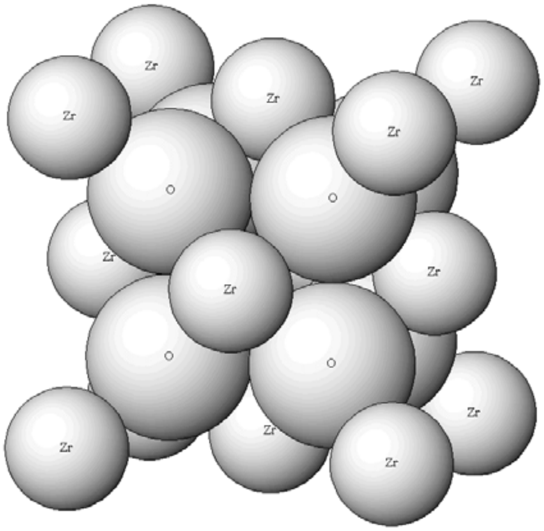

Figure 18 - ZrO_2 fluorite structure [27].

Table 8 - ZrO_2 crystal structure properties [63].

Material name	Zirconium Oxide, ZrO_2
Chemical formula weight	123.22
System	Monoclinic @ 25°C
***a* (Å), *b* (Å), *c* (Å)**	5.1501, 5.2077, 5.3171
α (deg), β (deg), γ (deg)	90, 90.224. 90
Unit cell volume (Å^3)	140.76
Calculated density (g/cm^3)	5.81

Zirconia has high thermal and electronic resistances, and is robust even at elevated temperatures, which makes it a good candidate for an SOFC component. However, pure zirconia undergoes several phase transformations at elevated temperatures and can cause rapid expansion of the material which can lead to cracking. This effectively eliminates pure zirconia for use in structurally-dependent applications, such as being the supporting electrolyte of an SOFC. For this purpose, yttrium oxide (Y_2O_3), which has a cubic bixbyite structure, is used to dope ZrO_2 which helps to stabilize the ZrO_2 structure in a wider temperature range. The cubic bixbyite structure is a modified fluorite structure where one anion location in four is vacant in order to compensate for the trivalent cation charge [64].

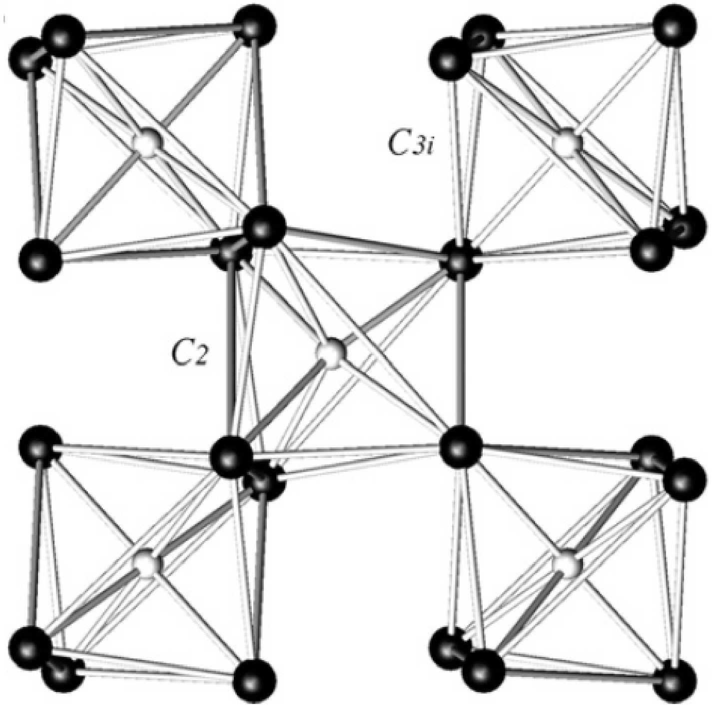

Figure 19 - Y_2O_3 cubic bixbyite structure with different distorted octahedral arrangements caused by the oxygen vacancies [65].

The substitution of Y_2O_3 into ZrO_2 stabilizes the structure in and eliminates the phase transformations. As was previously mentioned, doping zirconia with Y_2O_3 also results in the creation of oxygen vacancies which enhance the conductive properties of zirconia oxide. Table 3 presents the dimensions of the tetragonal crystal structure of the commonly used 3mol% YSZ.

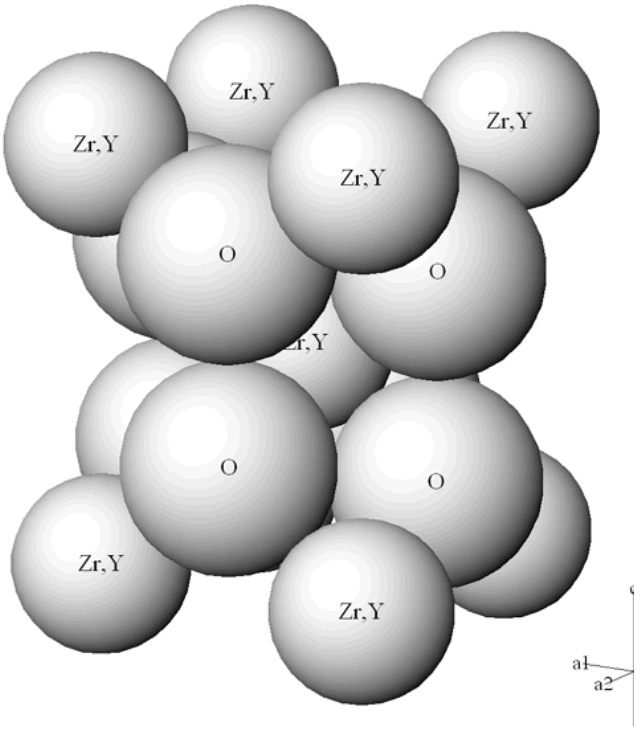

Figure 20 - 3mol% YSZ unit cell [27].

Table 9 - 3mol% YSZ crystal structure properties [66].

Material name	3mol% Yttria stabilized zirconia, YSZ
Composition	$(ZrO_2)_{0.97}(Y_2O_3)_{0.03}$
Chemical formula weight	122.62
System	Tetragonal @ 25C
***a* (Å), *b* (Å), *c* (Å)**	3.6067, 3.6067, 5.1758
***α* (deg), *β* (deg), *γ* (deg)**	90
Unit cell volume ($Å^3$)	67.33
Calculated density (g/cm^3)	6.05

SCSZ in its stabilized cubic form has a theoretical density of 5.74 g/cm^3, but this can vary depending on the manufacturer's actual powder composition, and a lattice parameter of 5.09Å [67, 68]. Sintering at high temperatures (above 1300°C) results in SCSZ samples being stabilized in the cubic phase at high temperature.

2.3 Cathode

2.3.1 Function

The cathode side of the SOFC is where the electrochemical oxygen reduction reaction occurs. The cathode needs to be highly catalytically active towards oxygen reduction and have high electronic conductivity, good ionic conductivity, high porosity for the diffusion of oxygen gas through the cathode to the electrolyte, and have good chemical and thermal stability and compatibility within the oxidizing environment and with the electrolyte. At the cathode-electrolyte interface, the reduction reaction takes place to produce oxygen ions. During the reduction, oxygen is reduced at the triple phase boundaries at the interface between the gas phase, the mixed conductor, and the electrolyte, producing oxygen ions and consuming electrons that are delivered by the external circuit [69]. This is a multi-step process which can involve a number of different pathways for charge transfer. First, gaseous oxygen molecules are partially adsorbed onto the surface of the catalyst, forming hybrid electron orbital with the catalyst and lowering the O-O bond to a lower energy state, as shown in Figure 21 [4]. The adsorbed oxygen travels on the surface of the cathode to the TPB, where it will combine with e^- to form O^{2-}, this can occur instantaneously, splitting the O-O bond completely, or in multiple steps, where O_2

combines with 2e$^-$ to form O_2^{2-} and subsequently combines again with 2e$^-$ to form O^{2-}. The reduction process is very complicated and, in fact, is poorly understood. In an MIEC cathode, this can all occur instantaneously both on the surface of the cathode and in the bulk of the material, due to the mixed conductivity of the cathode, rather than only at the surfaces which form a TPB with the electrolyte. The resulting oxygen ions are either transferred to the electrolyte by traveling through the cathode to the electrolyte interface in the case of an MIEC cathode, or instantaneously transferred to the electrolyte as the reduction reaction is completed at the TPB of gaseous O_2, electronically conductive cathode, and ionically conductive electrolyte [69-72]. The current state-of-the-art material for use in SOFCs is electronically-conducting Sr-doped $LaMnO_3$ (LSM), often as a composite with an electrolyte material such as YSZ to increase ionic conductivity, lengthen the TPB away from the cathode-electrolyte interface, and improve connectivity with the electrolyte [7].

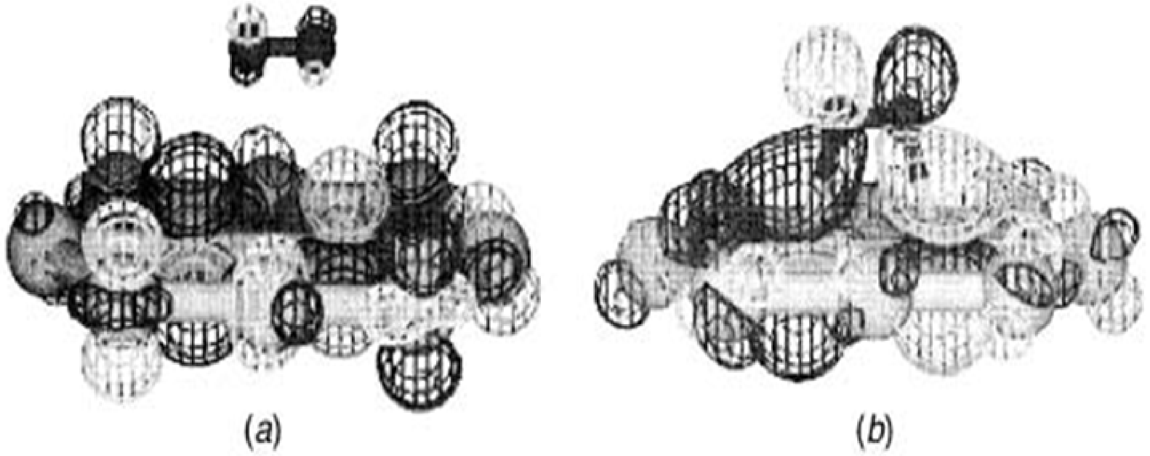

Figure 21 - Oxygen molecule as it (a) approaches the cathode catalyst surface and (b) forms hybrid orbitals with the catalyst, lowering the energy state of the O-O bond [4].

2.3.2 Materials

In order to facilitate the reduction reaction, it is best that the cathode be of mixed conductivity. However, cathode materials need to be primarily electronically conductive, so materials for cathodes can include electronic conductors such as LSM, mixed ionic-electronic conductors (MIECs), such as $La_{1-x}Sr_xFe_{1-y}Co_yO_{3-\delta}$ (LSCF), or composites of electronic and ionic conductors, such as the aforementioned LSM-YSZ composite. There are different reaction paths for each of the aforementioned cases; electrode surface path, electrode bulk path, and electrolyte surface path, respectively, though combinations of these are possible [7]. The added ionic conductivity of MIECs and composites extends the triple-phase boundary from the confines of the cathode-electrolyte interface, extending the reaction zone and increasing performance.

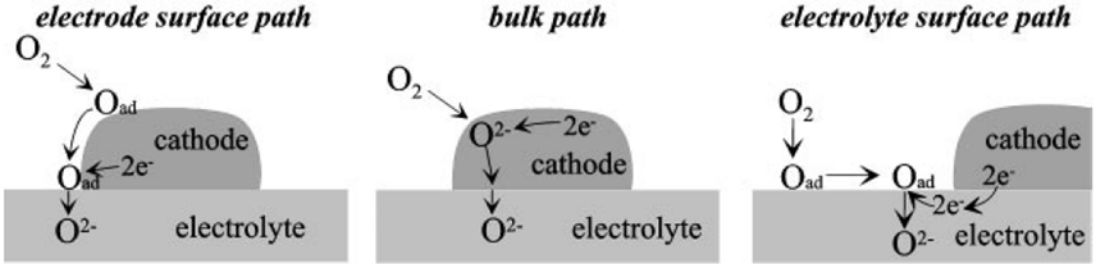

Figure 22 - Reaction paths for electronic conductor, MIEC, and composite cathodes, respectively [70].

Perovskite-type materials are extensively studied and used as cathodes for SOFCs due to the benefits of their mixed conductivity [73]. The perovskite structure ABO_3 is seen in Figure 23, with an A-site cation, such as Lanthanum, occupying a simple cubic structure and the B-site cation, such as Iron or Manganese, occupying the center of the cubic structure. Oxygen atoms are arranged in the octahedral interstitial sites. Substitutions of the base structure such as the popular lanthanum manganite, $LaMnO_3$, with dopants such as strontium enhance the conductive properties and stability of the perovskite. Perovskite materials used for SOFC cathodes include manganites, cobaltites, ferrites, and nickelates, among others [7, 43, 74-77].

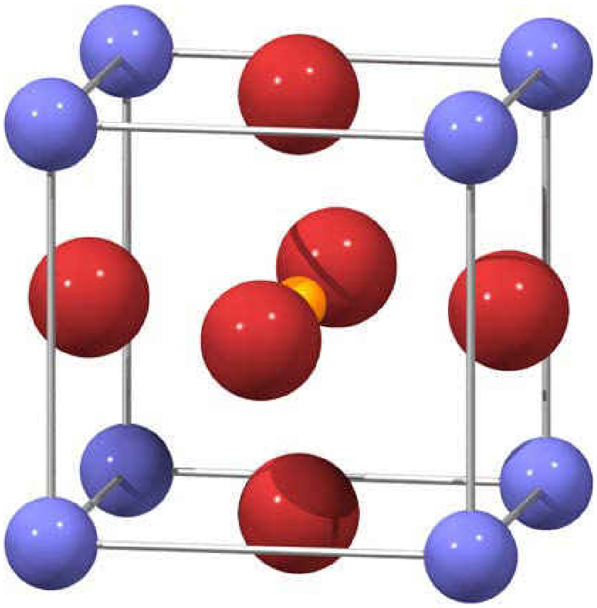

Figure 23 – Perovskite structure with purple A-site cations, orange B-site cations, and red oxygen anions [78].

Many perovskite structures do not have the perfect cubic structure shown in Figure 23, but are distorted, and distortions can be further enhanced by substitutions of A- and B-site cations. For ionic radii of r_A, r_B, $r_{O,}$ there exists a tolerance factor, t, given in Equation 4, which must lie within the range $0.8<t<1.0$; or $r_A>0.090$ nm, $r_B>0.051$ nm [79] to ensure stability of the ideal cubic structure. The stability of materials with a perovskite crystal structure increases with the size of the A-site cation, which makes lanthanum based perovskites a very attractive choice for several applications [74].

$$(t) = \frac{(r_A + r_O)}{\sqrt{2}(r_B + r_O)} \tag{5}$$

Electronic conductivity is enhanced by substitution of the La^{3+} site with lower valence ion such as strontium, Sr^{2+}. Strontium is a preferred dopant for the A-site cation of SOFC applications because the resulting perovskite forms stable compounds with high conductivity in the oxidizing atmosphere found at the cathode due to the closeness of ionic radii of the two ions [74] .

2.3.2.1 Manganites

The aforementioned LSM, and other manganites, are considered state-of-the-art due to their high electronic conductivity, strong activity for oxygen reduction at high temperatures, and thermal compatibility with common solid electrolytes such as YSZ [76]. However, LSM cathodes suffer from low oxygen ion conductivity and reactivity with YSZ in high temperatures to form low-conductivity zirconates such as $SrZrO_3$ and $La_2Zr_2O_7$ when Sr doping exceeds 30 mol% [80]. Reactivity can be controlled by introducing deficiencies in the A-site of LSM and enhance performance due to a higher concentration of oxygen vacancies [81]. Other promising manganites exist by replacing La with other rare earth elements. Sr- and Ca- doped $PrMnO_3$, for example, exhibit even higher electrochemical activity and electronic conductivity and lower reactivity with YSZ at high temperatures [82].

2.3.2.2 Cobaltites

Cobaltite materials based on $LaCoO_3$ typically display higher conductivities than other cathode materials, along with high electrochemical activity and decreased polarization resistance [7]. In particular, the $La_{0.7}Sr_{0.3}CoO_{3-\delta}$ system has been shown to have notably high oxygen diffusion and reduction properties [83]. There are several drawbacks of cobaltite cathodes, including a large thermal expansion coefficient (TEC) due to the formation of oxygen vacancies, which can lead to delamination from the electrolyte due to a large difference between the TECs of the two materials [84]. Sensitivity to these oxygen vacancies also leads them to be thermodynamically unstable in comparison to manganites [76]. Cobaltites are also highly reactive with YSZ, easily forming non-conductive interphases during sintering, so a protective interlayed is necessary, such as a thin coating of SDC or GDC between electrode and electrolyte to prevent direct interaction and eliminate subsequent raises in resistance [85, 86]. Doping of the cobalt and substitution of the A-site with an alternative cation, such as Sm or Pr, can be used as method of decreasing the TEC [7]. This type of doping, however, can often lead to a marked decrease in electronic and ionic conductivities [77]. $Ba_{0.5}Sr_{0.5}Co_{0.8}Fe_{0.2}O_{3-\delta}$ (BSCF) is another attractive cobaltite due to its high electrochemical activity but the high TEC and severe reactivity with GDC and YSZ at high temperatures makes it a poor choice for SOFC cathodes [87, 88].

2.3.2.3 Ferrites

Ferrites of the $LaFeO_3$ (LFO) based system, particularly Sr-doped lanthanum ferrite (LSF), have shown promising performance and stability in comparison to cobaltites, along with a decrease in reactivity with YSZ and a lower TEC [75]. Total conductivity levels of ferrites are dominated by electronic conductivity rather than oxygen ion transport, though moderate doping levels of Sr will increase oxygen vacancies [76, 89]. While lower than those of cobaltites, he TECs of ferrites are still significantly higher than those of manganites, due to a high chemical expansion which can translate into poor compatibility with commonly used electrolytes. This can be suppressed by doping of the Fe site, but can lead to decreases in electronic and ionic conductivities [90].

A well-known variant of LSF with doping of both the A-site and the B-site is $La_{1-x}Sr_xFe_{1-y}Co_yO_{3-\delta}$ (LSCF), where the oxygen nonstoichiometry enhances ionic conductivity. LSCF is well known for having good electrical conductivity and oxygen activity [91]. The varying valency of Fe and Co, which can exist in 2+, 3+, or 4+ valencies, readily creates an oxygen nonstoichiometry in LSCF and enhances ionic conductivity [92]. Higher levels of Fe result in a lower δ, as Fe is more stable than Co, and an increase is cause by increasing levels of Sr [93]. However, ionic conductivity is affected more by Sr content and the Fe and Co content primarily affects the electrical conductivity [7]. LSCF with moderate to high doping can increase conductivity and oxygen reduction rates, but negatively affect thermal stability [94]. An example of a moderately doped LFO is $La_{0.6}Sr_{0.4}Fe_{0.8}Co_{0.2}O_{3-\delta}$, which provides a good balance between the thermomechanical, electrical, and conductive properties, along with good compatibility when used with ceria-based electrolytes, though the high level of Sr content will raise the TEC [76]. Introducing an A-site deficiency, such as in $La_{0.6}Sr_{0.2}Co_{0.2}Fe_{0.8}O_{3-\delta}$, can lower the TEC to values more compatible with common electrolytes [95, 96]. Although less reactive to zirconia than manganites and cobaltites, ferrites will still form low conductivity $La_2Zr_2O_7$, so an intermediate layer between cathode and electrolyte is appropriate [97]. Table 10 shows the TEC, electronic, and ionic conductivities of numerous perovskites in air at varying temperatures, showing their potential for use in reduced operating temperature SOFCs.

Table 10 - Performance data of several perovskite materials studied for use as cathodes, compiled by [7].

Composition	TEC ($x10^{-6}K^{-1}$)	T (°C)	σ_e (Scm^{-1})	σ_i (Scm^{-1})
La0.8Sr0.2MnO3	11.8	900	300	$5.93x10^{-7}$
La0.7Sr0.3MnO3	11.7	800	240	-
La0.6Sr0.4MnO3	13	800	130	-
Pr0.6Sr0.4MnO3	12	950	220	-
La0.8Sr0.2CoO3	19.1	800	1220	-
La0.6Sr0.4CoO3	20.5	800	1600	0.22
La0.8Sr0.2FeO3	12.2	750	155	-
La0.5Sr0.5FeO3	-	550	352	-
	-	800	369	0.205
La0.6Sr0.4FeO3	16.3	800	129	$5.6x10^{-3}$
Pr0.5Sr0.5FeO3	13.2	550	300	-
Pr0.8Sr0.2FeO3	12.1	800	78	-
La0.7Sr0.3Fe0.8Ni0.2O3	13.7	750	290	-
La0.8Sr0.2Co0.8Fe0.2O3	20.1	600	1050	-
La0.8Sr0.2Co0.2Fe0.8O3	15.4	600	125	-
La0.6Sr0.4Co0.8Mn0.2O3	18.1	500	1400	-
La0.6Sr0.4Co0.8Fe0.2O3	21.4	800	269	0.058
La0.6Sr0.4Co0.2Fe0.8O3	15.3	600	330	$8x10^{-3}$
La0.4Sr0.6Co0.2Fe0.8O3	16.8	600	-	-
La0.8Sr0.2Co0.2Fe0.8O3	14.8	800	87	$2.2x10^{-3}$
La0.8Sr0.2Co0.8Fe0.2O3	19.3	800	1000	$4x10^{-2}$
La0.6Sr0.4Co0.9Cu0.1O3	19.2	700	1400	-
Pr0.8Sr0.2Co0.2Fe0.8O3	12.8	800	76	$1.5x10^{-3}$
Pr0.7Sr0.3Co0.2Mn0.8O3	11.1	800	200	$4.4x10^{-5}$
Pr0.6Sr0.4Co0.8Fe0.2O3	19.69	550	950	-
Pr0.4Sr0.6Co0.8Fe0.2O3	21.33	550	600	-
Pr0.7Sr0.3Co0.9Cu0.1O3	-	700	1236	-
Ba0.5Sr0.5Co0.8Fe0.2O3	20	500	30	-
Sm0.5Sr0.5CoO3	20.5	700-900	>1000	-
LaNi0.6Fe0.4O3	11.4	800	580	-
Sr0.9Ce0.1Fe0.8Ni0.2O3	18.9	800	87	0.04

2.3.2.4 Nickelates

Nickelates of the form $LaNiO_{3-\delta}$ are attractive due to their electrochemical, thermal stability, and electronic conductivity properties but are unstable at high temperatures due to phase transformations [98, 99]. These phase transformations can be prevented by moderate doping of the Ni site, such as with $LaNi_{0.6}Fe_{0.4}O_3$ (LNF) which has been shown to have high electrical conductivity, phase stability, a TEC value close to that of common electrolytes, and high catalytic activity [98]. LNF is, however, even more reactive towards the formation of non-conductive $La_2Zr_2O_7$ than conventional LSM at high temperatures [99, 100]. Other nickelates of recent interest include $La_2NiO_{4+\delta}$ compounds which have a K_2NiF_4 structure described as alternating layers of perovskite and rock salt, as shown in Figure 24.

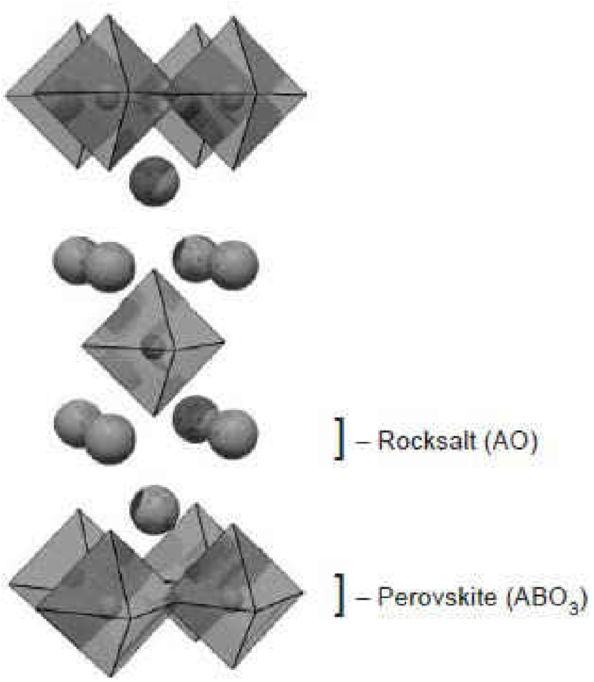

Figure 24 - K_2NiF_4 structure of La_2NiO_4 of alternating perovskite and rock salt layers [101].

These compounds are attractive due to high electronic conductivity, moderate TECs, and a high concentration of oxygen interstitials due to the layered structure, which leads to high oxygen ion transport [101]. It has also been reported that these structures will experience structural transformations due to heating, such as $La_2NiO_{4+\delta}$ changing from orthorhombic to tetragonal at temperatures above 150°C, making it unstable for cathode use [102]. Structural changes can be suppressed with doping, along with lowering of the TECs to levels closer to electrolyte values [76].

2.3.2.5 Composites

Composites utilizing nearly all of the aforementioned cathode types have been of interest due to various advantages presented by pairing one of these materials with an electrolyte material. These advantages can include lower thermodynamic strains due to better matching TECs between components and significant extension of the TPB reaction zone into the cathode bulk [77]. The addition of 30-50 wt% $Ce_{0.8}Gd_{0.2}O_3$ to $La_{0.6}Sr_{0.4}Co_{0.2}Fe_{0.8}O_3$, for example, resulted in a decrease by an order of magnitude in the polarization resistance of pure LSCF and enhanced overall cathode performance [103]. Similar results have been reported for composites utilizing LSM, such as LSM-YSZ and LSM-$Sm_{0.2}Ce_{0.8}O_{1.9}$ (SDC), though the former may still have problems from the formation of low conductivity zirconates [104].

2.3.3 Manufacturing

As with manufacturing of anodes, cathodes can benefit from a graded construction of a fine active layer at the electrolyte interface and a coarser, thicker layer on top to promote gas diffusion and electron transfer from the external circuit. Many of the same techniques used for creating graded anodes can be applied to cathodes, and easily up-scalable processes are the typically accepted norm. This includes screen printing inks of different compositions or making tapes of different compositions, punching discs, and laminating them together. Cathode-supported structures are not typically used due to a high overpotential/polarization losses and restricted gas flow resulting from the thick cathode structure [11].

2.3.3.1 Screen Printing

The screen printing method is a reliable one in which the thickness and quality of prints is easily reproduced and controlled, and is up-scalable. Inks are typically produced using a roll mill, ball mill, or automatic grinder [105, 106]. The pastes produced from milling are then used with a commercial screen printer using a steel mesh screen stenciled using emulsion to precisely print electrodes onto electrolytes.

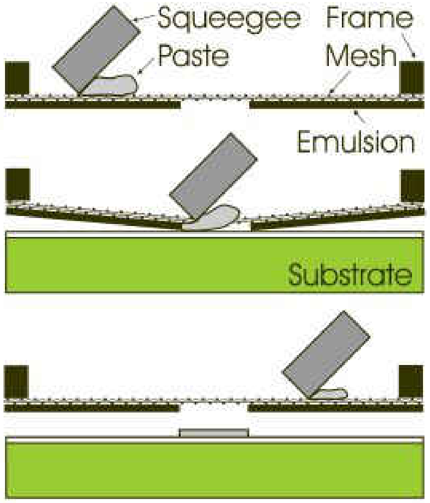

Figure 25 - Screen printing process [26].

2.3.3.2 Tape Casting

Liu et. al [107] used the tape casting process to produce complete cells of Ni/YSZ anode, YSZ electrolyte and LSCF cathode. The anode and electrolyte were co-casted and co-fired, an LSCF tape was casted and discs were applied to the sintered half calls using a gadolinium-doped ceria (GDC) buffer layer applied by slurry coating to act as the bond between the cells and the LSCF discs. This buffer layer acted both to bond the surfaces together and prevent the formation of $La_2Zr_2O_7$. Using the slurry coating process resulted in a dense homogeneous coating across the entirety of the electrolyte with a strong bond between the GDC and LSCF. The tape casting method is an easily controllable and reliable method of producing samples, and this method could help to bring down overall production costs, due to a minimization in necessary equipment and reduction of production times.

2.3.3.3 Composite Manufacturing

Composites can be manufactured in a number of ways, depending on the type of structure desired and the ratio of solids being used. The easiest way to do this is to use traditional powder blending techniques of mixing and milling appropriate proportions of powders together for an extended period of time to achieve homogeneity, such as is typically done with anode cermets. The mixed powders can then be made into a slurry or ink for spray coating or screen printing, such as the LSCF-GDC composite by [108]. The other largely used method is to use an impregnation, or infiltration, method where a single phase electrode, such as LSM, is produced in a traditional manner such as by screen printing and subsequent sintering followed by impregnation of an ionic conductor, such as SDC, into the porous framework [104]. The reverse process was also done, using an SDC lattice and impregnating it with LSM, and provided a lower polarization resistance than impregnating an LSM electrode with SDC or using the conventional screen printing of mixed powders. Structurally graded components can also be constructed using conventional techniques such as screen printing, spray painting, or tape casting. A fine structured active layer is first sprayed onto the electrolyte surface and sintered using composite slurry created from mixing powders and then the larger grained upper surface is subsequently sprayed and sintered, or a disc from a green tape can be applied to fine structure and sintered to produce similar results [109]. Compositionally graded structures, such as those presented in Figure 26, have also been created in a similar manner, spray painting compositionally varied layers of 3YSZ, LSM, and LSC onto a YSZ electrolyte to create a functional gradient within the cathode [110]. Spray deposition techniques such as those described previously in section 2.2.3 have also been used to successfully create LSM-YSZ composite cathodes [56].

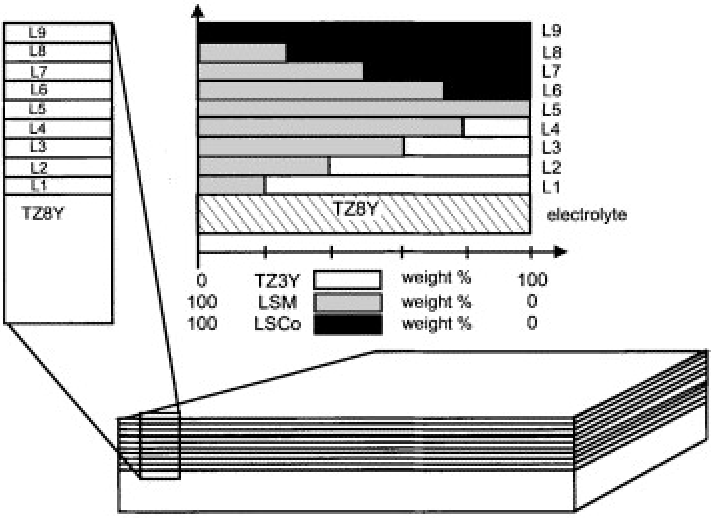

Figure 26 - Compositionally graded composite cathode produced by spray painting [110].

2.3.3.4 Pulsed Laser Deposition

Other techniques such as pulsed laser deposition have been explored to control the microstructural aspects of composite cathodes [111]. Using a sintered LSC-GDC composite pellet as the laser's target, the porosity of the composite layer could be controlled by changing the ambient conditions of the deposition environment, allowing for enhancement of adhesion between cathode and electrolyte and tailoring of microstructure.

2.3.3.5 Intermediate Layer

Many of the cathode materials which have been discussed have severe reactivity with common electrolyte materials, especially when employing YSZ. These materials, such as LSM or LSCF, can react with the YSZ to form non-conductive interphases such as $La_2Zr_2O_7$, lanthanum zirconate, degrading cell performance. In order to prevent the formation of these insulating phases, the thin film processes such as spin coating and spray deposition are often used to apply a protective intermediate layer between then electrolyte and cathode. An effective material choice for the intermediate layer is GDC, as it has high conductivity and low reactivity towards both YSZ and common cathode materials [51]. It has been found that using an intermediate layer of GDC between YSZ and $La_{0.6}Sr_{0.4}Co_{0.2}Fe_{0.8}O_{3-\delta}$ can significantly improve electrode performance as interphase formation is suppressed; however, there is a rise in polarization resistance associated with the GDC coating. It was shown that using an LSCF-GDC composite in conjunction with the GDC intermediate layer not only suppressed this, but further increased performance by further lowering resistances [112]. Similarly, cells constructed using cobaltite-based $Sm_{0.5}Sr_{0.5}CoO_{3-\delta}$ as cathodes with a thin GDC layer between the cathode and the

YSZ electrolyte experienced a decrease in performance of only 3% after 12 hours of operation, as opposed to those without the GDC layer which decreased by 23% [113]. It is, therefore, recommended that a thin intermediate layer be applied to the cathode side of ZrO_2-based electrolytes when using common perovskite cathode materials.

2.3.4 LSCF Structural and Material Properties

Lanthanum strontium cobalt ferrite (LSCF), as described previously, has a perovskite structure and good electrical and electrochemical properties. Specifically, $La_{0.6}Sr_{0.4}Co_{0.2}Fe_{0.8}O_3$ is a compound with desirable characteristics, as increasing content of Fe in the B-site results in a decrease in TEC, making it more thermodynamically compatible with common electrolytes than a compound with high Co content [114]. The substitutions of La and Fe with Sr and Co, respectively, in $La_{0.6}Sr_{0.4}Co_{0.2}Fe_{0.8}O_3$ are randomly distributed throughout the crystal causing distortions and vacancies throughout the crystal, affecting its properties and structure.

LSCF has a rhombohedral structure at room temperature, with angle $\alpha \approx 60.3°$ and pseudo-cubic lattice constant $a \approx 3.86$ [96, 114]. With the increase of temperature, α approaches closer to 60°, which leads to a second order phase transition (no discrete volume or enthalpy change) from rhombohedral to cubic occurring between 700-800°C and varies slightly with variation in Co content [115]. Above this temperature, α stays constant around 60°, and the pseudo-cubic lattice parameter expands slightly from 3.87Å at room temperature and up to around 3.91Å around 800°C, as shown in Figure 27 [114, 115]. Figure 27 also shows the increasing lattice parameter with an increase in Fe content.

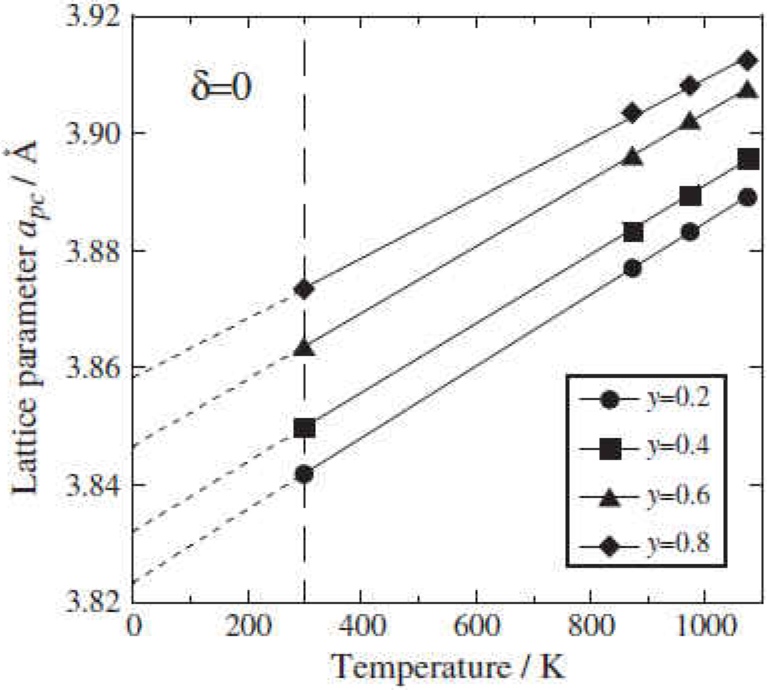

Figure 27 - Expansion of lattice due to increase in Fe content, y, and temperature [114].

The phase transition was also accompanied by an increase in Young's modulus and material stiffness. As received samples of room-temperature rhombohedral LSCF in [115] had a Young's modulus of 102 ± 4 GPA while samples annealed at 900C, which above the transition temperature, had a Young's modulus of 139 ± 3GPa. Strength of the LSCF compound is also affected by composition; an increase in Sr content causes a decrease in the fracture strength, as does nonstoichiometry [116]. Table 11 shows a decrease in fracture strength of 10 MPa with a 20% increase of Sr and a 46 MPa decrease with the introduction of an A-site deficiency. There is also a general trend of strength increasing with temperature, though this doesn't seem to be the case for the compound in which an A-site deficiency is present.

Table 11 - Fracture stress for some perovskite materials [116].

Material	Strength (MPa)	Test method
$LaFeO_3$	202±18 (RT) 235±38 (800 °C)	4-point
$La_{0.5}Sr_{0.5}CoO_{3-\delta}$	138±12 (RT) 181±18 (800 °C)	4-point
$La_{0.5}Sr_{0.5}Fe_{0.5}Co_{0.5}O_{3-\delta}$	121±7 (RT) 181±13 (800 °C)	4-point
$La_{0.5}Sr_{0.5}Fe_{0.25}Co_{0.75}O_{3-\delta}$	71±7 (RT) 120±11 (800 °C)	4-point
$La_{0.8}Sr_{0.2}Fe_{0.8}Co_{0.2}O_3$	165 (RT)	Biaxial
$La_{0.6}Sr_{0.4}Fe_{0.8}Co_{0.2}O_3$	155 (RT)	Biaxial
$La_{0.5}Sr_{0.5}MnO_3$	78 (RT) 200 (800 °C)	4-point
$La_{0.58}Sr_{0.4}Fe_{0.8}Co_{0.2}O_3$	109±9 (Apparent value linear theory, RT) 70±6 (Considering non-linearity, RT) 66±10 (800 °C)	Biaxial

Electrical conductivity rises with temperature and drops with an increasing Sr-deficiency, as shown in Figure 28. Oxygen nonstoichiometry also causes a reduction in electrical conductivity due to a decrease in the presence of charge carriers by oxygen vacancy formation, though it should cause a slight rise in ionic conductivity [91].

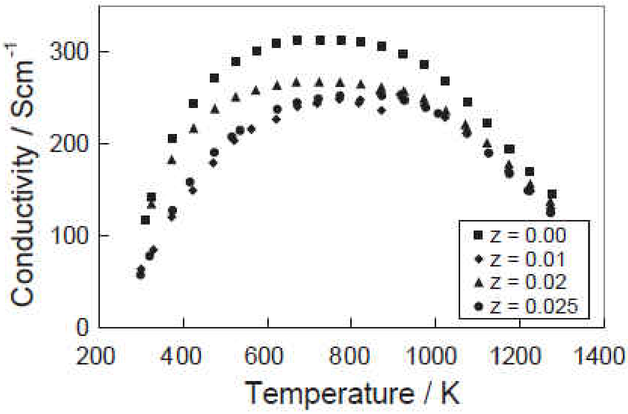

Figure 28 - Effects of temperature and Sr-deficiency of La0.6Sr0.4-zCo0.2Fe0.8O3-δ on conductivity [96].

CHAPTER 3: EXPERIMENTAL

This section will contain descriptions of all of the different processes used to create single SOFCs along with some of the theory behind the methods and the equipment used. These processes will be separated by category of which cell component they relate to; the electrolyte, electrodes, or the whole cell. They are listed mostly in chronological order of manufacturing a single cell from raw powders to finished product and evaluation methods of said cells. However, the electrolyte, GDC interlayer, and each electrode are all sintered independently after their respective manufacturing processes have been completed. As such, in the interest of brevity, the sintering process is listed as an all-cell process, although sintering is done repeatedly throughout the manufacturing process.

3.1 Electrolyte Specific

3.1.1 Slurry

Electrolytes are produced by tape casting a thin film of slurry onto a moving substrate. The first step to the tape casting process is to develop the slurry, correctly assembling its constituents to make sure they interact in a favorable manner and impart the desired properties. The slurry is composed of the primary powder of which the electrolyte is composed of several different parts, each of which serves a different purpose.

In the primary mixing step, the electrolyte powder, either YSZ or SCSZ, is mixed with xylene and ethanol solvents and blown menhaden fish oil dispersant in a rolling mill within a bottle containing mixing media, which will be described in more detail in the following section. The purpose of the solvent is to dissolve the other ingredients, and needs to be chosen accordingly so it effectively dissolves the other ingredients to create a homogenous mixture. The solvent used must evaporate steadily and equally throughout the tape to prevent the premature formation of a dry skin at the top of the tape, homogenizing the tape throughout its thickness. The dispersant, or deflocculant, in the mixture is used to spread the electrolyte powder and keep them separated in a homogeneous suspension. This allows for all of the particles to be evenly and thoroughly coated with other additives, and prevents the formation of agglomerates which can trap air in the slip. Menhaden fish oil is the most popular dispersant as it is a very effective homogenizer and deflocculant due to the large variety of fatty acid chains contained within it. It also acts as a type II plasticizer, which will be explained shortly, and is often called a lamination aid [49].

During the secondary mixing step binders and plasticizers are added to the slip followed by a continuation of the milling process. The binder supplies a network polymer chains which holds all of the particles together as a system, forming a film, and can have a large effect on the final tape quality. Polyvinyl butyral is a commonly used polyvinyl resin binder and is typically used for applications where the tape will be sintered in air. The plasticizer is used to impart a flexible plastic-like characteristic to the tape, allowing it to bend without cracking and discs to be punched and laminated without cracking. Benzyl butyl phthalate, a Type I plasticizer acts as a binder solvent, softening the polymer chains to increase the flexibility. Polyalkylene glycol, a Type II plasticizer, acts as a lubricant, allowing the particles and polymer chains contained within the green tape to move easily without the need for excess force, contributing further to the flexibility of the green tape while preventing fracture. A balanced slip containing both Type I and II plasticizers will impart flexibility to the green tape which will make it easy to deform and mold, properties which will impart ease to the lamination process [49].

3.1.2 Ball Milling

The ball milling process is essential to slurry preparation, as it provides the means for all of the slurry constituents to react and mix with each other. The milling process mechanically separates the agglomerates which can form in powders through the impacting and grinding action of the tumbling media. This allows the powder to be coated with the dispersant, which will in turn help to keep the particles apart so that the other constituents of the slurry can be evenly dispersed in the slip. A rotary ball mill is a common choice, and the use of a plastic bottle reduces the energy needed to be put into the milling process. The choice of media is important to achieve proper mixing and prevent contamination or undesired interactions. The amount of media is also important, as the media needs to have enough room to move freely within the rotating bottle to cause impacts. The speed at which the mill is set has a large effect on this, as the desired effect is that the media fall at the top of its rotation, causing impacts with the slurry at the bottom. Milling times can range anywhere from 4 to 48 hours, though in the case of plasticizers at least 12 hours are necessary to ensure thorough interaction. However, excessive milling can cause undesired effects, such as changing slip viscosity beyond the usable range, and the effect on viscosity will differ for each unique slip [49].

Ball milling was done using plastic 1L bottles with cylindrical zirconia media with around 6.3mm diameter and 6.35mm length filling about 1/3 of the bottle’s volume, leaving enough space for movement once all the slurry contents are added in. As stated, this ensured that the media would be able to move enough to mix properly.

Figure 29 - Ball milling of slurry to ensure proper mixture or all components.

3.1.3 Tape Casting

Figure 30 – ProCast tape casting machine for producing electrolyte green tapes.

Tape casting, as described previously in the literature review, is one of the most popular methods for processing electrolytes. Using the slip as formed above, a doctor blade, and a tape caster with a moving carrier film, such as the ProCast TC-71LC shown in Figure 30, tapes can be made with the desired thickness. Large scale systems can use pipes or tubing to feed multiple casters from a single reservoir, while laboratory setup such as the one employed here use a doctor blade with a built in reservoir.

After development of the slip in the milling machine, the slip is separated from the milling media and degassed. This is necessary to remove any air bubbles which may be trapped in the slip which could cause defects in the tape such as pinholes, streaking, or cracking. Degassing time needs to be carefully determined to make sure all such bubbles are released, however degassing too aggressively or too long can cause evaporation of the solvents, causing large increases in viscosity or formation of a skin on top which will affect slip behavior during casting [49].

The slip is then poured into the reservoir of the doctor blade at the feed end of the tape caster. The doctor blade height is preset prior to addition of the slip using the attached micrometers, checking to make sure both micrometers are level so that tape thickness does not vary from one side to the other, and its height will be determined by factors such as slip viscosity and desired final thickness. As the carrier film moves at a constant speed, friction between the film and the slip will cause the slip to be deposited uniformly onto the carrier film.

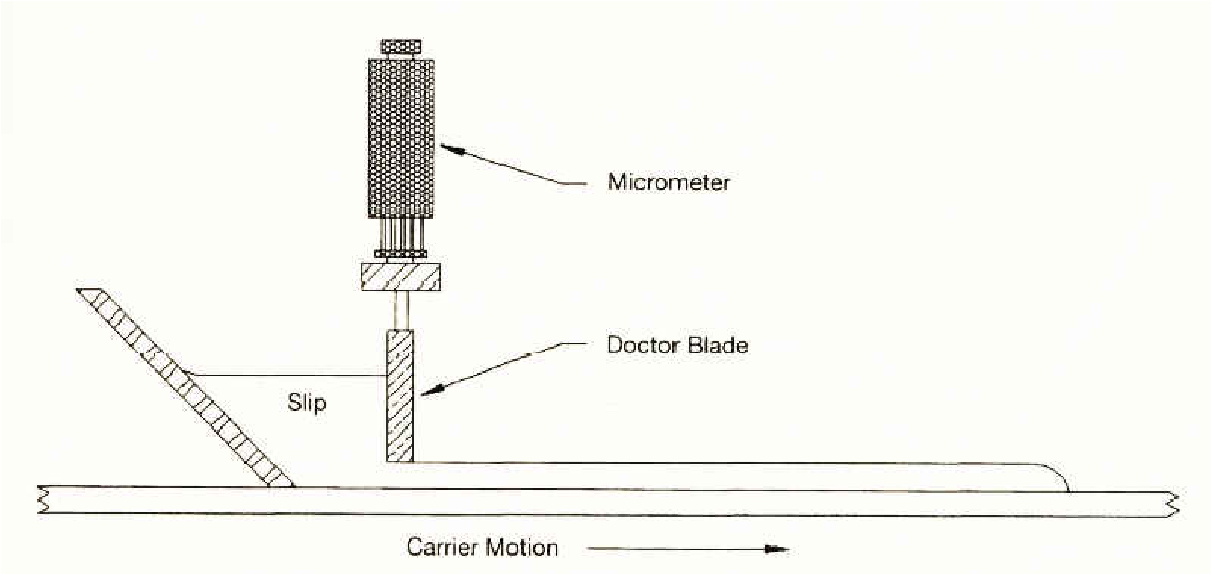

Figure 31 - Adjustable doctor blade used for tape casting [49].

It is important to note that setting the doctor blade to a specific height will not necessarily yield that height tape. There are several factors which must be accounted for which will determine final tape thickness. The most prominent of these is the viscous flow forces present at the gap of the doctor blade, as pictured in Figure 32, which will prevent the tape from being the same thickness as the gap. Evaporation of solvents and shrinkage or expansion of the film as it dries will also be a factor. If the solvents evaporate while the slip is still in the reservoir, a film or segregated dry spots could occurs which can cause blockage at the gap and affect both the final height and tape homogeneity throughout its length [49].

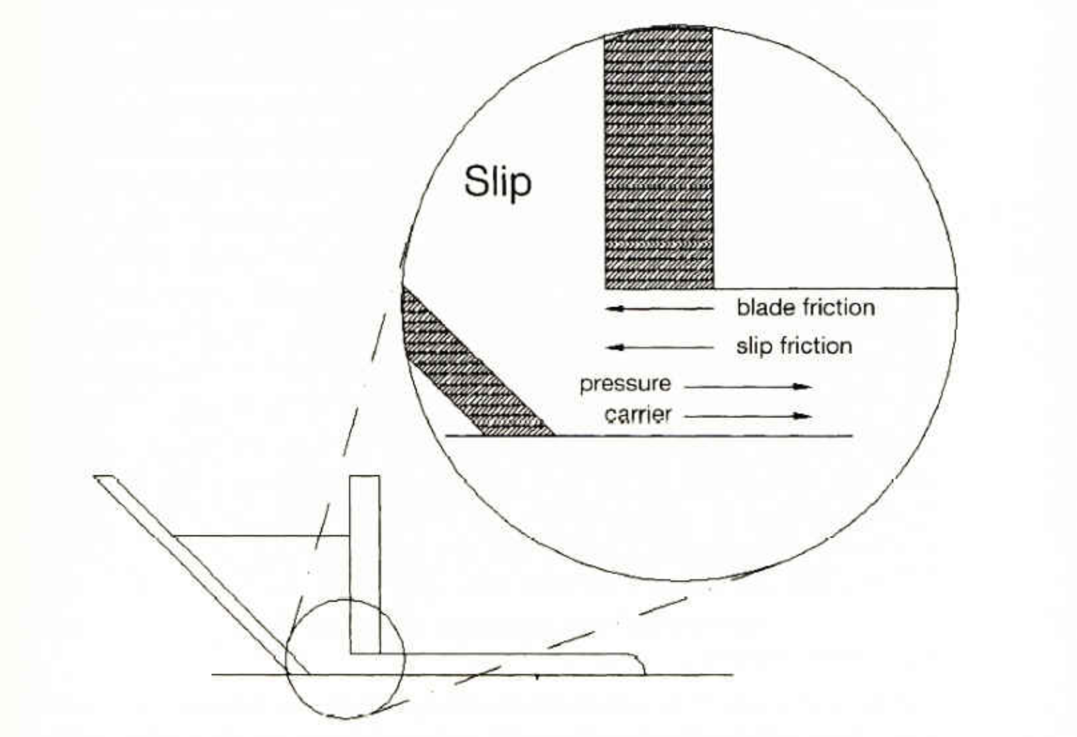

Figure 32 - Forces which cause differences in tape height vs. doctor blade height [49].

3.1.4 Punching and Lamination

After casting, the tape is then left to dry, allowing enough time for all solvents to evaporate steadily in a controlled atmosphere. Atmospheric conditions such as temperature and humidity should be kept constant during this time so as not to affect evaporation rates which could cause premature skin formation, trapping solvents below the surface. A metal punch is used to create discs from the green tape to be laminated and sintered together to from electrolytes. The size of the punch must be selected according to the sintering properties of the materials being used, as samples will shrink during sintering. Therefore, it is necessary to know by how much the sample will shrink to properly size the punch for making discs from the green tape.

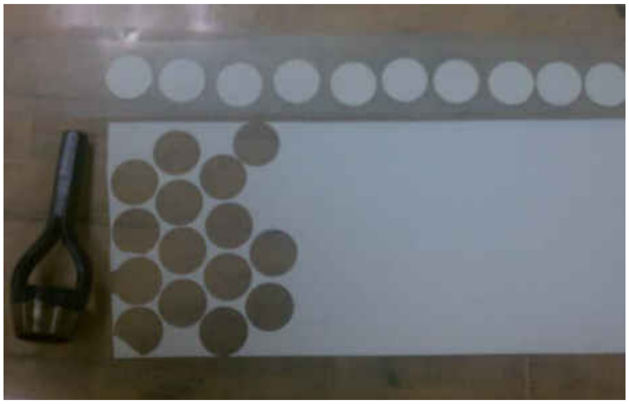

Figure 33 - Punching discs from electrolyte green tape.

Lamination is the key process to fabrication of multi-layered ceramics, and depends on three key parameters: time, pressure, and temperature. Proper lamination will allow the multiple layers to sinter into a single structure and prevent delamination from occurring. These setting will vary on the size, thickness, and composition of the tape and the number of layers being used to create the electrolyte. The temperature will depend mainly on the organics used within the slurry and the time and pressure will be affected by the overall thickness of the layered structure. Layers should be stacked with the top surface of each layer being in contact with the bottom surface of the layer on top of it, so as to prevent delamination from a deficiency of binder between the two surfaces due to existence of binder gradients which can occur in tapes [49]. Enough time should be used so that the entire structure can be thoroughly heated during pressure, and the pressure should be high enough to provide sufficient contact between layers but low enough to avoid deformation of the structure.

Certain procedures may be incorporated to homogenize the laminated layers due to thickness gradients which can occur in green tapes and can lead to defects after sintering. Such procedures include rotation of disc layers to average out thickness differences and rotation of the stack within the press during lamination. Rather than a single lamination period, multiple shorter periods are used with the stack being rotated. The stack is rotated so as to even out the pressure distribution on the sample being pressed, averaging the amount of pressure throughout the stack. This avoids the creation of stress concentrations due to uneven pressure application caused by misaligned press platens [49]. A Carver heated automatic press and a stainless steel 40 mm die were used for laminating the layered electrolytes.

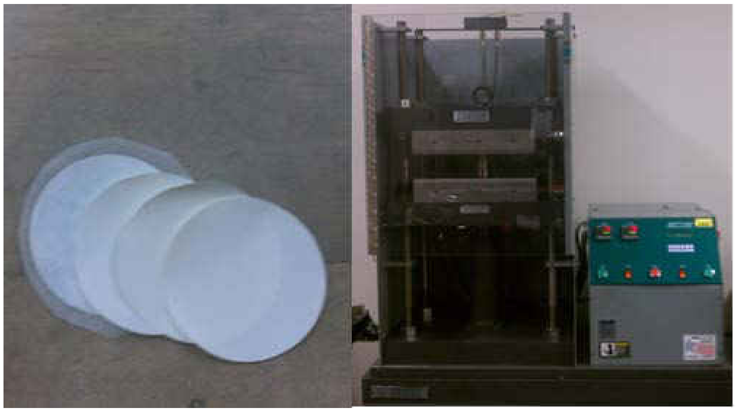

Figure 34 - Laminating and pressing of green tape discs.

3.2 Electrode Specific

3.2.1 Spin Coating

Deposition of the thin intermediate layer was done using a Specialty Coating Systems G3 Desktop Spin-coater to spread a suspension of GDC over the surface of the electrolytes as described in section 2.2.3. The spin-coater is connected to the building's air supply, rated to 60psi, which supplies the 0.55scfm of air necessary to purge the system and maintain positive pressure. A 4cfm vacuum pump provides the vacuum to bond the spinning sample holder and the electrolyte to keep the sample from flying off the chuck. The coater will not operate without these two lines properly connected and operating. All aspects of the spin coating routine are programmable, and small changes will affect the final quality of deposition. Speed and time of spin coating recipes will be largely affected by the dynamics of the fluid and the size of the substrate being used. The solution used for spin coating is a GDC suspension, 10 wt% GDC in ethanol, mixed by ultrasonic dispersion.

Figure 35 - Spin-coater with vacuum pump set up in ventilation hood and connected to building air supply.

3.2.2 Ink Processing

Pore formers are mixed in with the electrode powders in order to ensure a high level of porosity in the final microstructures. Pore formers are used to achieve a highly connected pore matrix within the sintered electrode. For purposes of easing gas diffusion and extension of the TPB, a porosity of around 40% is desired. Several pore formers were tested and results were evaluated using a scanning electron microscope. Electrode powders are mixed with pore formers in a plastic bottle with using spherical 5.3mm diameter zirconia mixing media. About 1/3 of the bottles volume is filled with media. Theoretically, the remaining 2/3 is filled with acetone and the desired combination of powders, such as the 60 vol% electrode – 40 vol% pore former used here, with the amount of each being measured out to theoretically fill 1/3 of the bottle's empty volume. As the media is spherical, however, mixing all of these into the bottle does not actually fill it and still leaves plenty of room for the media and the other constituents to move and achieve thorough mixing action. After mixing for 24 hours on the ball mill, the slurry is separated from the mixing media using a large sieve to catch the media which is then rinsed using acetone sparingly so as to recover as much of the mix as possible but not to add too much solvent to the mix and increase dry time. The mixture is then dried using a glass tray on a hot plate set to a low to medium heat setting to evaporate the solvent, the mixture is stirred constantly with a spoon to prevent agglomeration or separation of the constituents in any part of the tray. After all of the solvent has evaporated the resulting solids are sieved through a fine-mesh sieve to separate agglomerates and achieve homogeneity in the final product. The resulting mixtures can then be used to produce inks.

Ink manufacturing for application of electrodes was done via Keith Machinery 3-roll mill used to mix a terpineol vehicle with the electrode powders. The grinding action of the mill's rear rolls spinning towards each other breaks apart any agglomerates in the powder and the recirculating terpineol causes the powders and the vehicle to mix together. Gradual addition of the powder to the mill, rather than addition of the full amount, further prevents creation of agglomerates on the mill. Ink consistency and texture can be controlled by minute adjustments being made to the gaps between rollers. Control must be practiced to allow enough material to pass between the rollers to achieve the right level of mixing and grinding, but not cause excessive force on either the powder or the rollers. Too large of a gap will allow agglomerates to pass unbroken and material could drop from the rollers. Milling should only be done so long as it is necessary to form a homogeneously mixed paste with favorable texture. Excessive milling times can result in changes to ink texture or consistency due to excessive grinding or increased temperature from friction. Temperature can be controlled through the use of a water cooling system to keep the mill at a certain level, preventing excess heat transfer to the ink or damage to the mill due to expansion of the rollers from the high heat.

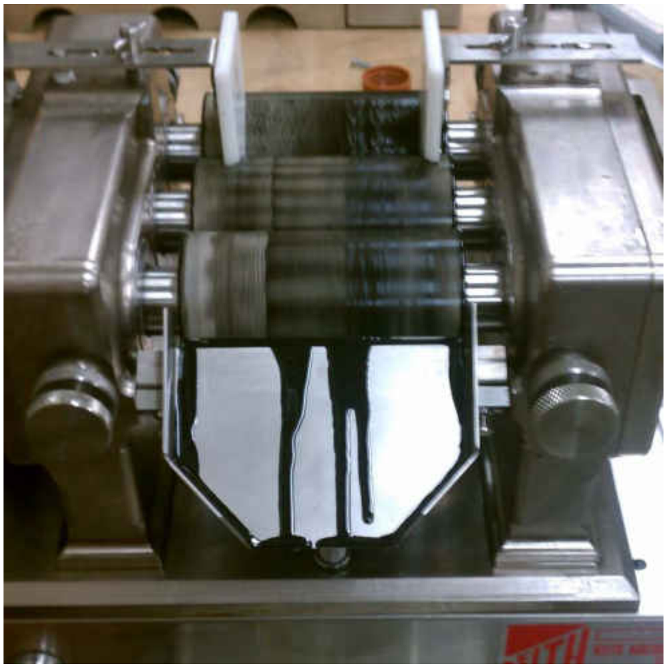

Figure 36 - Cathode ink production using Keith machinery 3-roll mill.

3.2.3 Screen printing

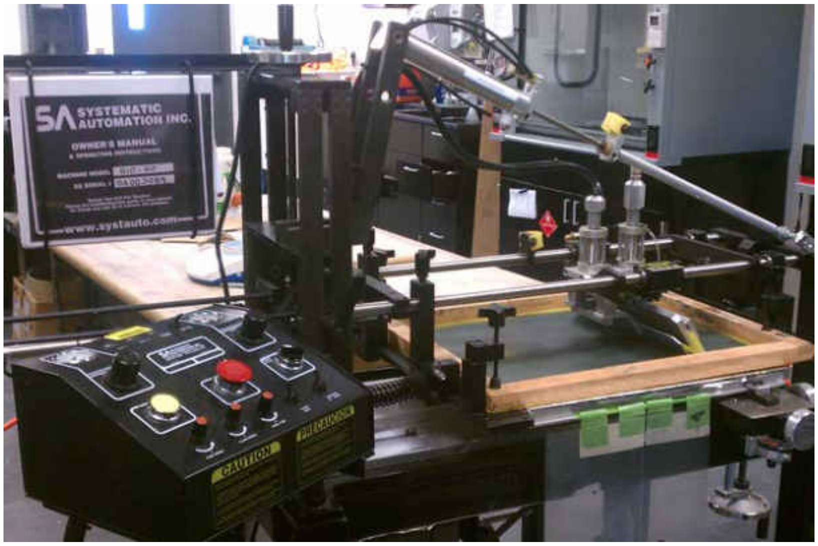

Figure 37 - Screen printing apparatus for application of electrodes to electrolyte.

Finished inks are used for application of electrodes onto the electrolyte via the screen printing method. A Systematic Automation 810-20 screen printer, pictured in Figure 37, was used to print the electrodes. The electrolytes are placed on the vacuum table which will hold them in place during ink transfer so that they do not stick to the screen. Pressure on the deposition stroke of the printer is set so as to transfer ink to the entire desire surface of the electrolyte and no higher, using the lightest possible amount of pressure minimizes the stress transferred to the electrolyte and minimizes the possibility of fracture. It will also leave a larger gap between the two surfaces and allow for maximum ink transfer, minimizing the number of prints required.

Accurate printing is achieved by using a fine mesh screen with negatives stenciled onto its surface. Everything except the area through which the ink is made to pass is covered in a nonpermeable emulsion which will prevent loss of ink or undesired transfer of ink through the mesh, printing only where the mesh is left intentionally blank. Ink is added generously to the screen to ensure full coverage of the deposition during printing when the squeegee blade forces the ink to pass over the open mesh. Referring back to Figure 25 in section 2.3.3, the squeegee moves the ink on the emulsified surface of the screen, pushing it through the open mesh as it passes over the electrolyte depositing a thin layer of electrode ink. After each deposited layer is dried in a furnace, the cell can be realigned using markings on the vacuum table and the screen itself to ensure accurate deposition and layering of prints. The number and quality of prints will be largely determined by the viscosity of the ink produced and its adherence to the surface and microstructure can be affected by the drying routine used for each layer. Both the number of prints required and the drying routine were determined through several iterations of testing for each.

3.3 All-cell Processes

3.3.1 Viscosity

Figure 38 - Brooksfield DV-II+ Pro viscometer.

A Brooksfield DV-II+ Pro rotary viscometer with a small sample adapter and a variety of different size spindles were used to measure the viscosities of several components during the manufacturing process. Namely, the viscosities of the electrolyte slurries, terpineol for inks, and manufactured inks were all measured.

The viscosity of a liquid is a measure of the fluid's resistance to flow or shear when a stress is applied to it. A rotational viscometer such as the Brooksfield model shown in Figure 38 operates on the principle that the resistance that a fluid has to flowing will be the same resistance that the fluid will impose on something moving within it. Therefore, the rate of rotation of a solid shape in a viscous medium can be measured by applying a known torque required to move the object in the viscous medium at a constant angular velocity to find that fluid's viscosity. The higher the force required to be applied to rotate the object in the viscous medium, the higher that medium's viscosity is [117].

3.3.2 Sintering

Sintering is done to join a mass of particles, the ceramic powders from which we want to create a structure, into a single mass by heating to 50-80% of the melting temperature. Rather than melting the material to form a continuous mass, sintering joins particles by atomic diffusion of solids, known as solid-state sintering. The sintering behavior of a material can be affected by several factors, including particle size and distribution, defect concentration, mobility, dopants, and atmospheric conditions. Transport of matter in sintering occurs by thermally-activated diffusion of atoms or ions by defect migration between particles, joining them together [118]. Sintering of each component is done independently of the other cell components after each stage of component manufacturing; electrolytes are sintered after lamination, GDC is sintered after spin coating, and each electrode is sintered after screen printing, for a total of 4 different sintering routines for each single cell. This can impose a limitation on cell production as the most cells that can be produced at one time is dictated by how many can fit in the furnace for sintering at one time.

Sintering for all of the components of the SOFCs produced here was done in air with no application of outside pressure. As such, the driving force for sintering of particles is that of the curvature of particle surfaces in contact. Through sintering, the particle mass can form a dense body which will result in a reduction of surface free energy, which provides the motivation for sintering. There are several mechanisms which can be simultaneously active during the sintering process which either affect densification of the material or grain growth. These are explained in Figure 39. While all of these mechanisms contribute to the bonding between particles, only 4-6 lead to densification by shrinkage of the particles. Due to the ability of more than one mechanism to be active at any one time, it can be very difficult to predict sintering characteristics of a structure. As such, it is necessary to find the parameters for sintering which achieve both a low, controlled rate of grain growth with an increase in densification rate [118].

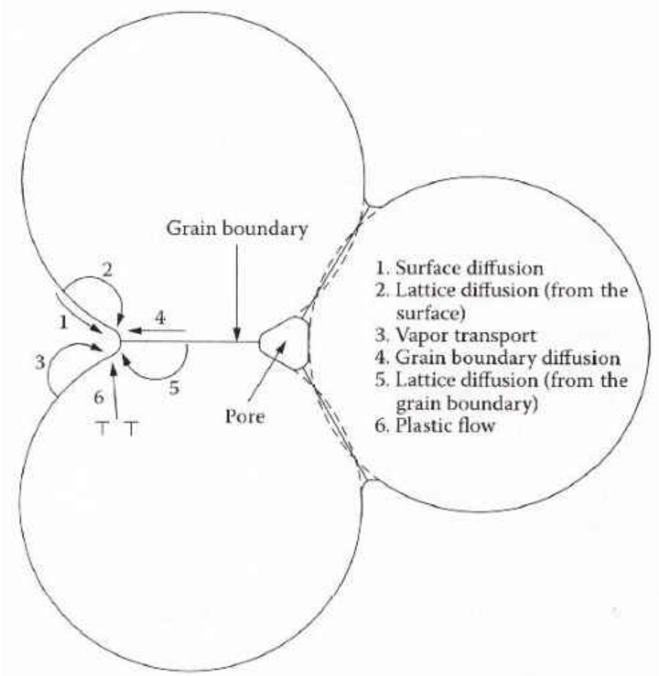

Figure 39 - Several of the different mechanisms which can contribute to sintering of particles numbered and labeled for a three-particle system [118].

Classification of sintering behavior can be achieved by sintering identical samples in varying temperatures, keeping all other factors constant. Samples were created using 2g of each respective powder in a 10mm die pressed to 20MPa. Sintering classification experiments were conducted using a Thermolyne 46100 furnace for electrolytes and twin Micropyretics Heaters International Z18-40 box furnaces for electrodes. Each component has its own dedicated furnace in order to facilitate production and limit delays attributed to long sintering times of certain components. This lets production continue in other stages using other furnaces while a certain furnace may be in use for 2-3 days at once, rather than causing a 2-3 day stall in progress. This also limits the possibility of cross-contaminating components during the sintering process. Sintering of samples at different temperatures keeping sintering conditions and heating and cooling rates constant allows for a direct comparison of temperature effects on densification of samples. From these results, necessary sintering temperatures and routines for each component can be determined to achieve ideal microstructure. This includes fabrication of high density electrolytes and high porosity electrodes with a well-connected matrix of particles.

3.3.3 Density

Characterization of sintering behavior is evaluated by using the Archimedes method to find the densities of the sintered samples. Samples are weighed using a Mettler Toledo JB1603-C high-precision scale. For closed or low porosity samples, weights were taken both in air and submerged in watered. The density is calculated using Equation 5, where ρ_s is the density of the solid sample, D is the measured dry weight, I is the weight of the sample immersed in the liquid, and ρ_l is the density of the liquid.

$$\rho_s = \frac{D}{D - I} \times \rho_l \tag{6}$$

For samples with high, or open, porosity, such as those of the cathode and anode, an additional measurement is necessary. Along with the two measurements from above, an additional measurement is required where the porous sample is once again measured in air, but with the pores filled with water. This is done by submerging the samples in water in beakers and then placing the beakers in a vacuum desiccator to evacuate the air from all of the pores and instead replace it with the water. The density formula is then modified as seen in Equation 6, where W is the weight of the wet sample in air, with its pore filled with water.

$$\rho_s = \frac{D}{W - I} \times \rho_l \tag{7}$$

These measurements are then used to calculate sample percent porosities using Equation 7, where ρ_t is the theoretical density of the sample material.

$$P = \frac{\rho_t - \rho_s}{\rho_t} \times 100\% \tag{8}$$

The theoretical densities can either be found as supplied by the manufacturers, through literature, or using Equation 8, where n is the number of atoms in the unit cell, M_A is the mass of particle A, M_B is the mass of particle B, V is the volume of the unit cell and N_A is Avogadro's number.

$$\rho_t = \frac{n[\sum_{i=1}^{i} M_i]}{VN_A} \tag{9}$$

The densities and porosities of the samples can be plotted against temperature to find the ideal sintering routines for each component of the cell, depending on the desired microstructural attributes.

3.3.4 Electrochemical Testing

Performance evaluation of single cells is done with the use of a custom built single cell test stand such as the one in Figure 40 and a multi-cell array (MCA) test stand capable of testing up to 12 cells at a time. These test stands are located at the National Energy Technology Laboratory, where all performance evaluations were conducted. The test stand is essentially a furnace with alumina tubing to support the cells and deliver the gaseous fuel and air and remove exhaust. Glass seals are used to seal the cell to the tubes to keep in gases and prevent gas crossover or leakage to the outside environment. Testing parameters such as temperature, fuel and oxidant source and flow speed, humidity, and time can all be adjusted according to the desired testing parameters and the materials used.

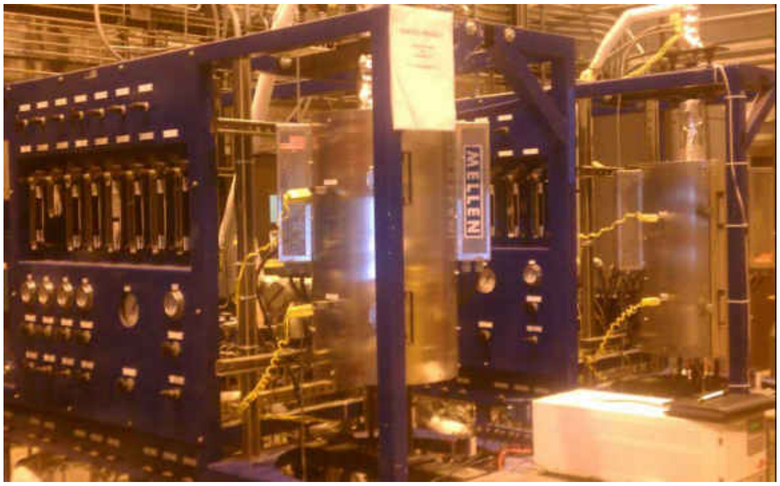

Figure 40 – NETL custom built single cell test stand.

For performance evaluation, platinum mesh current collectors were connected to the electrodes using platinum and nickel pastes to act as glue onto the cathode and anode, respectively. The mesh is welded onto the wire leads which can then be connected to the wires of the test stand to supply power and collect data. Performance evaluation involves applying a voltage across the cell and measuring the current to collect I-V data to plot the response and evaluate cell resistances. The I-V response can be used to calculate the power and current densities of the cell, which can be used to compare it to other cells and evaluate performance by comparison. Testing parameters can be varied to test cells in different environments, though the materials being used will typically dictate what temperature and fuels are best suited to each cell. The tests conducted for the cells manufactured here were constant voltage and temperature tests, which can study the effects of prolonged testing by keeping other variables constant.

3.3.5 Impedance Spectroscopy

Impedance spectroscopy is a frequency-related analytical technique which uses small-signal AC pulses to characterize the electrical properties of materials and interfaces between electrodes and electrolytes. It investigates the dynamics of bound or mobile charge carriers in the bulk or interfacial regions. Testing is typically done with symmetric cells in which identical electrodes are applied to either side of the electrolyte. This allows for more accurate analysis of the resulting spectra and makes it easier to figure out what component to attribute the resistance to and try to devise solutions to correct those faults. This can, however, be done with complete cells, though analysis may be more difficult to conduct. Tests may be conducted in varying atmospheres of neutral gas like argon or in air or a vacuum with temperature kept constant. Tests can be repeated after extended periods of operation of the cells so as to analyze the deterioration of the cells performance over time [119].

To measure impedance, cells are installed in a test stand and a single frequency voltage is applied to the interface. Measurements of the resulting current are taken to measure the phase shift and amplitude gives the real and imaginary resistances affecting the current at that frequency. The current will depend on both the ohmic resistance and the reaction rate between the interfaces. A range of different frequencies can be tested using purpose-built machines that analyze the behavior of the cells under changing conditions. The data acquired from these tests is often fitted to an idealized equivalent circuit in order help to analyze it. Modeling in this fashion can aid in the analysis of spectra to determine where certain resistance values may be originating. Microstructural aspects such as pore structure which can also affect the transport properties of the cells can typically be accounted for using theoretical models. Grains, grain boundaries between different compositions in a composite mixture, suspensions of one phase within another, and porosity can all be modeled to some extent by using equivalent circuits so that these phenomena may be more easily identified during the analysis of impedance spectra [119].

Impedance testing for the manufactured cells was done using a Solartron 1470E Potentiostat and Solartron 1252A Frequency Response Analyzer on a custom built test stand at the National Energy Technology Laboratory facility in Morgantown, WV. Frequencies in the range of 0.1Hz to 100 kHz were applied to each of the cells tested to evaluate respective impedances of each cell and find out which component may be causing the major part of the resistance to occur.

3.3.6 SEM

Microstructural analysis was conducted using scanning electron microscopy (SEM) at both the manufacturing and testing stages and sites. During manufacturing, a Zeiss Ultra-55 SEM was used to inspect the impact of changes to manufacturing processes, such as the small changes made while refining GDC application routine. During testing and latter stages of manufacturing at the NETL, a JEOL 7600 SEM was used to inspect both manufacturing changes and microstructure of cells after testing.

Figure 41 - Zeiss Ultra-55 SEM.

SEM micrographs such as those presented in Chapter 4 are constructed by directing an electron beam at the surface of the sample and then returning the signals back to the detectors. Electrons are transmitted both as electronic signals and as electrons deflected from the surface of the sample. For non-conductive samples, the sample must first be coated with a 10-100nm layer of conductive material. This is done by sputter coating in a vacuum chamber, depositing a material such as gold in an electric field onto the surface of the sample. This coating, along with conductive adhesive tape, creates an electrical connection with the metallic sample support and the sample support holder, which conducts signals back to the receptor to create SEM images [120].

Figure 42 - SOFC fragment held on metal sample holder with conductive carbon tape and sputter coated in gold to make SEM possible.

CHAPTER 4: RESULTS AND DISCUSSION

4.1 Electrolyte Processing

Electrolytes are produced from a combination of 3 mol% yttria (3YSZ) stabilized zirconia and 10 mol% scandia-1mol% ceria stabilized zirconia in the layered electrolyte design discussed in section 2.2.2. Initially, these electrolytes were produced using 8 mol% YSZ (8YSZ) rather than 3YSZ due to the increased conductivity offered by 8YSZ. However, due to differences in strength as outlined in section 2.2.4, the electrolytes produced with 8YSZ outer layers showed a tendency to fracture during screen printing of the electrodes onto the electrolyte surface. Although the Young's modulus does not vary by much at room temperature, it can be seen that the fracture toughness varies drastically between the different types of stabilized zirconia. This is likely what is responsible for the tendency of the 8YSZ cells to break during processing while the 3YSZ cells survived.

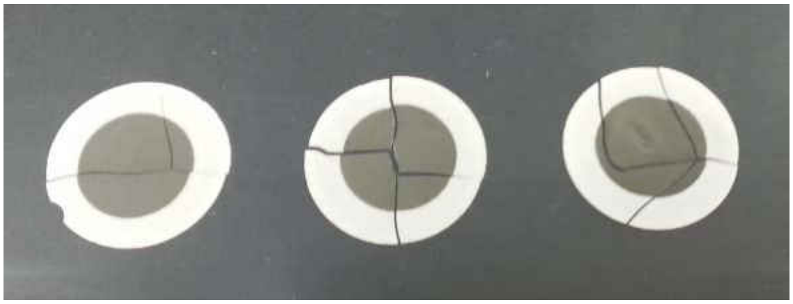

Figure 43 - Composite electrolytes with 8YSZ outer layers broken during application of anode.

Those that did not fracture during screen printing typically did not survive the rigors of electrochemical testing and the pressures of the test stand. This is likely due to the general trend of decreasing strength in stabilized zirconia with increasing temperatures. The 3YSZ electrolytes, however, survived both printing and testing, so layered electrolytes made with 3YSZ were chosen for the remainder of the electrolytes produced.

4.1.1 Slurry

Important background information for slurry preparation for producing electrolytes was outlined in the experimental section, 3.1.1 and [39, 49]. Following these guidelines, slurry mixes were developed for both the Tosoh 3mol% Y_2O_3 stabilized ZrO_2 and the Treibacher 10mol% Sc – 1 mol% Ce – stabilized ZrO2 materials used for tape casting layered electrolytes. The SCSZ slurry was mixed and casted first, followed by the 3YSZ tape. Slurry preparation consists of 2 mixing steps and grinding sessions. Table 12 shows the amounts of ingredients added during each step. For the first step, denoted as Mixture Preparation Step 1, the SCSZ powder, fish oil vehicle, and solvents are weighed to the values specified and added to a 1L mixing bottle with around 1/3 of the volume filled with 6.3mm diameter and 6.35mm length cylindrical zirconia mixing media. The bottle is then placed on a ball mill to mix the contents for 20-24h at 58rpm, ensuring that all agglomerates are separated and particles coated with fish oil dispersant. After the first mixing period, the bottle is removed from the mill and the binder and plasticizers are added in the quantities specified in Table 12 under Step 2 and mixed for another 20-24h period at 58rpm. After mixing, the slurry is immediately poured into a beaker, separating it from the mixing media. This beaker is covered with plastic film with some pressure relief holes cut into it and placed into a desiccator which is connected to a JB Industries DV-142N Platinum vacuum pump, which can pump 142 l/m as the name suggests. The vacuum pressure is slowly increased to remove all of the air in the desiccator and slurry contained until the slurry begins to bubble slowly, as shown in Figure 44.

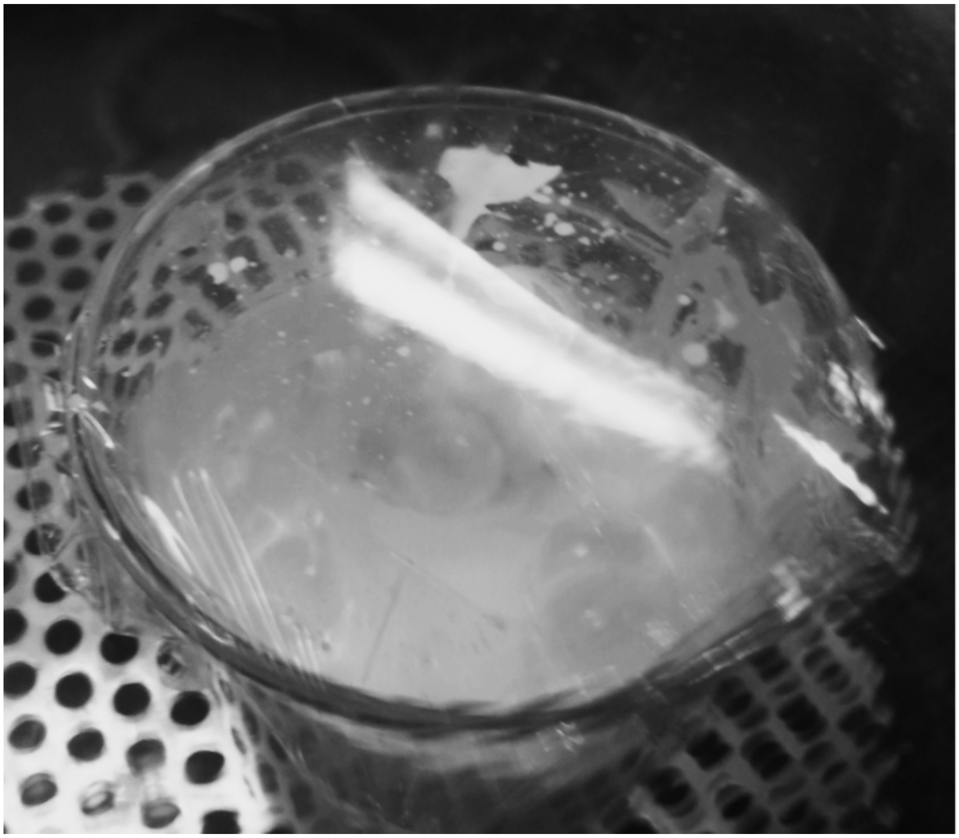

Figure 44 - Slurry bubbling steadily in a controlled manner during degassing.

The slurry is allowed to bubble for approximately 8 minutes, or until the interval between bubbles surfacing is greater than 30 seconds, to ensure the thorough removal of air bubbles. If the slurry is left in the desiccator too long, with the 30 second interval between bubbles exceeded, formation of a skin on top of the liquid can occur due to excessive evaporation of solvents, which could impact the quality of the subsequently casted tape.

Table 12 - Electrolyte slurry recipe for SCSZ.

Mixture Preparation Step 1	
SCSZ	61.94g
Menhaden fish oil blown Z-3	02.23g
Xylene	27.56g
Ethanol	27.56g
Mixture Preparation Step 2	
Polyalkylene Glycol	02.91g
Benzyl Butyl Phthalate	02.91g
Polyvinyl Butyral	05.79g

The same procedure was used for making 3YSZ slurry. The same proportions used for the SCSZ tape were initially used to make the 3YSZ tape. However, the resulting slurry was too thin and the tape produced using it was of low quality and showed pronounced streaking effects, signs of a non-homogeneously spreading slurry. This is likely due to the increased SSA of the 3YSZ (14.9 m^2/g) over the SCSZ (13.4 m^2/g,) the smaller particles having a higher SSA need a higher solids content to give a consistency similar to that of the SCSZ slurry.

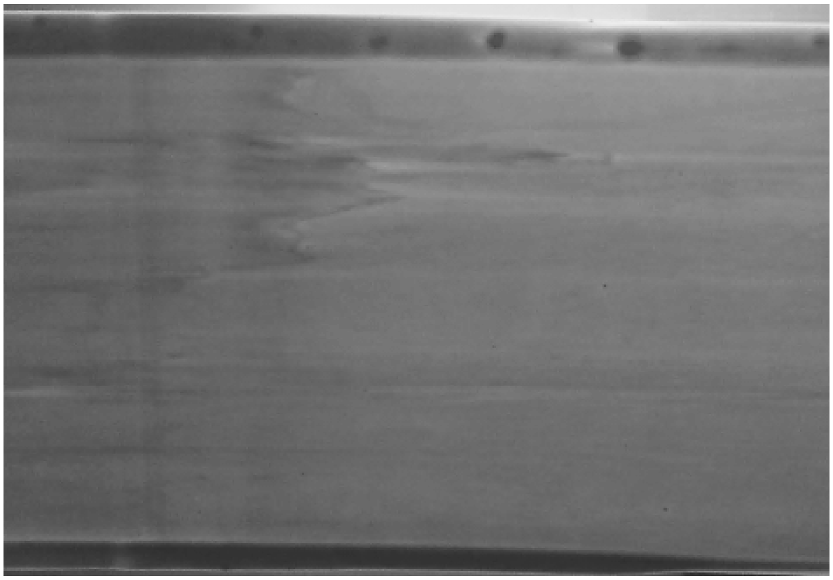

Figure 45 - Initial attempt at 3YSZ tape with unaltered slurry formula showing severe streaking.

In order to amend this issue, slight adjustments were made to the slurry mixture, increasing solids while simultaneously decreasing solvents. This had the desired effect of producing thicker slurry which could be used to produce a much higher quality tape. The final mixture is as follows in Table 13. The decrease in solvents kept the dispersant from spreading the smaller particles too far and the increased plasticizer content yielded a better bonded but still flexible network which translated into thick, but homogeneously flowing slurry.

Table 13 - Electrolyte slurry recipe for 3YSZ.

Mixture Preparation Step 1	
3mol% YSZ	61.94g
Menhaden fish oil blown Z-3	02.23g
Xylene	25.00g
Ethanol	25.00g
Mixture Preparation Step 2	
Polyalkylene Glycol	03.01g
Benzyl Butyl Phthalate	03.01g
Polyvinyl Butyral	05.79g

4.1.2 Tape Casting and Laminating

The tape casting method is used to make electrolyte tapes from slurries using compositions as outlined in Table 1 using a ProCast precision tape casting machine with a 300µm (0.0118in) gap for the doctor blade. After degassing, the slurry is immediately poured into the doctor blade set on the feed side of the tape caster.

Figure 46 - Slurry in doctor blade.

The green tape is cast with the tape caster’s collection roller speed set to 20 %, creating a tape of uniform thickness, width, and texture as seen in Figure 47.

Figure 47 - Green tape being cast.

After casting, the tapes are left to dry for at least 24 hours, and discs are punched from each of the two materials for subsequent lamination using a 31.75mm punch. Using the 31.75mm punch results in ~25mm diameter electrolytes after sintering, as shrinkage of about 24% from the unsintered discs to the sintered electrolytes was observed regardless of the original disc punch diameter used or the number of layers laminated together as seen in Table 14, which displays the differences in thickness and diameter of 3YSZ electrolytes before and after sintering.

Table 14 - Shrinkage in 3YSZ electrolytes due to sintering.

Sample Name	**Diameter, mm**		**Thickness, mm**		**ΔD**	**ΔT**
	Pre	Post	Pre	Post	% diff.	% diff.
6N	31.864	23.952	0.356	0.274	24.831	22.857
6F	31.775	24.282	0.371	0.279	23.581	24.658
4N	31.801	24.079	0.239	0.178	24.281	25.532
4F	31.788	23.978	0.236	0.175	24.571	25.807
2N	31.750	23.952	0.132	0.102	24.560	23.077
2F	31.775	23.952	0.140	0.107	24.620	23.636
Average					**24.407**	**24.261**

The SCSZ and YSZ discs were stacked in the order illustrated in Figure 15 in section 2.2.2, rotating each layer by x degrees, where x=360/n, n being the number of layers being used to produce the electrolyte. In this case, 6 layered electrolytes were chosen for single cell manufacturing due to properties of high strength and conductivity as compared to thinner structures [39]. As such, each subsequent layer was rotated 60 degrees past the rotation of the previous layer. The stacked layers of SCSZ and YSZ discs were then heated to 60°C and laminated under pressure of 25MPa using a Carver heated hydraulic press. The laminated electrolytes were then pressureless sintered between ZrO_2 coated setter plates to prevent curvature and buckling of the electrolytes which can occur during sintering due to the stresses present from the mismatch in thermal and mechanical material properties [39]. Constrained sintering of the electrolytes between these platens ensures flatness of the electrolytes after the sintering process.

4.1.3 Sintering

Sintering temperatures were determined through sintering at a range of temperatures and density measurements to calculate porosity to determine the ideal sintering temperature for the necessary density as outlined in section 3.3.3. The sintering behavior of both materials was determined in order to find a sintering temperature that would adequately densify both materials individually and thus could be used for sintering of layered structures. A fully dense electrolyte structure is desired for maximum ionic conductivity and to minimize any chance of gas crossover between the two electrodes. To determine the optimal sintering temperature, 2g samples were compressed in a 10mm cylindrical die with 20MPa of pressure and then sintered at temperatures of 900°C, 1000°C, 1100°C, 1200°C, 1300°C, 1400°C, 1500°C, 1550°C, and 1600°C. Three samples of each material were sintered at each temperature for 4 hours, with heating and cooling rates of 1°C/min. The density of the sintered samples was then calculated using Archimedes' method. A Mettler Toledo JB1603-C scale was used to weight the samples in air and water. A desiccator connected to a JB Industries DV-142N Platinum vacuum pump was used to ensure full penetration of the water into the pores to measure the density of the samples which exhibited an open porosity, specifically those sintered at 900-1100°C. Those samples were submerged in water in individual beakers and then placed in the desiccator for 5-6 hours with the vacuum pump pulling air out of the desiccator, in turn causing the air to evacuate the pores and fill them with water. The resulting density and porosity measurements with respect to sintering temperature for SCSZ and 3YSZ are as shown in Figure 48 and Figure 49, respectively.

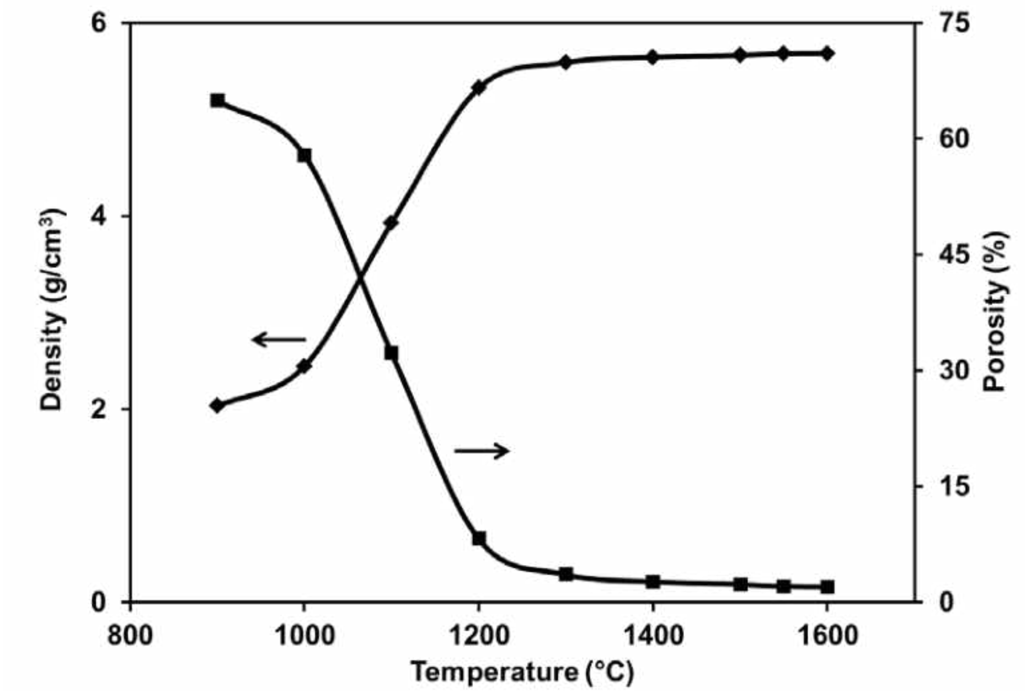

Figure 48 - Density and porosity as a function of temperature for 10 mol% Sc2O3 - 1 mol% CeO2 - ZrO2.

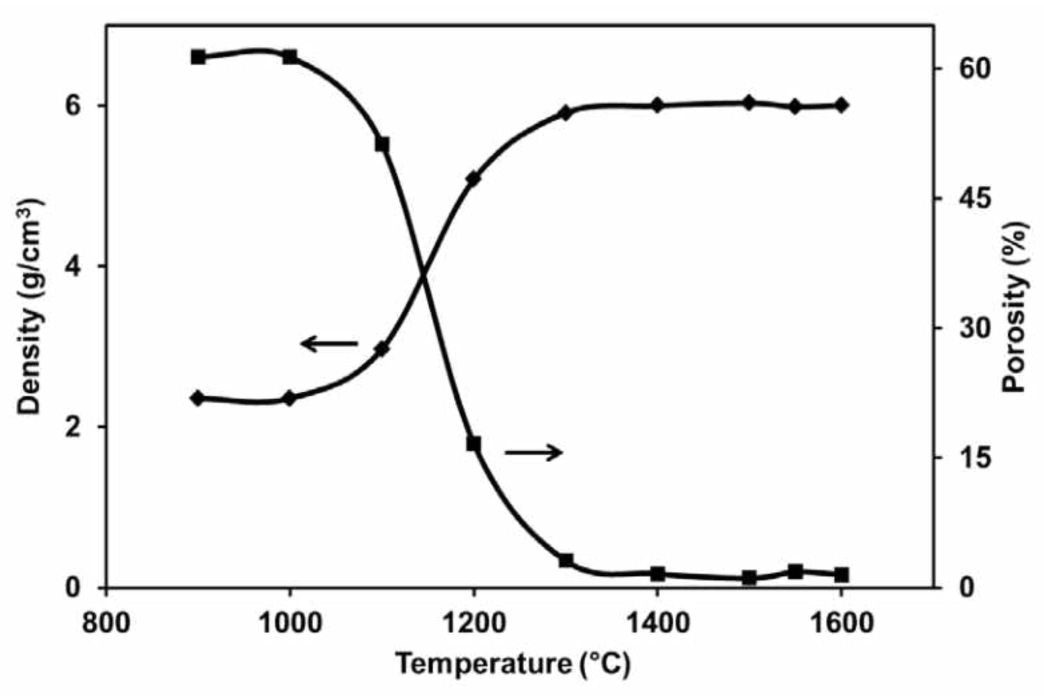

Figure 49 - Density and porosity as a function of temperature for 3 mol% Y_2O_3 - ZrO_2.

A final sintering temperature of 1500°C was selected for the layered electrolytes, as both materials individually show high density is achieved in the 1400-1500°C temperature range. The sintering routine in Figure 50 was established accordingly. The 3hr dwell periods at 300°C and 600°C are in place to ensure the complete removal of all solvents, dispersants, plasticizers, and binders in the slurry, leaving only the primary particles behind to sinter together. The slow heating and cooling rates are to prevent fracture from thermal expansion and resulting stresses.

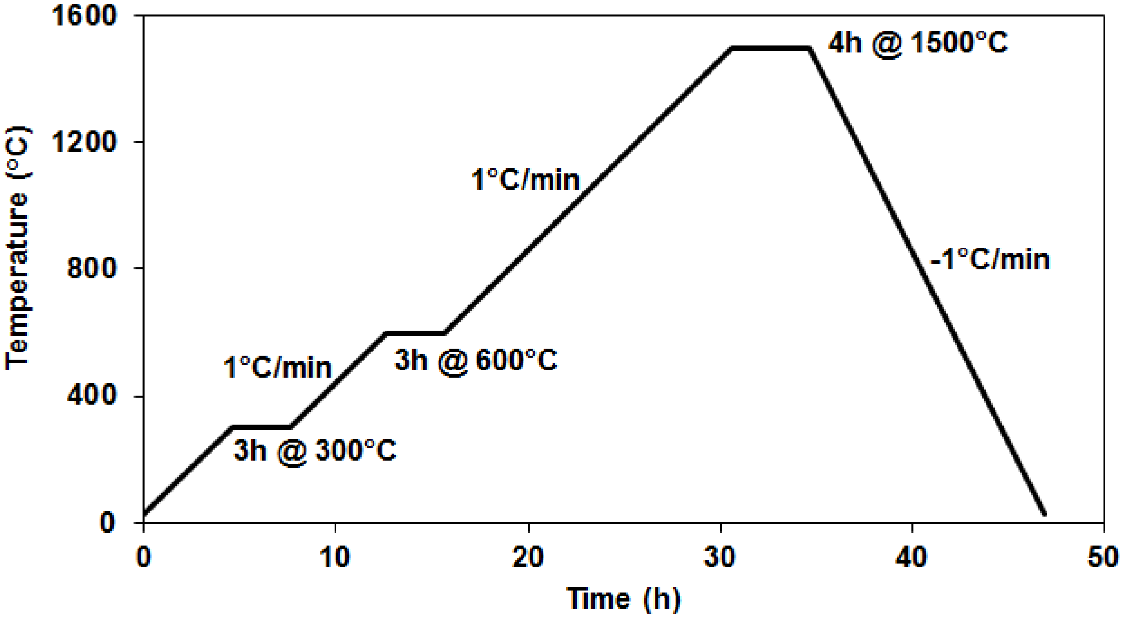

Figure 50 - Sintering profile for layered electrolytes with 3 hour hold periods at 300°C and 600°C and a sintering period at 1500°C.

4.2 Intermediate Layer

As stated in section 2.3.3, application of an intermediate layer is essential to preventing the formation of non-conductive zirconate phases between the cathode and electrolyte. It is required that the regime used for applying the intermediate layer be both controllable and repeatable, to produce likewise results. In order to meet these requirements, spin coating, as described in section 3.2.1, was used to apply a thin intermediate layer of Praxair $Ce_{0.8}Gd_{0.2}O_2$ (GDC) with a specific surface area (SSA) of 6.56 m^2/g to the electrolyte surface. Subtle variations in the spin coating parameters can result in vast differences in the coated film [20]. Therefore, it is important to establish a well-defined spin-coating regime that yields repeatable satisfactory results.

Figure 51 - Spin coating electrolytes with GDC.

In order to spin coat the GDC onto the electrolyte, a suspension of GDC in ethanol was created to disperse the GDC over the electrolyte. The suspension consists of 10 wt% GDC in ethanol, which was stirred with a glass rod to begin the dispersion of the GDC and then fully mixed by placing the beaker in an ultrasonic bath. The beaker containing the suspension was placed in the bath for 15-25 minutes until full dispersion of the GDC in the ethanol was achieved. This was verified visually by using the glass rod to scrape the bottom of the beaker to make sure none of the GDC agglomerated at the bottom of the beaker, rather than dispersing in the solution as desired. Throughout the spin coating process the suspension was placed into the ultrasonic bath periodically for a few minutes to ensure suspension of all particles, as some small amounts of GDC tend to drop out of suspension after longer periods of time. This is especially important when sequentially coating numerous samples.

Several different spin coating regimes were tested to find a suitable recipe which left a coating with the desired characteristics after sintering. The final speed was settled at 2500rpm as a starting point taken from [21], in which the authors spin-coated a thin, uniform layer of YSZ onto an anode using a similar suspension. Using this as a basis, the spin-coating regime was altered and the effects of the alteration were studied; alterations such as static vs. dynamic dispensing of the fluid onto the electrolyte and alteration of the ramp up speed vs. immediate speed up to the final spin speed of 2500rpm rather than having a ramp up to speed; these will be explained in the following paragraphs. Regardless of what spin-coating recipe was used, however, the sintering routine remained the same. After successfully spin-coating the electrolytes and placing them in a covered zirconia-coated alumina tray, the furnace was heated at 5°C per minute up to 1400°C from room temperature where it dwelled for 4 hours to sinter the GDC layer and then cooled at 5°C per minute.

The first of the spin coating routines tested was to keep the final spin speed constant at 2500rpm and alter the ramp rate by changing the time period between rest and final spin. First, the surface of the electrolyte was flooded at rest, dropping enough of the suspension onto the electrolyte to cover the entirety. Spin-up interval times of 3, 5, 10, and 15 seconds were tested using layered electrolytes with a 20mm diameter, as these were the size initially being produced for our lab by Yan Chen [39]. Of these tests, the 10 second ramp time proved to yield the best results. The 3 and 5 second ramps were too quick, providing inadequate cover of the cell's surface as the excess suspension spun off before reaching the edge of the electrolyte. The 15 second ramp proved to be unnecessarily long, which caused uneven deposition due to slow speed, with the layer being thicker towards the center of the electrolyte and gradually thinning towards the edges. Figure 52 shows the results of using a 10 second ramp up to the 2500rpm final spin speed.

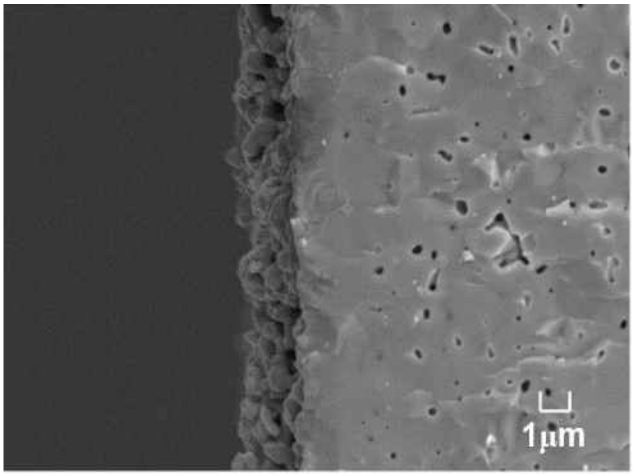

Figure 52 - Flooded surface, 10 second ramp to 2500 rpm.

The second routine tested was to flood the surface of the electrolyte and immediately speed up to the final spin speed. Starting with the 2500rpm spin speed suggested in [52], several speeds were tested. The 2500rpm spin appeared to be too fast, as the coating left behind was thick and very uneven, as seen in Figure 53, suggesting inadequate time or too fast of a spin for adequate adhesion to occur. Based off of this observation, slower speeds of 2000rpm and 1500rpm were also tested. The slower speeds, however, did not show an improvement in coating quality, leaving behind the same uneven coating that the 2500pm samples displayed.

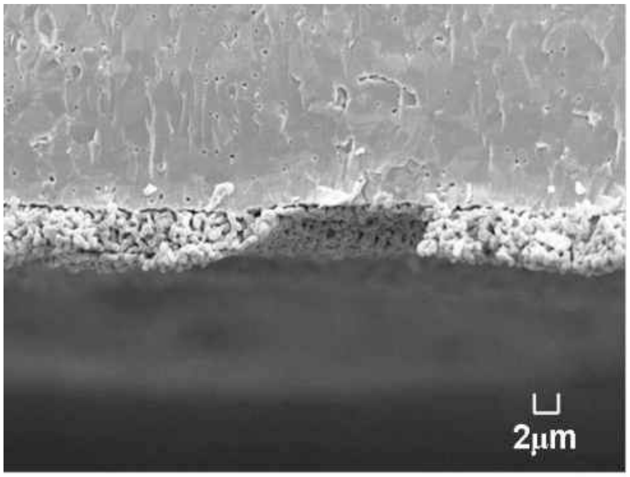

Figure 53 - Flooded surface, immediate spin up to 2500rpm.

The third approach which was tested was to dynamically drop the solution onto the surface of the electrolyte as it spun. For these tests, the samples was placed onto the spin coater and spun dry, dropping solution steadily onto the surface through an access hole in the lid of the spin coater made specifically for this reason. This was tested at speeds of 2500rpm, 2000rpm, and 1500rpm. Regardless of the speed, however, this method proved unreliable. Figure 54 shows the uneven coating left by using this method, which left some portions complete uncoated even after several layers of application. It is believed that this method is of too low a viscosity to use this method, since regardless of the speed tested the resulting coating was thin and very uneven. This method may have worked at much lower speeds than tested, but it is also very wasteful. Therefore, testing of this routine at lower speeds was not done, as the amount of material wasted using this routine was much higher than with the other routines tested.

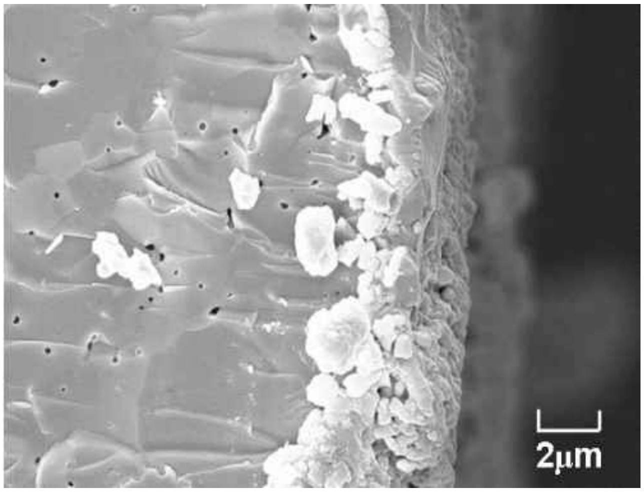

Figure 54 - Drip suspension onto electrolyte while spinning at 2500rpm.

The first routine was chosen for use with 20mm electrolytes. The recipe used is as follows: flood surface of electrolyte with this layer of GDC suspension, 10 second interval duration spin up to 2500 rpm, dwell for 50 seconds at 2500rpm, slow down to 0rpm using 5 second interval. This was repeated 10 times to ensure a homogeneous thin coating would be left behind after sintering. The ramp period is the period during which all excess suspension is spun off, leaving behind the thin coating desired, and the dwell period serves to dry the spin coated surface so that the next layer may be applied. Spinning at a continuous speed serves to pull air onto the surface of the sample to evaporate the solvents, causing it to dry thoroughly and leave behind a film of solids. The slow-down period was chosen arbitrarily as it serves only to lighten wear on the machine, as the manual states that abrupt stops from high speed spins are detrimental to the life on the unit. After the 10 coats are applied, the GDC coating was sintered at 1400°C for 4 hours with heating and cooling rates of 5°C/min [121].

Due to the need for 25mm diameter electrolytes for performance testing of single cells in the National Energy Technology Laboratory (NETL) test stands, alterations had to be made to the spin coating routine as the larger diameter changed the results of the coating using the aforementioned routine. The larger sized electrolytes did not get homogeneously coated throughout the entirety of their diameter, as seen in Figure 55. The reflective, lighter colored portion of the electrolyte, which can be seen encircling the entire sample between the outer edge and the center of the electrolyte, is the resulting uncoated portion of the electrolyte after sintering.

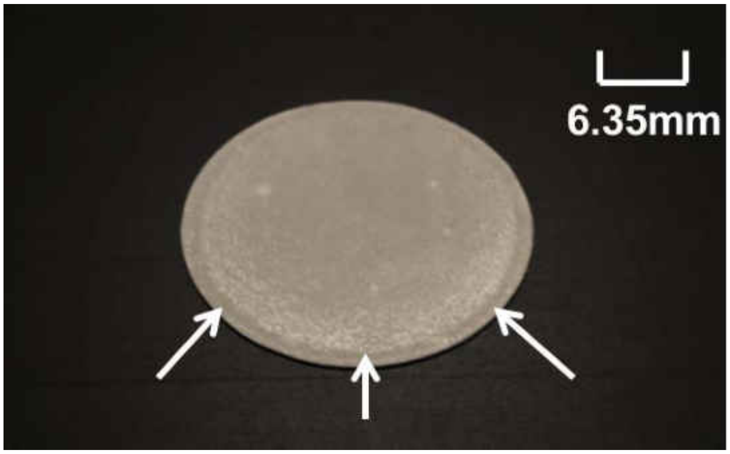

Figure 55 - Non-homogeneously coated 25mm electrolyte coated with previously established routine.

The first attempt to fix this involved adding more layers to the coating, in the belief that each new coat extend closer to the edge of the electrolyte, however this was not the case, and after 20 coats there was still a small ring of uncoated or very lightly coated electrolyte surface present. Next, the previously established routine was done twice on the same cell; the cell would be coated with 10 layers using a 10 second ramp to 2500rpm and sintered at 1400°C and then coated with another 10 layers and sintered again. This had the desired effect of producing a more-or-less homogeneous coating throughout the entire diameter of the electrolyte surface. Thus, this double-coat method was established as the method to be used for coating future cells. In the interest of expediting the production of complete single cells for testing at the NETL, this method was established and alterations to it were left unexplored. It is, however, believed that this method could be further refined and the issues of incompletely coated 25mm electrolytes could be solved with a more efficient routine. Suggestions on alternate routines to explore are included in Chapter 5: Future Work.

Table 15 - GDC coating routine and spin coater recipe.

Step	Description	Time	Speed/Rate
0	Initialize recipe	0 sec.	0 rpm
1	Ramp	10 sec.	2500 rpm
2	Dwell	50 sec.	2500 rpm
3	Ramp	5 sec.	0 rpm
4	End recipe	0 sec.	0 rpm
5	Repeat 10 times.		
6	Sinter at 1400°C for 4 hours, 5°C/min. ramp.		
7	Repeat coating 10 more times.		
8	Sinter again.		

During the aforementioned time spent at the NETL for testing, complete cells were manufactured using materials on site. This brought to attention the need for consistency in material use. The GDC powder in stock at the NETL had a specific surface area (SSA) of $9.47m^2/g$, as opposed to the $6.56m^2/g$ powder used at the home institution. The use of this powder with the previously established routine proved for very different results, as the dynamics of the smaller powder changed the coating quality. Figure 56 shows the drastic differences between the two; the use of the higher SSA powder resulted in a thicker, less homogenous coating due to the smaller powder dropping from suspension faster than the larger one. The severity of the non-homogeneity became more pronounced with the addition of more layers, causing uncoated valley-like features to be very pronounced in the resulting coating.

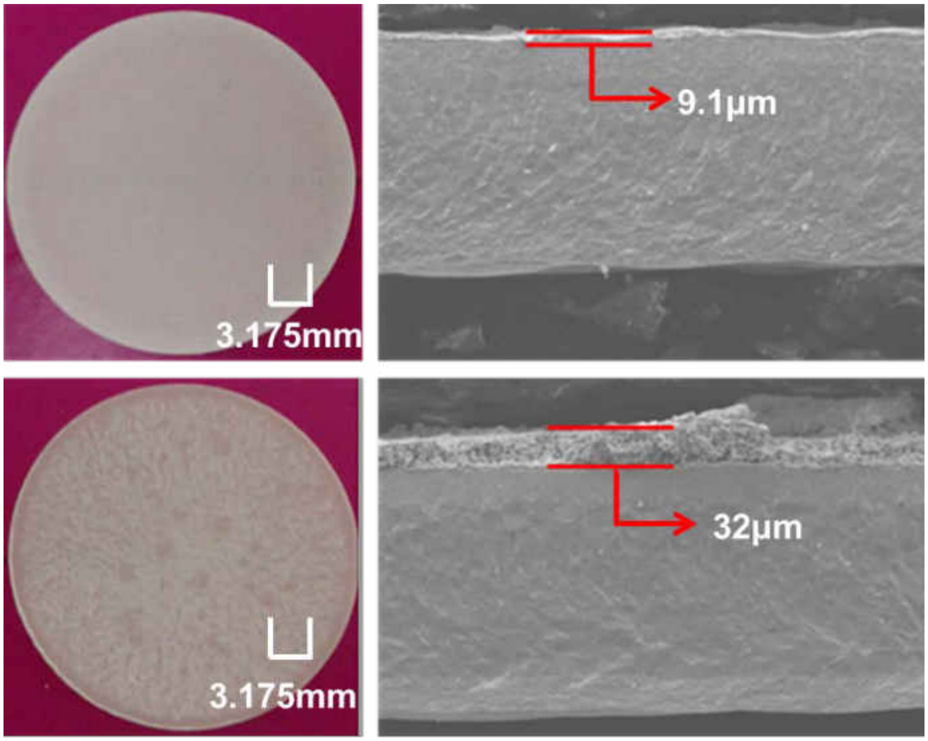

Figure 56 - Comparison of resulting coatings when using the same routine for powders with different SSA values; 6.56 m^2/g shown on top, 9.47 m^2/g on bottom.

4.3 Ink Preparation

As discussed in section 3.2.2, electrode inks are made to be used with screen printing to apply electrodes to the electrolyte support. These inks are made from a combination of electrode powders, 65 wt% NiO – 35 wt% 8 mol% YSZ for the anode and $(La_{0.6}Sr_{0.4})_{0.995}Fe_{0.8}Co_{0.2}O_{3-\delta}$ for the cathode, and terpineol. To ensure adequate porosity of sintered electrodes, a pore former was used in fabricating both the anode and cathode inks. A pore former powder is blended with the electrode powder in a 60vol% electrode powder - 40vol% pore former mix to be used for making the inks to be used in the electrode manufacturing process. This is done to ensure that a well-connected pore matrix exists within the electrodes after sintering of the printed electrodes. This both extends the triple phase boundaries and eases the diffusion of gases from the flow channel to the electrode-electrolyte interface. A study was conducted in order to choose the best pore former from a few likely candidates. Three candidate materials were identified as potential pore formers from [122]; Cabot Vulcan XC72R carbon black (CB) which has a density of 0.0961 g/cm^3 and a light, flaky texture, Acros Organics polymethyl methacrylate (PMMA) with a density of 1.18 g/cm^3 and a hard, granular texture, and polyethylene (PE) from Polysciences, Inc. with a density of 0.915 g/cm^3 and 3-45μm spherical particles.

As stated, the purpose of the pore former is to create a network of continuously interconnected pores spread uniformly throughout the electrodes. To test the pore structures formed by these different materials, a number of small cylindrical samples were made for each material from a mixture of 60vol% (65wt%NiO-YSZ) and 40vol% pore former. The powders were thoroughly mixed using a ball mill, zirconia milling media, and ethanol, then dried slowly so as to not separate the mixture and sieved to eliminate agglomerates and ensure proper mixture. The powder was then used to press several 2g cylindrical pellets using a 10mm die and hydraulic press. These pellets were then sintered at 950°C to 1150°C. Higher density (1100°C and 1150°C) samples were subsequently fractured and for inspection of inner pore matrix using a SEM.

The first of the pore former materials to be tested was the PE. As seen in Figure 57, the polyethylene-containing samples did not actually sinter into a porous structure. Instead, the PE caused the NiO to reduce to Ni. This is due to the fact that polyethylene thermally degrades at high temperatures. Polyethylene is a polymer chain of ethylene, C_2H_4. At temperatures above 780°C the polyethylene chains break down into several different gaseous hydrocarbon constituents such as H_2, CO, CO_2, CH_4 C_2H_6, and C_2H_4 [123]. These gaseous species then act as a fuel for the reduction reaction of NiO to Ni, as shown in Equation 10 [124].

$$6NiO + C_2H_4 \rightarrow 6Ni + 2H_2O + 2CO_2 \tag{10}$$

As such, polyethylene was immediately dismissed as a choice for use as a pore former for the electrodes.

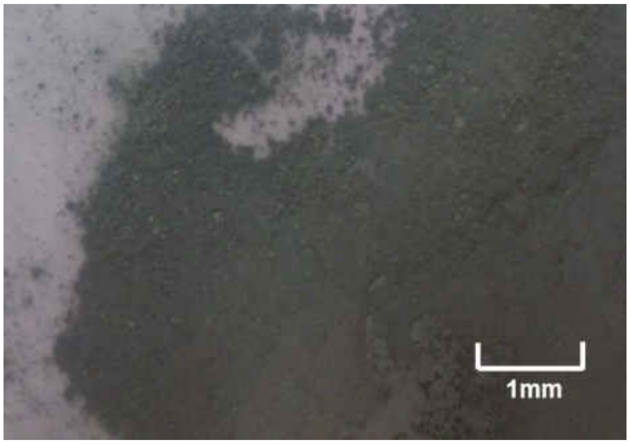

Figure 57 - Anode sample sintered with polyethylene which caused reduction of NiO to Ni during sintering.

Next, PMMA was tested using the same process. The PMMA powder before processing has a hard, granular consistency, like very small beads. The resulting porous structure after sintering of the pressed samples reflects this. Figure 58 shows the large, crater-like pores which resulted from the use of PMMA in the anode samples and which could be seen with the naked eye without the assistance of a microscope.

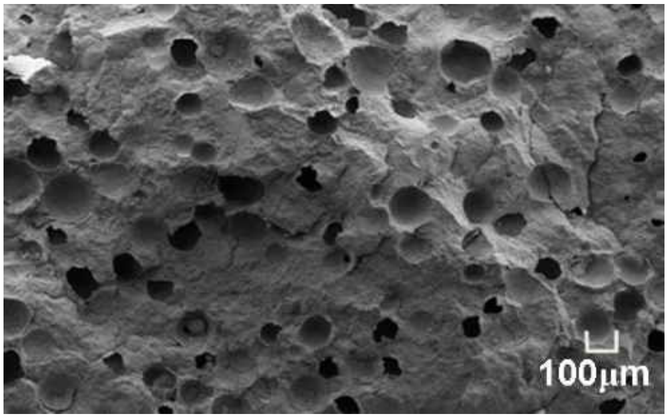

Figure 58 - Large, isolated pores caused by using PMMA as a pore former.

These pores are largely unconnected, and caused the surrounding areas to be quite dense in comparison to areas further from the edges of these large pores, as seen in Figure 59. This suggests an effectively low overall porosity for the sample. As such, PMMA was also deemed a poor choice for use as a pore former.

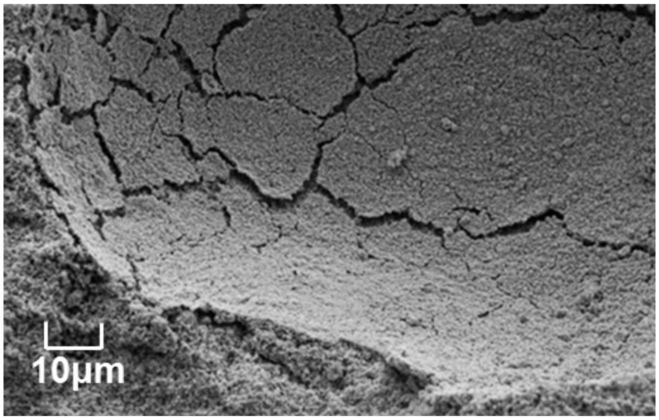

Figure 59 - Dense surfaces of large pores causing poor connectivity of pore matrix.

The final pore former additive tested was the carbon black. The carbon black, with its very low density, had a very flaky, light texture, which made it somewhat difficult to work with and very messy. Special care and attention was needed when mixing the CB with the electrode powder during the drying stage, as the very light powder can separate from the mixture easily if left untended for too long. However, it proved to be very effective in achieving the desired results, as shown in Figure 60. The samples prepared with CB as a pore former had a very desirable homogeneous pore structure throughout. As such, it was determined that CB produced the ideal pore structure for electrodes to provide a highly connected pore matrix for the purposes of gas diffusion and extension of the TPB.

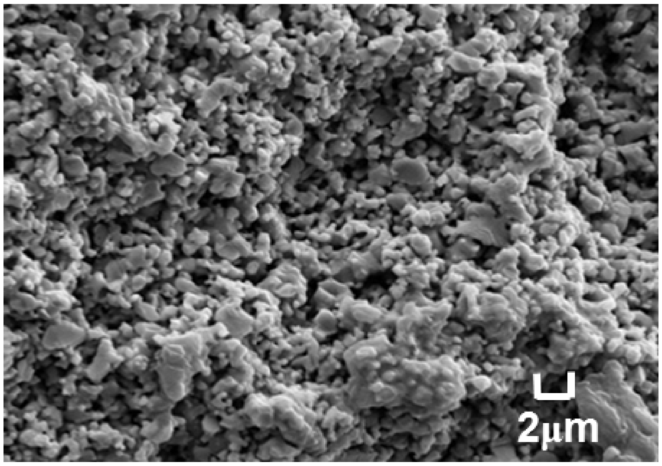

Figure 60 - Use of carbon black yields the ideal homogeneous pore structure sought for electrodes.

Inks are then created by blending a mixture of 50wt% powder mixture with 50wt% terpineol as a delivery vehicle which is burned out during sintering using a Keith Machinery 3-roll mill. The powder mixture is as described previously, consisting of 60vol% electrode powder (LSCF for the cathode and 65wt%NiO-3YSZ for the anode) and 40vol% carbon black pore former. The first attempt at creating inks for printing utilized α-Terpineol from Acros Organics, which has a measured viscosity of 43.2cp using a number 27 spindle at 50 rpm. For reference, water has a viscosity of about 1cp at room temperature. The terpineol was added to the 3-roll mill first, between the middle and rear rollers, creating a smooth roll of terpineol between the two rollers. The powder is slowly added to this roll little by little, making sure each addition is smoothly blended in before adding more. This produces a homogeneously smooth ink and prevents the creation of agglomerates in the finished ink or during the milling process. If these agglomerates are formed by adding too much powder at once, they will be forced through the rolls, causing them to be crushed. This could cause a both a loss in material and alteration of particle size distribution, which may affect printing.

The 1:1 powder to Acros α-Terpineol ratio produced a thin, low viscosity ink, much like the ink used in pens. This ink, however, proved to be ineffective for screen printing of electrodes, as seen in Figure 61. The prints produced using this ink turned out very sloppy regardless of how careful and precise one may try to be. This makes it difficult to accurately layer prints to achieve the desired thickness, as the thin inks would smear onto the surface rather than being deposited in a precise layer.

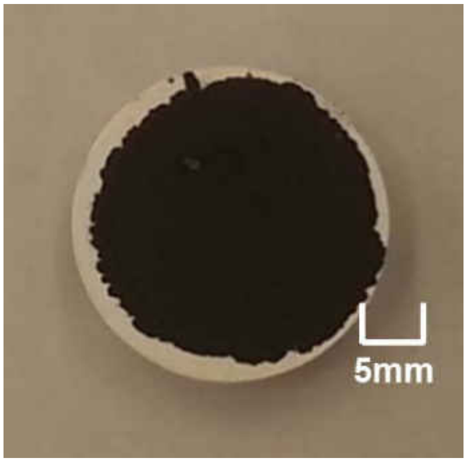

Figure 61 - Attempted layered cathode printed using ink made from 1:1 α-Terpineol to powder mixture.

In order to fix this issue, V-006A terpineol with resin was purchased from Heraeus Electronic Materials as a starting point to formulate a new, thicker mixture. The Heraeus V-006A has a measured viscosity of 5020cp using a number 6 spindle at 50 rpm. Starting with a 1:1

terpineol to powder ratio, the powder content would be increased or decreased until a usable ink was produced. However, the resin mixed into the V-006A made the terpineol much thicker to begin with than the previously used Acros Organics α-Terpineol. As such, the V006 acts as both a dispersant vehicle and a binder. It was mixed in the same manner, but the thicker terpineol produced less wasted material due to its viscous properties, eliminating drips from the rolls and minimizing the amount of ink which was lost to the mill after scraping the ink off of the front roll. Using the HV006 in a 1:1 mixture produced an ink with a paste-like consistency. This material was easy to work with and produced very sharp, accurate prints when applied to the electrolytes via screen printing. Although it required numerous prints due to its high viscosity, the sharp definition of the prints allowed for easy alignment for subsequent prints to achieve accurately layered electrodes.

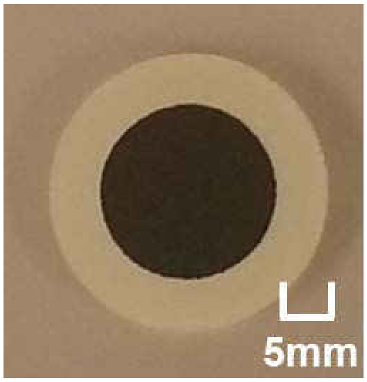

Figure 62 - Layered cathode printed using ink made from 1:1 Heraeus V-006A to powder mixture.

Furthermore, the V006 helps to keep the particles in the suspension much better than the α-Terpineol due to its high viscosity and resin content. Inks produced with the α-Terpineol undergo separation of phases after aging for a short time, as little as a week can be enough time for the powder to separate from the terpineol vehicle. The inks made with the V006, however, kept the same consistency a few weeks after initial production.

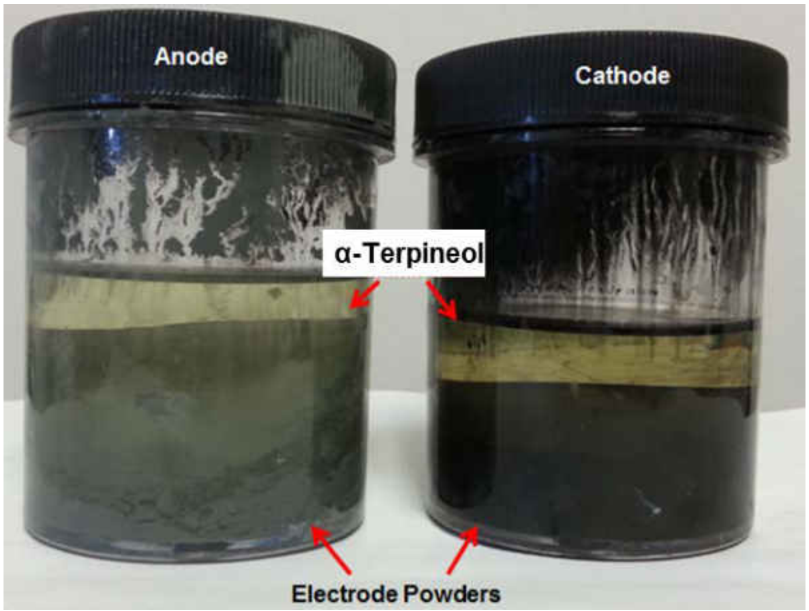

Figure 63 - Inks made with α-Terpineol which show separation of phases after short periods of storage.

4.4 Electrode Processing

4.4.1 Screen Printing

As described, application of the electrodes is performed by screen printing and drying several layers of ink onto each electrolyte. However, the number of prints necessary for each electrode will differ due to the increasing overall thickness of the cell and thus decreasing space available between the cells surface and the screen. Each time a new layer is applied the free space for which a new layer may be applied is marginally reduced. This difference can be seen in

Figure 64 and Figure 65, which have had 3 and 4 layers, respectively, of anode ink applied, dried, and sintered.

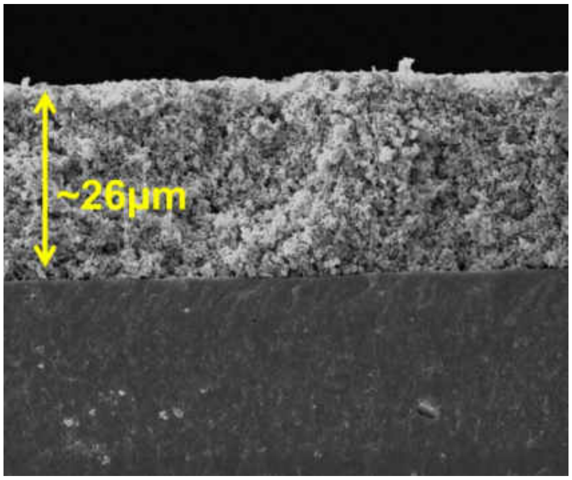

Figure 64 - Electrolyte with 3 layers of anode ink printed.

Figure 64 shows a cell with 3 layers of anode ink printed and sintered on, which resulted in a thickness of about 26μm. This averages out to 8.67μm per print. However, as Figure 65 shows, this is not necessarily the case. The electrolyte printed with 4 layers results in a 32μm thick electrode, averaging 8μm per print.

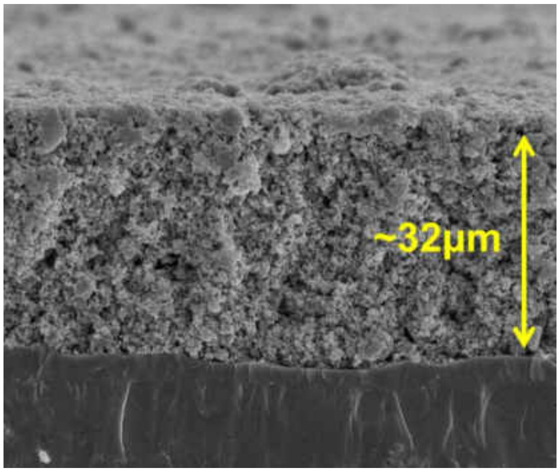

Figure 65 - Electrolyte with 4 layers of anode ink printed.

Thus, each new layer does not necessarily add the same amount of thickness to the cell, and these effects become more pronounced as layering continues. This is especially relevant when applying the second electrode, as the space between the electrolyte surface and the screen printer will be reduced by however large the final thickness of the electrode may be. Several cells were printed with varying numbers of layers to achieve a thickness of ~30µm per electrode. Testing was done to determine the thickness of the first electrode, the anode, by printing GDC coated electrolytes with 3, 4, 5, and 6 layers of ink. These were then inspected using a SEM to determine how many layers were necessary to achieve the desired thickness. After this number was determined, several cells were manufactured with the anode and the same test was repeated for finding the cathode thickness. It was determined that 4 layers would provide the desired thickness for the anode and 5 layers for the cathode.

4.4.2 Drying

The screen printing process to apply electrodes to electrolytes requires layering of multiple prints. In order to prevent smearing of inks and to achieve proper thickness through layering, each layer must be dried after its application to create a new dry surface for the subsequent layer to be applied to. It is, of course, of high interest to find the most expedient way to do this. Time is money, and so the concerns of lowering production costs directly apply to the time spent on any one process required to fabricate a single cell. With that in mind, it is essential that this process not be rushed, as inadequate drying time can lead to undesirable results. As such, the first routine established to dry each layer applied involved drying at 400°C for one hour. Although this routine is effective at ensuring an adequate level of dryness for each layer so as not to affect the final microstructure, as seen in Figure 66, it also presents some problems. Due to the temperature, the furnace must be given time both to heat and cool steadily, so as not to incur problems from thermal shock. This can occur when removing the samples from the 400°C furnace to the room temperature environment, causing additional stresses which could cause the cell to fracture.

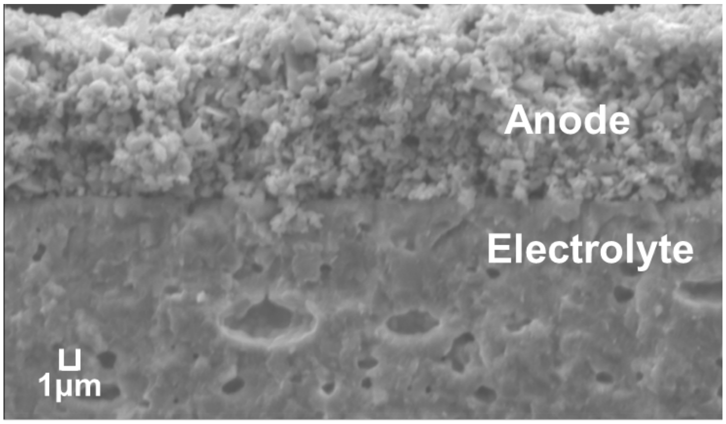

Figure 66 - Microstructure of layered screen-printed electrode dried at 400°C for 1h.

In order to remedy the issue of using such a time consuming recipe for drying –around 30 minutes for heating and the same or more for cooling to a safe level – a recipe was established at the lower level of what might work. At a suggestion from the NETL, the next recipe attempted was to dry each layer at 100°C for 30 minutes. This would eliminate the need for long heating and cooling times, saving hours over the previous process. This routine, however, did not provide adequate drying and, as seen in Figure 67, the application of subsequent prints affected the microstructure or the lower layers, trapping moisture within the lower layers until sintering and causing large agglomerations to form. It is suspected that the pressure from each subsequent print caused a pressing effect on the previous layers and the remaining terpineol acted as a sort of lubricant between particles, encouraging the formation of these agglomerates. These agglomerates can cause blocked pore passages to form, impeding gas flow through the electrode and lowering cell performance.

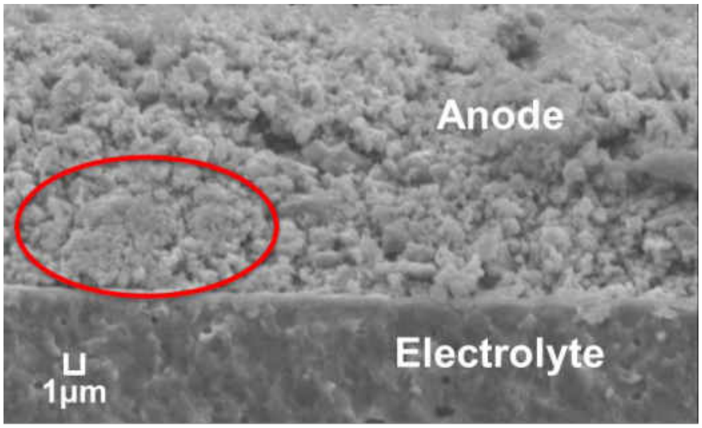

Figure 67 - Microstructure of layered screen-printed electrode dried at 100°C for 30min, note agglomerates caused by imporper drying.

Raising the duration of drying to 1 hour at the same 100°C temperature yielded slight improvements, but the clumping was still an issue. Keeping the time period constant at 1h, as the duration of the drying period seemed to be of high importance, the temperature was raised to 200°C to ensure thorough drying. This temperature for 1h proved adequate for drying the layers thoroughly without compromising microstructure, preventing the agglomeration of particles while eliminating the need for extensive heating and cooling periods.

4.4.3 Sintering

After printing, electrodes need to be sintered. In order to determine the sintering temperature, the same process was used that was used to determine the electrolyte sintering temperature. However, the desired characteristics are different. For the electrodes, a porosity of around 40% is desired to avoid mass transport issues with fuel and oxidant delivery. This means finding a temperature which results in a well-connected pore matrix intertwined with a highly sintered electrode matrix with strong connections between particles. For electrodes, 2g samples of 60 vol% electrode powder – 40 vol% carbon black mixture were pressed in a 10mm die and sintered at 900, 1000, 1100, 1200, 1300, 1400, 1500, 1550, and 1600°C for 4 hours with heating and cooling rates of 2°C/min.

The Archimedes method was used to calculate the densities and porosities at each of the different temperatures using a theoretical density of 6.34 g/cm^3 for the anode mixture and 6.448 g/cm^3 for the LSCF cathode. The anode and cathode sintering curves are shown in Figure 68 and Figure 69, respectively.

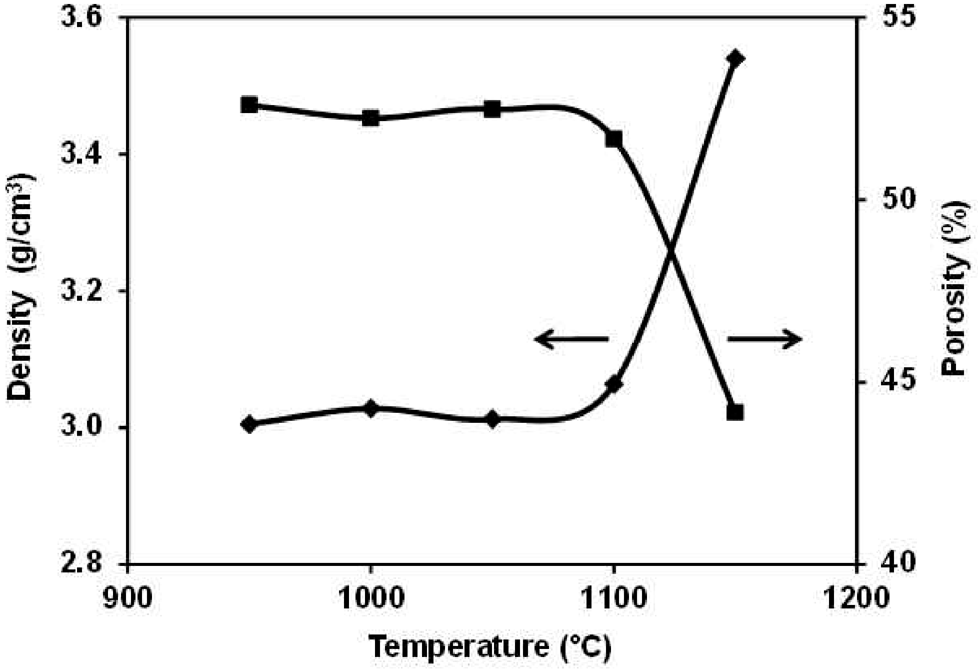

Figure 68 – NiO-YSZ anode sintering behavior.

From Figure 68 the anode sintering temperature was chosen as 1150°C, as it still has a high level of porosity but also shows some densification.

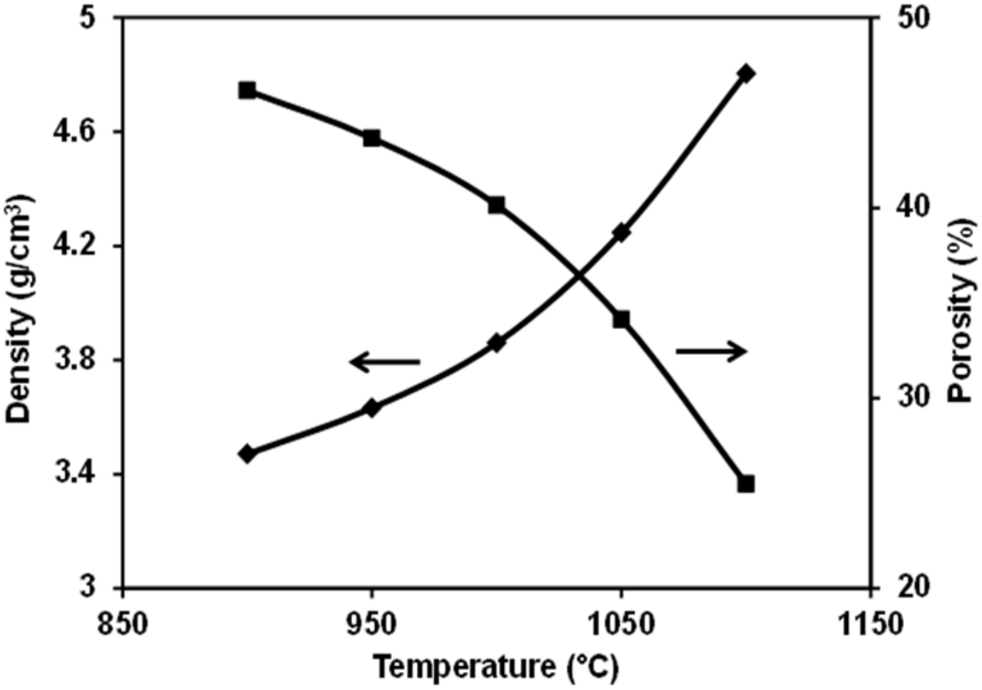

Figure 69 – LSCF cathode sintering behavior.

Similarly, the cathode sintering temperature was chosen as 1000°C using the relationship shown in Figure 69. As such, since the sintering temperature for the anode is higher than that of the anode, then the anode must be applied to the electrolyte and sintered before the cathode is applied. This is to prevent further densification of the cathode which would lead to a drastic reduction in porosity. As seen in Figure 69, if the cathode were to be applied first and then the anode applied and sintered at 1150°C, the cathode would continue to sinter, reducing the porosity to below 20% which would enormously impede gas flow through the electrode.

4.5 Single Cell Performance

All tests were performed at an operating temperature of 800°C with hydrogen humidified at 3% as the fuel and atmospheric air as the oxidant. For the 20h tests, cells were tested under constant voltage conditions to note the effects of extended use on performance and resistance.

The first of the cells tested were cells constructed using 6-layer electrolytes with 8 mol% YSZ outer layers and SCSZ inner layers. Though most of these cells failed during manufacturing as described previously, some did survive to be tested. Three cells were placed into the MCA for simultaneous testing. All of these however, failed at some point during operation, whether during cell mounting and assembly or during initial operation, yielding no performance analysis. Once again, this indicates that the 8YSZ outer layered design is not strong enough to merit further investigation. This reinforced the need to test the 3YSZ outer layered cells instead.

In light of the failure of the 8YSZ cells and in the interest of making the best of the time available for use of the NETL facilities, single cells were constructed using ceria-based Hionic electrolytes from Fuel Cell Materials. This was done so as to evaluate the performance of the electrodes themselves based on an electrolyte which the NETL team had plenty of previous experience using while waiting for 3YSZ cells to be manufactured and tested. Figure 70 shows the current response as the voltage applied was varied.

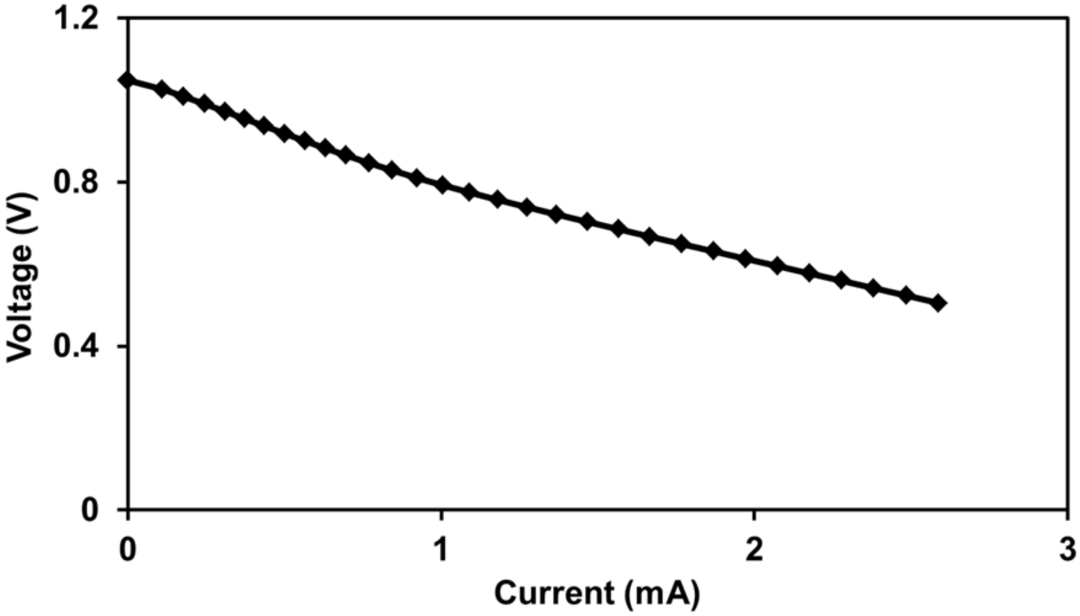

Figure 70 - Current response to varied voltage across Hionic-based single cell.

This cell showed significant ohmic resistance, as can be seen by the very low current response. Impedance testing was used to examine the specific cell losses, as described in the Experimental section. Figure 71 shows the results of the impedance test of the Hionic cell. These results show that there are significant losses in the low frequency processes, which may mean that gas diffusion is being inhibited, though many interpretations may be possible. This suggests the need to examine electrodes and further refine the mixtures and processes used to make them, to ensure a good microstructure with high porosity is being produced, though it does show that the electrodes work.

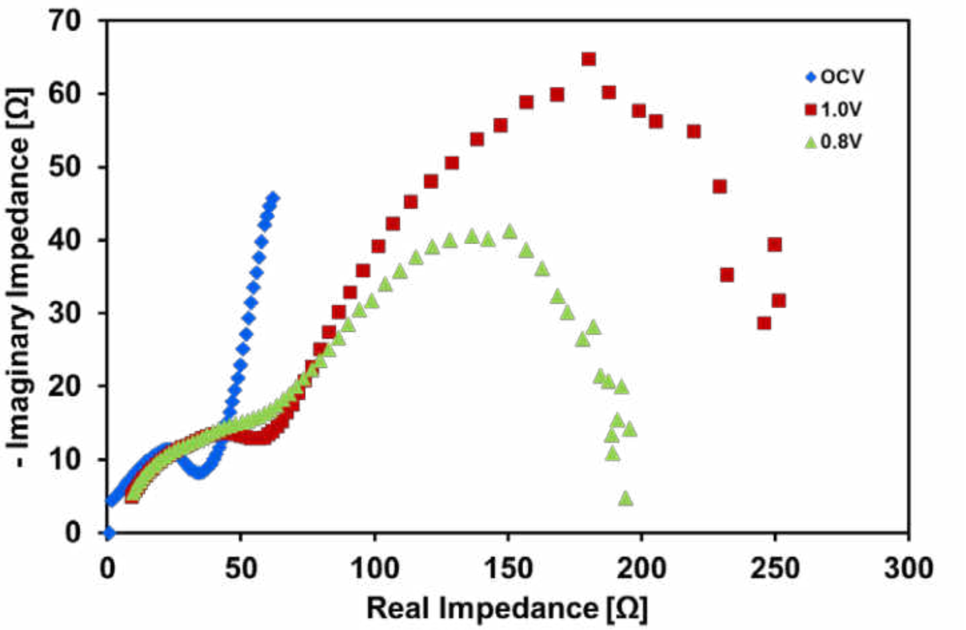

Figure 71 - Impedance spectroscopy results for Hionic-based single cell.

Production of single cells continued using 6 layer electrolytes with 3 mol% YSZ for the outside layers. As stated previously, these cells fared much better during fabrication of the electrodes. Electrolytes lost during electrode production were much lower, and cells were able to be tested without experiencing complete failure. In fact, upon removal of the cell from the test stand, initial visual inspection shows no signs of cracks and a fully reduced anode with no re-oxidation occurring. The V-I response of the 3YSZ cell is shown in Figure 72. Although the current output was roughly doubled compared to that of the Hionic cell, the overall performance is still rated as rather poor. Given that the electrodes used on these cells were identical, the increase in performance, however small, can therefore be attributed to the use of the layered electrolyte.

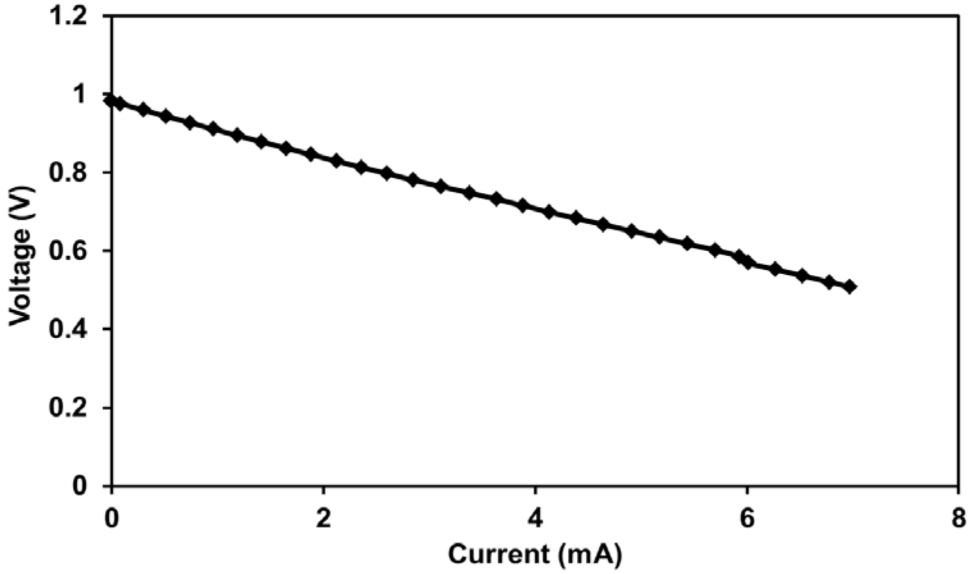

Figure 72 - V-I response of 3YSZ cell.

A standardized way to assess the cell's performance is to calculate the current and power densities of the cell. The power and current densities of the cell as a response to a varying voltage are shown in Figure 73. In order to perform these calculations from the VI response Figure 72, the electrode area was approximated at around 2 cm^2. The curve shown here is significantly lower than what may have been hoped for, but also indicates some level of success. This response indicates that the components chosen for cell production will work together, but will require further refinement.

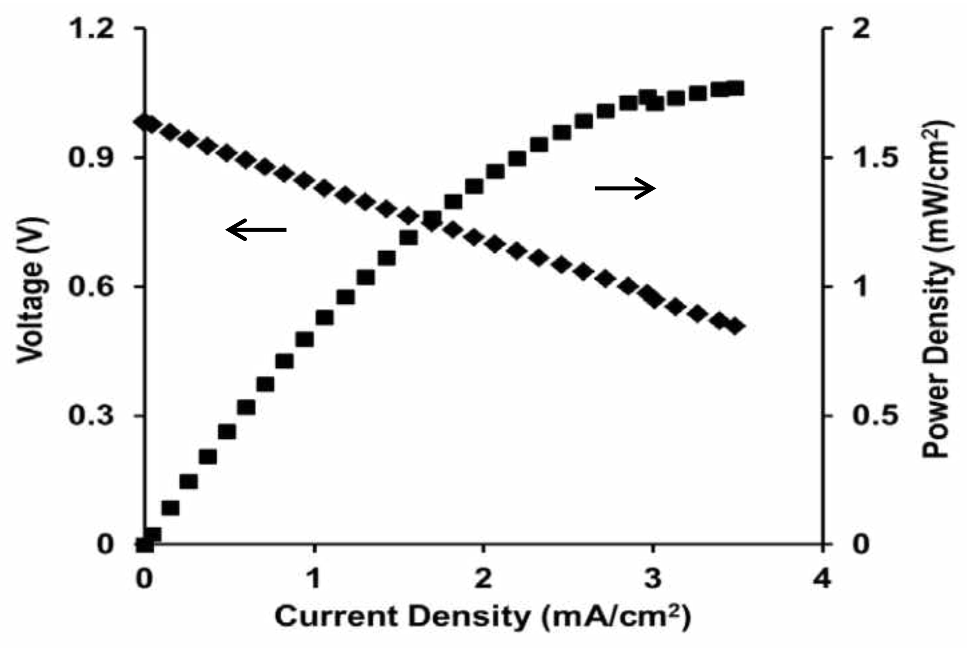

Figure 73 - Power and current densities of 3YSZ cell.

Impedance testing was performed on the 3YSZ cell during both initial operation of the cell and after 20h of operation under a constant voltage of 0.8V at 800°C. Tests were performed at both open circuit voltage (OCV) where no load is applied and with an applied load. The original impedance is shown in Figure 74 and the impedance after 20h of testing is shown in Figure 75. Direct comparison of the two plots shows an increase in all tests, in both real and imaginary impedance, the rightward shift being evident of increasing ohmic resistance after the 20h operation due to some degradation mechanism. The split in the curve for the 0.9V measurement after 20h of operation suggests partial loss of electrical contact or delamination occurring during the time the actual test was being performed. This suggests that the original rightward shift may also be due to some loss of contact or delamination which occurred between tests during the 20h operation period.

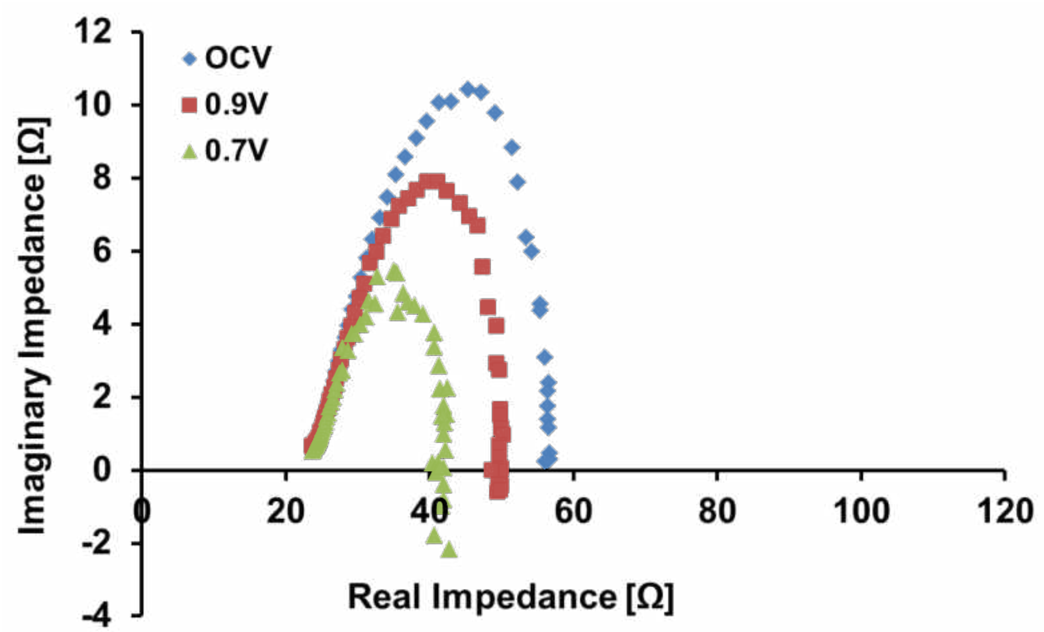

Figure 74 - Initial impedance of 3YSZ cell.

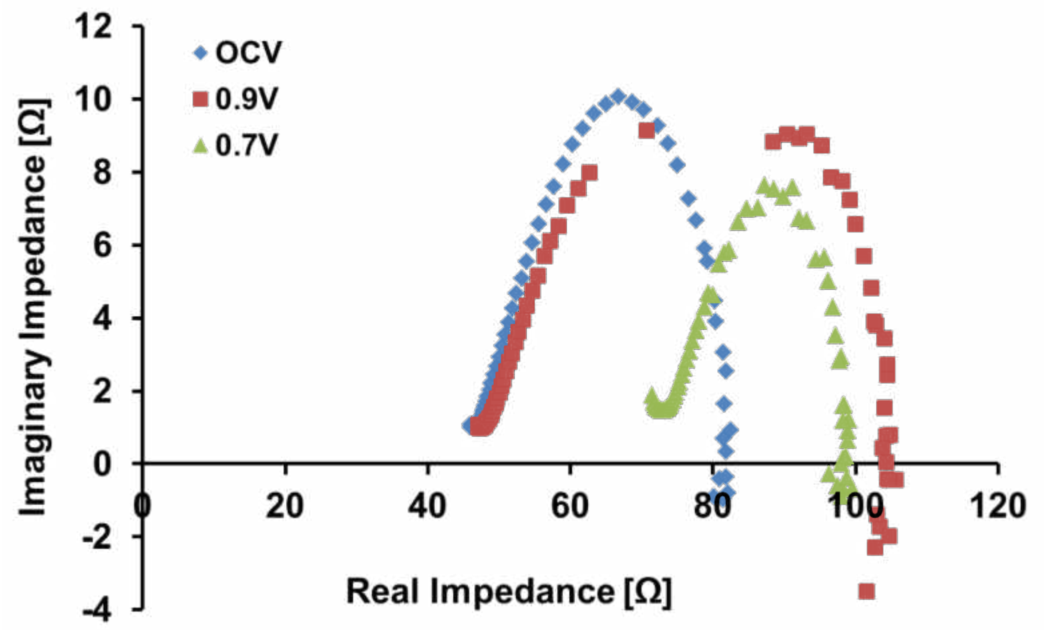

Figure 75 - Impedance after 20h testing period.

As with the power output, the impedance can also be standardized by the area, using an approximate area of $2cm^2$ for the electrode area, both at OCV and under a 0.7V load. Figure 76 shows the impedance of the 3YSZ cell at OCV conditions upon initial startup and after 20h operation. Figure 76 (a) shows the imaginary vs. real impedance with relation to area, while part (b) shows the impedance as it relates to the frequency of the applied signal, known as a Bode plot. Figure 77 shows this same cell under a load of 0.7V.

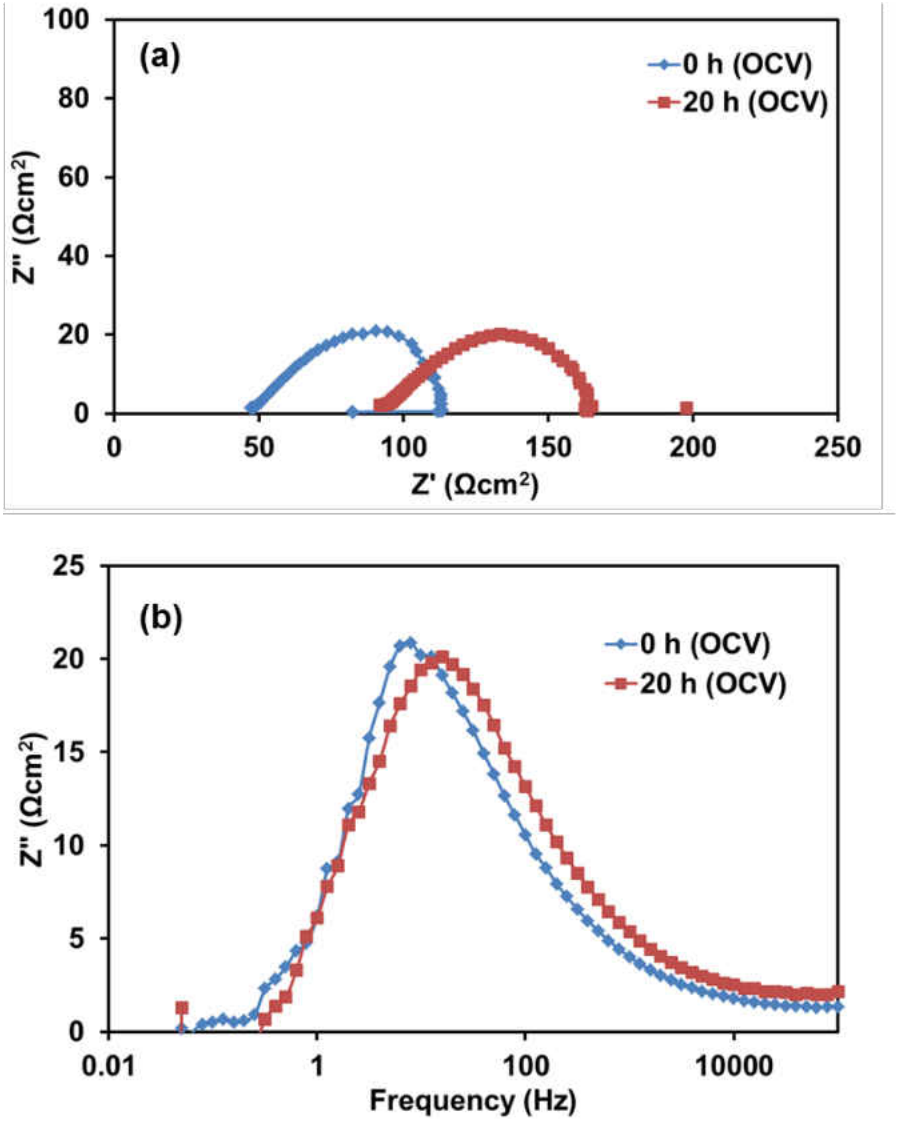

Figure 76 - Impedance response of 3YSZ cell at OCV.

There can be seen a general shift of the impedance curve, indicating a 50Ωcm^2 increase in ohmic resistance at OCV after the 20h operation. Figure 76 (b) shows a peak in the low to intermediate frequency range which is typically indicative of gas diffusion through the electrode pores for the 1-10Hz range and the dissociation and adsorption of oxygen into the cathode surface for the 10-100Hz region [97, 125-127]. The impedance shift is even more pronounced under the 0.7V load, with an increase of roughly 100Ωcm^2 after the 20h operation, as shown in Figure 77 (a).

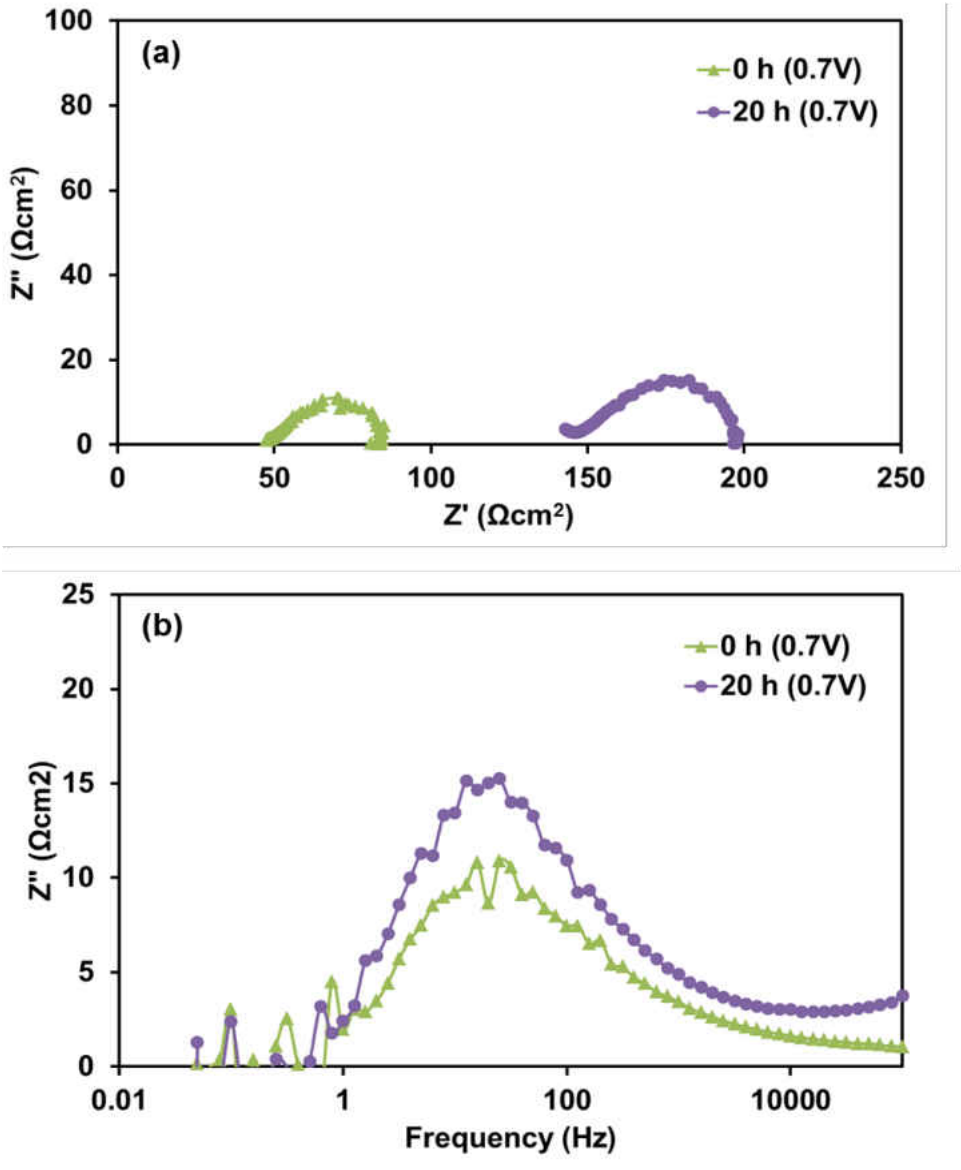

Figure 77 - Impedance response of 3YSZ under 0.7V load.

The peak in resistance in Figure 77 (b) shifts rightward to reside fully within the 10-100Hz region which is believed to be associated with cathode activation [125-127]. This leads to the belief then that the highest contribution to resistance is associated with the cathode, though the gradual rise to that peak through the 1-10Hz region suggests some gas diffusions issues through the pore structure could also be at fault. The rise in that peak after the 20h operation, therefore, is likely associated with degradation mechanisms within the cathode. The small increase in the high frequency range suggests some degradation of the performance of charge transfer at either electrode/electrolyte interface, such as a reduction of the contact region between the two components by delamination [125, 126].

4.6 Microstructural Analysis

A SEM was used to further analyze operation effects on cell microstructure to explain impedance shifts. Microscopic analysis of the cell after operation shows evidence of massive delamination occurring throughout, contributing to the shifts in the impedance analysis. The micrograph in Figure 78 shows a large crack in a section of the cell where the cathode has mostly delaminated from the electrolyte. This suggests weak bonding of the electrode to the electrolyte, perhaps due to low grain growth from an inadequate sintering period. This relates both of the increases in impedance in Figure 75 and Figure 77, as cathode performance is degrading due to delamination.

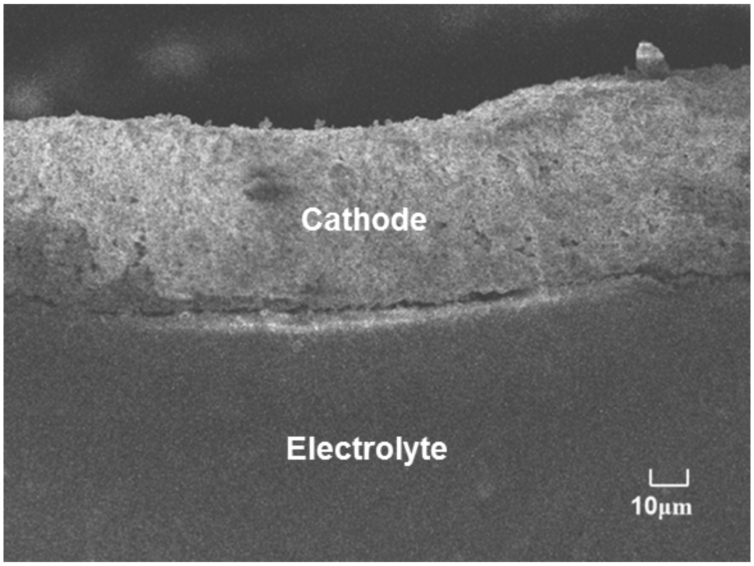

Figure 78 - Delamination occurring between electrode and electrolyte causing increases in ohmic resistance.

A closer inspection of the cathode reveals a relatively thick, porous GDC interlayer as well, suggesting that the sintering routine established for this component needs to be revised as well. Figure 79 shows the cathode and GDC interlayer. The larger grains close to the electrolyte interface are the GDC particles, which have undergone some grain growth but still remain somewhat porous, limiting ionic transport between the electrode and electrolyte. However, it should be noted that this interlayer was deposited using the GDC with SSA of $9.47m^2/g$ available at the NETL, rather than the GDC used at the home institution which the deposition routine was established for. Recalling section 4.2, the use of a powder with different properties can adversely affect microstructure and therefore cell performance. Specifically, this powder resulted in a thicker coating when using the same spin coating recipe. The porosity may possibly be related to this as well, as this powder's sintering behavior was not evaluated.

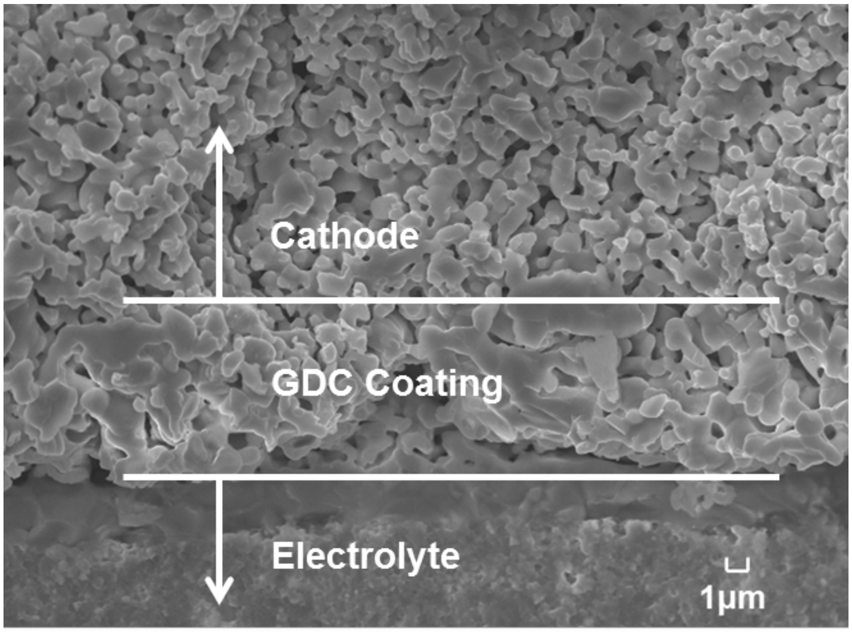

Figure 79 - Microstructure of cathode on 3YSZ cell showing incomplete densification of GDC.

Inspection of the anode reveals relatively poorly connected YSZ matrix within anode microstructure, suggesting too low of a content of YSZ. Figure 80 shows a micrograph of the anode where the Ni and YSZ phases can be distinctly differentiated by their size. The smaller grains are the YSZ and the larger, more continuous looking grains are the Ni. The YSZ in this micrograph exists mostly in segregated clusters spread throughout, rather than as a continuous matrix intertwined with the Ni matrix within the anode. This would limit fuel activity within the anode mostly to the TPB at the interface between the anode and the electrolyte, severely limiting overall cell performance.

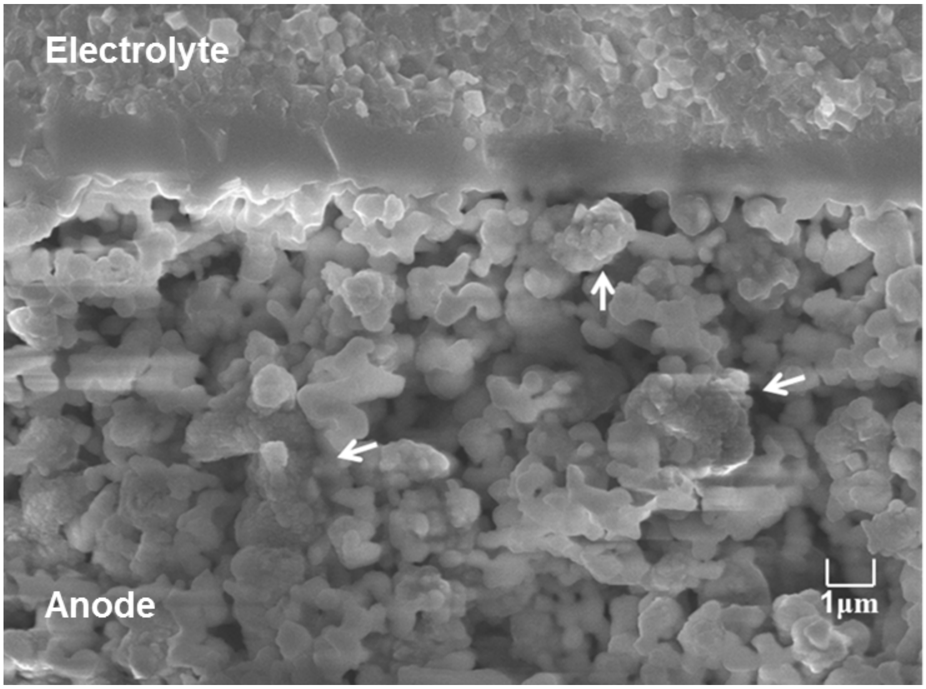

Figure 80 - Micrograph of anode with arrows indicating isolated clusters of 3YSZ.

CHAPTER 5: FUTURE WORK

As per the observations in Chapter 4 and some of the suggestions already made, there are some adjustments suggested here which could potentially increase the performance and durability of the single cells produced. These will be presented in the order that components are typically manufactured, with each change's potential to help the cell in one way or another explained.

Firstly, it is believed that the application of the intermediate layer of GDC to the electrolyte surface could be further refined to expedite the process, reducing both time and the amount of material used to reduce the overall cost. Firstly, when using the double-sintering method, it is believed that a fewer number of coatings could be used for each of the two applications. Rather than depositing 10 coatings and sintering twice, 5 and 7 layer coatings will be deposited each time. This will reduce the overall time consumed for coating each electrolyte and also reduces the amount of material used, lowering cost. Alternatively, the original single application and sintering routine which was established for 20mm electrolytes could be revisited and the ramp time modified to try and keep the suspension from spinning off too early, leaving a deposit throughout the entire diameter of the electrolyte rather than leaving an uncoated portion. Ramp times of 12-15 seconds would be tested to try to achieve this result, with each one being used 10 times on a single cell to compare overall deposit thickness and homogeneity. Using this single-coating method would also reduce cost, and both methods should also leave a slightly thinner coating, which is still thick enough to prevent the formation of insulating zirconates. The reduced thickness, however, will have a smaller contribution to overall cell resistances, increasing cell performance. These adjusted routines will be inspected by SEM to ensure thorough coverage of the electrolyte surface with GDC. At the same time, these micrographs will be used to ensure that the GDC coating is sintering to full density, rather than leaving behind a porous coating as shown in Figure 79. If the interlayer is seen to be porous after sintering, the sintering routine will be reevaluated using the same method which was used to determine the sintering temperatures of each of the other components.

The anode mixture tested seems to be inadequate for forming continuous intertwined matrices of both NiO and YSZ. Namely, the YSZ content appears to be too low, as Figure 80 shows clusters of YSZ within the anode, rather than a continuous matrix. To correct this, mixtures of 55 wt% NiO – 45 wt% YSZ and 50 wt% NiO – 50 wt% YSZ will be tested. This should create a better connected YSZ matrix intertwined with the NiO matrix, extending the effective TPB area further into the anode bulk and increasing overall cell performance due to an increase in fuel oxidation activity.

The cathode could also benefit from some refinement. As Figure 78 shows, the bond between the cathode and the electrolyte suffered during testing, suggesting weak bonding due to insufficient grain growth during sintering. Rectifying this would involve re-evaluating the sintering behavior, using a longer sintering period, an increased sintering temperature, or a combination of both to encourage grain growth. Inversely, this could also result in a decrease in porosity, which would negatively impact cell performance. Therefore, adjustment of the sintering routine would likely need to be combined with an adjustment in the electrode to pore former ratio, increasing the amount of pore former to maintain a high level of porosity.

Alternatively, composite LSCF-GDC cathodes could be tested to increase both the ionic conductivity and the bond between the cathode and the intermediate layer. Use of composite cathodes has also shown a decrease in overall cell resistances and increase cathode performance [103]. Composite mixtures such as 50-50 and 60-40 would be mixed, printed onto electrolytes, sintered, and examined microscopically.

CHAPTER 6: CONCLUSIONS

The purpose of this thesis was to develop a complete processing routine for manufacturing solid oxide fuel cells based on a high-performance layered YSZ/SCSZ composite electrolyte [39]. The processing techniques developed were based on popular SOFC manufacturing methods adjusted for the materials utilized in these cells. Layered electrolytes were produced by tape casting and lamination and sintered at 1500°C for 4 hours with 3 hour dwell periods at 300°C and 600°C for removal of binders, plasticizers, and dispersants. A thin layer of GDC was applied to one side of the electrolyte by spin coating, using a 10 second ramp to 2500rpm and applying 10 coatings before sintering at 1400°C, this was repeated twice for each sample to ensure thorough coverage of the entire electrolyte surface. Electrode inks were produced by 3-roll mill using a 60vol% electrode powder – 40 vol% carbon black pore former mixture as the powder mixture. The powder mixture was mixed in a 1:1 weight ratio with Hereaus V006 terpineol vehicle to produce a paste-like ink. Inks were subsequently applied by screen printer, drying each layer at 200°C for one hour. The anode is printed first and sintered at 1150°C and then the cathode is printed and sintered at 1000°C, as was determined using the density versus temperature graphs. Cell microstructures were inspected through the use of scanning electron microscopy of sputter coated cells. Performance tests were conducted at the Department of Energy's National Energy Technology Laboratory using custom built test stands to evaluate the V-I response of the cells and the impedance spectra of the cells after initial heat up to operating temperature and after 20h hours of run time. Both cell microstructures and performance evaluations confirm that the cells developed can produce electricity. However, performance of the cells was not very good and impedance was high. SEM inspection shows microstructural defects such as delamination and isolation of YSZ within the anode which contribute to the high cell resistances. The impedance is increased further after 20h of testing, indicating degradation mechanisms within the cell, such as the aforementioned delamination. Adjustments to manufacturing processes to eradicate these issues have been suggested, including reevaluation of some sintering routines, further refinement of the GDC interlayer spin coating recipe, and adjustments to electrode mixtures to increase phase connectivity and performance.

REFERENCES

[1] A. B. Stambouli and E. Traversa, "Solid oxide fuel cells (SOFCs): a review of an environmentally clean and efficient source of energy," *Renewable and Sustainable Energy Reviews,* vol. 6, pp. 433-455, 2002.

[2] S. Badwal, "Stability of solid oxide fuel cell components," *Solid State Ionics,* vol. 143, pp. 39-46, 2001.

[3] S. Singhal, "Advances in solid oxide fuel cell technology," *Solid State Ionics,* vol. 135, pp. 305-313, 2000.

[4] R. O'Hayre, S. W. Cha, W. Colella, and F. B. Prinz, *Fuel Cell Fundamentals*: John Wiley & Sons, 2009.

[5] N. Q. Minh, "Solid oxide fuel cell technology—features and applications," *Solid State Ionics,* vol. 174, pp. 271-277, 2004.

[6] C. Sun and U. Stimming, "Recent anode advances in solid oxide fuel cells," *Journal of Power Sources,* vol. 171, pp. 247-260, 2007.

[7] C. Sun, R. Hui, and J. Roller, "Cathode materials for solid oxide fuel cells: a review," *J Solid State Electrochem,* vol. 14, pp. 1125-1144, 2009.

[8] S. M. Haile, "Fuel cell materials and components," *Acta Materialia,* vol. 51, pp. 5981-6000, 2003.

[9] E. D. Wachsman and K. T. Lee, "Lowering the Temperature of Solid Oxide Fuel Cells," *Science,* vol. 334, pp. 935-939, November 18, 2011 2011.

[10] L. Carrette, K. A. Friedrich, and U. Stimming, "Fuel cells: Principles, types, fuels, and applications," *ChemPhysChem,* vol. 1, pp. 162-193, 2000.

[11] S. Singhal, S. C. Singhal, and K. Kendall, *High-temperature Solid Oxide Fuel Cells: Fundamentals, Design and Applications: Fundamentals, Design and Applications*: Elsevier Science, 2003.

[12] A. Atkinson, S. Barnett, R. J. Gorte, J. T. S. Irvine, A. J. McEvoy, M. Mogensen*, et al.*, "Advanced anodes for high-temperature fuel cells," *Nat Mater,* vol. 3, pp. 17-27, 2004.

[13] S. P. Jiang and S. P. S. Badwal, "Hydrogen Oxidation at the Nickel and Platinum Electrodes on Yttria-Tetragonal Zirconia Electrolyte," *Journal of The Electrochemical Society,* vol. 144, pp. 3777-3784, January 1, 1997 1997.

[14] S. Jiang and S. Chan, "A review of anode materials development in solid oxide fuel cells," *Journal of Materials Science,* vol. 39, pp. 4405-4439, 2004/07/01 2004.

[15] J. Hanna, W. Y. Lee, Y. Shi, and A. F. Ghoniem, "Fundamentals of electro- and thermochemistry in the anode of solid-oxide fuel cells with hydrocarbon and syngas fuels--a review " *Energy and Environmental Science,* vol. In review, 2012.

[16] Y. Shi, N. Cai, C. Li, C. Bao, E. Croiset, J. Qian*, et al.*, "Modeling of an anode-supported Ni–YSZ|Ni–ScSZ|ScSZ|LSM–ScSZ multiple layers SOFC cell: Part I. Experiments, model development and validation," *Journal of Power Sources,* vol. 172, pp. 235-245, 2007.

[17] T. Fukui, S. Ohara, M. Naito, and K. Nogi, "Performance and stability of SOFC anode fabricated from NiO–YSZ composite particles," *Journal of Power Sources,* vol. 110, pp. 91-95, 2002.

[18] S. Jiang, "Sintering behavior of Ni/Y2O3-ZrO2cermet electrodes of solid oxide fuel cells," *Journal of Materials Science,* vol. 38, pp. 3775-3782, 2003/09/01 2003.

[19] W. Zhu and S. Deevi, "A review on the status of anode materials for solid oxide fuel cells," *Materials Science and Engineering: A,* vol. 362, pp. 228-239, 2003.

[20] H. Sumi, Y. H. Lee, H. Muroyama, T. Matsui, and K. Eguchi, "Comparison Between Internal Steam and CO2 Reforming of Methane for Ni-YSZ and Ni-ScSZ SOFC Anodes," *Journal of The Electrochemical Society,* vol. 157, pp. B1118-B1125, 2010.

[21] F. Besenbacher, I. Chorkendorff, B. S. Clausen, B. Hammer, A. M. Molenbroek, J. K. Nørskov*, et al.*, "Design of a Surface Alloy Catalyst for Steam Reforming," *Science,* vol. 279, pp. 1913-1915, March 20, 1998 1998.

[22] S. P. Jiang, P. J. Callus, and S. P. S. Badwal, "Fabrication and performance of Ni/3 mol% Y2O3–ZrO2 cermet anodes for solid oxide fuel cells," *Solid State Ionics,* vol. 132, pp. 1-14, 2000.

[23] F. Tietz, H. P. Buchkremer, and D. Stöver, "Components manufacturing for solid oxide fuel cells," *Solid State Ionics,* vol. 152, pp. 373-381, 2002.

[24] M. Ni, M. K. H. Leung, and D. Y. C. Leung, "Micro-scale modelling of solid oxide fuel cells with micro-structurally graded electrodes," *Journal of Power Sources,* vol. 168, pp. 369-378, 2007.

[25] P. Holtappels, C. Sorof, M. C. Verbraeken, S. Rambert, and U. Vogt, "Preparation of Porosity–Graded SOFC Anode Substrates," *Fuel Cells,* vol. 6, pp. 113-116, 2006.

[26] M. Richards, E. Tang, R. Petri, "Solid Oxide Fuel Cell Manufacturing Overview," in *Hydrogen and Fuel Cell Technologies Manufacturing R&D Workshop*, Washington, D.C., 2011.

[27] N. Katsuhiro, "Intermediate Temperature Solid Conductors - Crystal Structure Gallery," ed. Kansai Center, Japan: National Institute of Advanced Inductrial Scrience and Technology, 2002.

[28] S. Sasaki, K. Fujino, and Y. Takeuchi, in *Proceedings of the Japan Academy. Ser. B: Physical and Biological Sciences*, Japan, 1979.

[29] F. M. L. Figueiredo and F. M. B. Marques, "Electrolytes for solid oxide fuel cells," *Wiley Interdisciplinary Reviews: Energy and Environment,* vol. 2, pp. 52-72, 2013.

[30] M. L. Faro and V. Antonucci, "Intermediate temperature solid oxide fuel cell electrolytes," *Journal of the Indian Institute of Science,* vol. 89, pp. 363-381, 2009.

[31] N. Sammes and Y. Du, "Intermediate-Temperature SOFC Electrolytes," *Fuel Cell Technologies: State and Perspectives,* pp. 19-34, 2005.

[32] M. Rühle, N. Claussen, A. C. Society, and A. H. Heuer, *Science and Technology of Zirconia*: American Ceramic Society, 1983.

[33] T. H. Estell and S. N. Flengas, "The Electrical Properties of Solid Oxide Electrolytes," *Chemical Review,* vol. 70, pp. 339-376, 1970.

[34] S. P. S. Badwal and K. Foger, "Solid oxide electrolyte fuel cell review," *Ceramics International,* vol. 22, pp. 257-265, 1996.

[35] S. Badwal and K. Foger, "Solid oxide electrolyte fuel cell review," *Ceramics International,* vol. 22, pp. 257-265, 1996.

[36] H. Fujimori, M. Yashima, M. Kakihana, and M. Yoshimura, "beta-cubic phase transition of scandia-doped zirconia solid solution: Calorimetry, x-ray diffraction, and Raman scattering," *Journal of Applied Physics,* vol. 91, pp. 6493-6498, 2002.

[37] Z. Wang, M. Cheng, Z. Bi, Y. Dong, H. Zhang, J. Zhang*, et al.*, "Structure and impedance of ZrO2 doped with Sc2O3 and CeO2," *Materials Letters,* vol. 59, pp. 2579-2582, 2005.

[38] J. Sankar, N. Bernier, M. Klimov, J. Kapat, and N. Orlovskaya, "Phase Stability and Sintering Behavior of 10 mol% Sc2 O3–1 mol% CeO2–ZrO2 Ceramics," *Journal of Fuel Cell Science and Technology MAY,* vol. 6, pp. 021007-1, 2009.

[39] Y. Chen, N. Orlovskaya, M. Klimov, X. Huang, D. Cullen, T. Graule*, et al.*, "Layered YSZ/SCSZ/YSZ Electrolytes for Intermediate Temperature SOFC Part I: Design and Manufacturing," *Fuel Cells,* vol. 12, pp. 722-731, 2012.

[40] M. L. Faro and V. Antonucci, "Intermediate temperature solid oxide fuel cell electrolytes."

[41] K. Eguchi, T. Setoguchi, T. Inoue, and H. Arai, "Electrical properties of ceria-based oxides and their application to solid oxide fuel cells," *Solid State Ionics,* vol. 52, pp. 165-172, 1992.

[42] A. McEvoy, "Thin SOFC electrolytes and their interfaces–: A near-term research strategy," *Solid State Ionics,* vol. 132, pp. 159-165, 2000.

[43] J. Drennan, V. Zelizko, D. Hay, F. T. Ciacchi, S. Rajendran, and S. P. Badwal, "Characterisation, conductivity and mechanical properties of theoxygen-ion conductor La0. 9Sr0. 1Ga0. 8Mg0. 2O3-x," *J. Mater. Chem.,* vol. 7, pp. 79-83, 1997.

[44] F. Zheng, R. K. Bordia, and L. R. Pederson, "Phase constitution in Sr and Mg doped LaGaO3 system," *Materials Research Bulletin,* vol. 39, pp. 141-155, 2004.

[45] F. Zheng and Y. Chen, "High temperature electrode reactions of Sr and Mg doped LaGaO3 perovskite," *Journal of Materials Science,* vol. 43, pp. 2058-2065, 2008/03/01 2008.

[46] M. Hrovat, A. Ahmad-Khanlou, Z. Samardžija, and J. Holc, "Interactions between lanthanum gallate based solid electrolyte and ceria," *Materials Research Bulletin,* vol. 34, pp. 2027-2034, 1999.

[47] K. Huang, J.-H. Wan, and J. B. Goodenough "Increasing Power Density of LSGM-Based Solid Oxide Fuel Cells Using New Anode Materials," *Journal of The Electrochemical Society,* vol. 148, pp. A788-A794, January 1, 2001 2001.

[48] N. M. Sammes, G. A. Tompsett, H. Näfe, and F. Aldinger, "Bismuth based oxide electrolytes— structure and ionic conductivity," *Journal of the European Ceramic Society,* vol. 19, pp. 1801-1826, 1999.

[49] R. E. Mistler and E. R. Twiname, *Tape Casting: Theory and Practice*: Wiley, 2000.

[50] J. Thijssen, "Solid Oxide Fuel Cells and Critical Materials: A Review of Implications," *Report for the National Energy Technology Laboratory,* 2011.

[51] "Doctor Blading," ed: Encyclopedia Brittanica, Inc., 1997.

[52] X. Xu, C. Xia, S. Huang, and D. Peng, "YSZ thin films deposited by spin-coating for IT-SOFCs," *Ceramics International,* vol. 31, pp. 1061-1064, // 2005.

[53] D. B. Hall, P. Underhill, and J. M. Torkelson, "Spin coating of thin and ultrathin polymer films," *Polymer Engineering & Science,* vol. 38, pp. 2039-2045, 1998.

[54] A. G. Emslie, F. T. Bonner, and L. G. Peck, "Flow of a Viscous Liquid on a Rotating Disk," *Journal of Applied Physics,* vol. 29, pp. 858-862, 1958.

[55] P. Bohac and L. Gauckler, "Chemical spray deposition of YSZ and GCO solid electrolyte films," *Solid State Ionics,* vol. 119, pp. 317-321, 1999.

[56] A. Princivalle and E. Djurado, "Nanostructured LSM/YSZ composite cathodes for IT-SOFC: A comprehensive microstructural study by electrostatic spray deposition," *Solid State Ionics,* vol. 179, pp. 1921-1928, 10/15/ 2008.

[57] T. Nguyen and E. Djurado, "Deposition and characterization of nanocrystalline tetragonal zirconia films using electrostatic spray deposition," *Solid State Ionics,* vol. 138, pp. 191-197, 1/1/ 2001.

[58] S. Giraud and J. Canel, "Young's modulus of some SOFCs materials as a function of temperature," *Journal of the European Ceramic Society,* vol. 28, pp. 77-83, 2008.

[59] Y. Chen, A. Aman, M. Lugovy, N. Orlovskaya, S. Wang, X. Huang*, et al.*, "Residual Stress and Biaxial Strength in Sc2O3-CeO2-ZrO2/Y2O3-ZrO2 Layered Electrolytes," *Fuel Cells,* vol. In review, Submitted 2013.

[60] M. Ghatee, M. Shariat, and J. Irvine, "Investigation of electrical and mechanical properties of 3YSZ/8YSZ composite electrolytes," *Solid State Ionics,* vol. 180, pp. 57-62, 2009.

[61] A. Mawson, G. Carter, R. Hart, N. Kirby, and A. Nachmann, "Mechanical Properties of 8 Mole% Yttria-Stabilised Zirconia for Solid Oxide Fuel Cells," in *MATERIALS FORUM*, 2006.

[62] T. Kushi, K. Sato, A. Unemoto, S. Hashimoto, K. Amezawa, and T. Kawada, "Elastic modulus and internal friction of SOFC electrolytes at high temperatures under controlled atmospheres," *Journal of Power Sources,* vol. 196, pp. 7989-7993, 2011.

[63] M. Yashima, T. Hirose, S. Katano, Y. Suzuki, M. Kakihana, and M. Yoshimura, "Structural changes of ZrO_{2}-CeO_{2} solid solutions around the monoclinic-tetragonal phase boundary," *Physical Review B,* vol. 51, pp. 8018-8025, 1995.

[64] R. J. Gaboriaud, F. Pailloux, P. Guerin, and F. Paumier, "Yttrium oxide thin films, Y 2 O 3 , grown by ion beam sputtering on Si," *Journal of Physics D: Applied Physics,* vol. 33, p. 2884, 2000.

[65] A. Gajović, N. Tomašić, I. Djerdj, D. S. Su, and K. Furić, "Influence of mechanochemical processing to luminescence properties in Y2O3 powder," *Journal of Alloys and Compounds,* vol. 456, pp. 313-319, 2008.

[66] U. Martin, H. Boysen, and F. Frey, "Neutron powder investigation of tetragonal and cubic stabilized zirconia, TZP and CSZ, at temperatures up to 1400 K," *Acta Crystallographica Section B,* vol. 49, pp. 403-413, 1993.

[67] V. Sadykov, G. Alikina, A. Lukashevich, V. Muzykantov, V. Usoltsev, A. Boronin*, et al.*, "Design and characterization of LSM/ScCeSZ nanocomposite as mixed ionic–electronic conducting material for functionally graded cathodes of solid oxide fuel cells," *Solid State Ionics,* vol. 192, pp. 540-546, 2011.

[68] A. Zevalkink, A. Hunter, M. Swanson, C. Johnson, J. Kapat, and N. Orlovskaya, "Processing and Characterization of Sc2O3-CeO2-ZrO2 Electrolyte Based Intermediate Temperature Solid Oxide Fuel Cells," in *MRS Proceedings*, 2006.

[69] S. B. Adler, J. A. Lane, and B. C. H. Steele, "Electrode Kinetics of Porous Mixed-Conducting Oxygen Electrodes," *Journal of The Electrochemical Society,* vol. 143, pp. 3554-3564, January 1, 1996 1996.

[70] J. Fleig, "Solid oxide fuel cell cathodes: Polarization mechanisms and modeling of the electrochemical performance," *Annual Review of Materials Research,* vol. 33, pp. 361-382, 2003.

[71] S. B. Adler, "Factors governing oxygen reduction in solid oxide fuel cell cathodes," 2004.

[72] J.-H. Wang, M. Liu, and M. C. Lin, "Oxygen reduction reactions in the SOFC cathode of Ag/CeO2," *Solid State Ionics,* vol. 177, pp. 939-947, 3/31/ 2006.

[73] S. J. Skinner, "Recent advances in Perovskite-type materials for solid oxide fuel cell cathodes," *International Journal of Inorganic Materials,* vol. 3, pp. 113-121, 2001.

[74] S. Jiang, "Development of lanthanum strontium manganite perovskite cathode materials of solid oxide fuel cells: a review," *Journal of Materials Science,* vol. 43, pp. 6799-6833, 2008/11/01 2008.

[75] S. P. Simner, J. F. Bonnett, N. L. Canfield, K. D. Meinhardt, J. P. Shelton, V. L. Sprenkle*, et al.*, "Development of lanthanum ferrite SOFC cathodes," *Journal of Power Sources,* vol. 113, pp. 1-10, 1/1/ 2003.

[76] E. Tsipis and V. Kharton, "Electrode materials and reaction mechanisms in solid oxide fuel cells: a brief review," *Journal of Solid State Electrochemistry,* vol. 12, pp. 1367-1391, 2008/11/01 2008.

[77] E. Tsipis and V. Kharton, "Electrode materials and reaction mechanisms in solid oxide fuel cells: a brief review. III. Recent trends and selected methodological aspects," *Journal of Solid State Electrochemistry,* vol. 15, pp. 1007-1040, 2011/05/01 2011.

[78] M. Levy, "Crystal Structure and Defect Properties in Ceramic Materials," PhD, Department of Materials, Imperial College London, 2005.

[79] J. J. Burton and R. L. Garten, *Advanced materials in catalysis*: Academic Press, 1977.

[80] G. Stochniol, E. Syskakis, and A. Naoumidis, "Chemical Compatibility between Strontium-Doped Lanthanum Manganite and Yttria-Stabilized Zirconia," *Journal of the American Ceramic Society,* vol. 78, pp. 929-932, 1995.

[81] V. V. Kharton, A. A. Yaremchenko, and E. N. Naumovich, "Research on the electrochemistry of oxygen ion conductors in the former Soviet Union. II. Perovskite-related oxides," *Journal of Solid State Electrochemistry,* vol. 3, pp. 303-326, 1999/08/01 1999.

[82] T. Ishihara, T. Kudo, H. Matsuda, and Y. Takita, "Doped PrMnO3 Perovskite Oxide as a New Cathode of Solid Oxide Fuel Cells for Low Temperature Operation," *Journal of The Electrochemical Society,* vol. 142, pp. 1519-1524, January 1, 1995 1995.

[83] A. Ringuedé and J. Fouletier, "Oxygen reaction on strontium-doped lanthanum cobaltite dense electrodes at intermediate temperatures," *Solid State Ionics,* vol. 139, pp. 167-177, 2001.

[84] A. Weber and E. Ivers-Tiffée, "Materials and concepts for solid oxide fuel cells (SOFCs) in stationary and mobile applications," *Journal of Power Sources,* vol. 127, pp. 273-283, 2004.

[85] M. Shiono, K. Kobayashi, T. Lan Nguyen, K. Hosoda, T. Kato, K. Ota*, et al.*, "Effect of CeO2 interlayer on ZrO2 electrolyte/La(Sr)CoO3 cathode for low-temperature SOFCs," *Solid State Ionics,* vol. 170, pp. 1-7, 5/14/ 2004.

[86] C. Rossignol, J. M. Ralph, J. M. Bae, and J. T. Vaughey, "Ln1−xSrxCoO3 (Ln=Gd, Pr) as a cathode for intermediate-temperature solid oxide fuel cells," *Solid State Ionics,* vol. 175, pp. 59-61, 11/30/ 2004.

[87] Z. Qingshan, J. Tongan, and W. Yong, "Thermal expansion behavior and chemical compatibility of BaxSr1−xCo1−yFeyO3−δ with 8YSZ and 20GDC," *Solid State Ionics,* vol. 177, pp. 1199-1204, 5// 2006.

[88] Z. Shao and S. M. Haile, "A high-performance cathode for the next generation of solid-oxide fuel cells," *Nature,* vol. 431, pp. 170-173, 2004.

[89] A. Zafar, Z. Imran, M. A. Rafiq, S. H. Shah, and M. M. Hasan, "Conduction in nanostructured La1−x Sr x FeO3 (0 ≤ x ≤ 1)," *Materials Science-Poland,* vol. 30, pp. 240-247, 2012/09/01 2012.

[90] V. V. Kharton, A. A. Yaremchenko, A. Shaula, A. Viskup, F. Marques, J. R. Frade*, et al.*, "Oxygen permeability and thermal expansion of ferrite-based mixed conducting ceramics," in *Defect and Diffusion Forum*, 2004, pp. 141-160.

[91] A. Mineshige, J. Izutsu, M. Nakamura, K. Nigaki, M. Kobune, S. Fujii*, et al.*, "Electrical property, crystal structure and oxygen nonstoichiometry of La1-xSrxCo0. 2Fe0. 8O3-delta," *Electrochemistry,* vol. 68, pp. 515-518, 2000.

[92] S. Wang, M. Katsukib, M. Dokiya, and T. Hashimoto, "High temperature properties of La0. 6Sr0. 4Co0. 8Fe0. 2O3Ād phase structure and electrical conductivity," *Solid State Ionics,* vol. 159, pp. 71-78, 2003.

[93] M. Katsuki, S. Wang, and T. Hashimoto, "High temperature properties of La0. 6Sr0. 4Co0. 8Fe0. 2O3-d oxygen nonstoichiometry and chemical diffusion constant," *Solid State Ionics,* vol. 156, pp. 453-462, 2003.

[94] H. Ullmann, N. Trofimenko, F. Tietz, D. Stöver, and A. Ahmad-Khanlou, "Correlation between thermal expansion and oxide ion transport in mixed conducting perovskite-type oxides for SOFC cathodes," *Solid State Ionics,* vol. 138, pp. 79-90, 2000.

[95] G. C. Kostogloudis and C. Ftikos, "Properties of A-site-deficient La0.6Sr0.4Co0.2Fe0.8O3−δ-based perovskite oxides," *Solid State Ionics,* vol. 126, pp. 143-151, 11/1/ 1999.

[96] A. Mineshige, J. Izutsu, M. Nakamura, K. Nigaki, J. Abe, M. Kobune*, et al.*, "Introduction of A-site deficiency into La0.6Sr0.4Co0.2Fe0.8O3–δ and its effect on structure and conductivity," *Solid State Ionics,* vol. 176, pp. 1145-1149, 3/31/ 2005.

[97] C. Endler, A. Leonide, A. Weber, F. Tietz, and E. Ivers-Tiffée, "Time-Dependent Electrode Performance Changes in Intermediate Temperature Solid Oxide Fuel Cells," *Journal of The Electrochemical Society,* vol. 157, pp. B292-B298, February 1, 2010 2010.

[98] T. Komatsu, H. Arai, R. Chiba, K. Nozawa, M. Arakawa, and K. Sato, "Cr poisoning suppression in solid oxide fuel cells using LaNi (Fe) O3 electrodes," *Electrochemical and solid-state letters,* vol. 9, pp. A9-A12, 2006.

[99] T. Komatsu, H. Arai, R. Chiba, K. Nozawa, M. Arakawa, and K. Sato, "Long-term chemical stability of LaNi (Fe) O3 as a cathode material in solid oxide fuel cells," *Journal of The Electrochemical Society,* vol. 154, pp. B379-B382, 2007.

[100] H. Orui, K. Watanabe, R. Chiba, and M. Arakawa, "Application of LaNi (Fe) O 3 as SOFC Cathode," *Journal of The Electrochemical Society,* vol. 151, pp. A1412-A1417, January 1, 2004 2004.

[101] C. N. Munnings, S. J. Skinner, G. Amow, P. S. Whitfield, and I. J. Davidson, "Oxygen transport in the La2Ni1−xCoxO4+δ system," *Solid State Ionics,* vol. 176, pp. 1895-1901, 7// 2005.

[102] S. J. Skinner, "Characterisation of La2NiO4+δ using in-situ high temperature neutron powder diffraction," *Solid State Sciences,* vol. 5, pp. 419-426, 3// 2003.

[103] E. Perry Murray, M. Sever, and S. Barnett, "Electrochemical performance of (La, Sr)(Co, Fe) O< sub> 3</sub>–(Ce, Gd) O< sub> 3</sub> composite cathodes," *Solid State Ionics,* vol. 148, pp. 27-34, 2002.

[104] X. Xu, C. Cao, C. Xia, and D. Peng, "Electrochemical performance of LSM–SDC electrodes prepared with ion-impregnated LSM," *Ceramics International,* vol. 35, pp. 2213-2218, 2009.

[105] P. Von Dollen and S. Barnett, "A Study of Screen Printed Yttria-Stabilized Zirconia Layers for Solid Oxide Fuel Cells," *Journal of the American Ceramic Society,* vol. 88, pp. 3361-3368, 2005.

[106] R. N. Basu, S. K. Pratihar, M. Saha, and H. S. Maiti, "Preparation of Sr-substituted LaMnO3 thick films as cathode for solid oxide fuel cell," *Materials Letters,* vol. 32, pp. 217-222, 9// 1997.

[107] Z. Liu, M. Liu, L. Nie, and M. Liu, "Fabrication and characterization of functionally-graded LSCF cathodes by tape casting," *International Journal of Hydrogen Energy,* vol. 38, pp. 1082-1087, 1/24/ 2013.

[108] Y. Leng, S. H. Chan, and Q. Liu, "Development of LSCF–GDC composite cathodes for low-temperature solid oxide fuel cells with thin film GDC electrolyte," *International Journal of Hydrogen Energy,* vol. 33, pp. 3808-3817, 2008.

[109] M. J. Jørgensen and M. Mogensen, "Impedance of Solid Oxide Fuel Cell LSM/YSZ Composite Cathodes," *Journal of The Electrochemical Society,* vol. 148, pp. A433-A442, January 1, 2001 2001.

[110] P. Holtappels and C. Bagger, "Fabrication and performance of advanced multi-layer SOFC cathodes," *Journal of the European Ceramic Society,* vol. 22, pp. 41-48, 2002.

[111] D.-H. Myung, J. Hwang, J. Hong, H.-W. Lee, B.-K. Kim, J.-H. Lee*, et al.*, "Pulsed Laser Deposition of La0.6Sr0.4CoO3−δ-Ce0.9Gd0.1O2−δ Nano-Composite and Its Application to Gradient-Structured Thin-film Cathode of SOFC," *Journal of The Electrochemical Society,* vol. 158, pp. B1000-B1006, January 1, 2011 2011.

[112] J. Peña-Martínez, D. Marrero-López, C. Sánchez-Bautista, A. J. D. Santos-García, J. C. Ruiz-Morales, J. Canales-Vazquez*, et al.*, *Effect of a CGO buffer layer on the performance of (La0.6Sr0.4)0.995Co0.2Fe0.8O3-delta cathode in YSZ-Based SOFC*, 2010.

[113] Y. Min Park and H. Kim, "Porous Gd-doped ceria barrier layer on solid oxide fuel cell with Sm0.5Sr0.5CoO3−δ Cathodes," *Ceramics International,* vol. 39, pp. 2037-2043, 3// 2013.

[114] S.-i. Hashimoto, Y. Fukuda, M. Kuhn, K. Sato, K. Yashiro, and J. Mizusaki, "Thermal and chemical lattice expansibility of La0.6Sr0.4Co1 − yFeyO3 − δ (y = 0.2, 0.4, 0.6 and 0.8)," *Solid State Ionics,* vol. 186, pp. 37-43, 2011.

[115] B. X. Huang, J. Malzbender, R. W. Steinbrech, E. Wessel, H. J. Penkalla, and L. Singheiser, "Mechanical aspects of ferro-elastic behavior and phase composition of La0.58Sr0.4Co0.2Fe0.8O3−δ," *Journal of Membrane Science,* vol. 349, pp. 183-188, 2010.

[116] B. X. Huang, J. Malzbender, R. W. Steinbrech, and L. Singheiser, "Mechanical properties of La0.58Sr0.4Co0.2Fe0.8O3-δ membranes," *Solid State Ionics,* vol. 180, pp. 241-245, 3/9/ 2009.

[117] D. S. Viswanath, *Viscosity of liquids : theory, estimation, experiment, and data*. Dordrecht: Springer, 2007.

[118] N. Rahaman, *Sintering of ceramics*: CRC Press, 2007.

[119] J. R. Macdonald and J. R. Macdonald, *Impedance spectroscopy : emphasizing solid materials and systems*. New York: Wiley, 1987.

[120] R. E. Chinn, *Ceramography : preparation and analysis of ceramic microstructures*. Materials Park, OH: ASM International, 2002.

[121] K. Yasuda, K. Uemura, and T. Shiota, "Sintering and mechanical properties of gadolinium-doped ceria ceramics," *Journal of Physics: Conference Series,* vol. 339, p. 012006, 2012.

[122] H. L. Lein, T. Tezuka, T. Grande, and M.-A. Einarsrud, "Asymmetric proton conducting oxide membranes and fuel cells prepared by aqueous tape casting," *Solid State Ionics,* vol. 179, pp. 1146-1150, 2008.

[123] K. Suresh Kumar Reddy, P. Kannan, A. Al Shoaibi, and C. Srinivasakannan, "Thermal Pyrolysis of Polyethylene in Fluidized Beds: Review of the Influence of Process Parameters on Product Distribution," *Journal of energy resources technology,* vol. 134, 2012.

[124] E. G. Grigor'yan, O. M. Niazyan, and S. L. Kharatyan, "Nickel oxide reduction under nonisothermal conditions," *Kinetics and Catalysis,* vol. 48, pp. 773-777, 2007/11/01 2007.

[125] S. Lee, N. Miller, and K. Gerdes, "Long-Term Stability of SOFC Composite Cathode Activated by Electrocatalyst Infiltration," *Journal of The Electrochemical Society,* vol. 159, pp. F301-F308, January 1, 2012 2012.

[126] X. J. Chen, K. A. Khor, and S. H. Chan, "Identification of O2 reduction processes at yttria stabilized zirconia|doped lanthanum manganite interface," *Journal of Power Sources,* vol. 123, pp. 17-25, 9/15/ 2003.

[127] A. Leonide, V. Sonn, A. Weber, and E. Ivers-Tiffée, "Evaluation and Modeling of the Cell Resistance in Anode-Supported Solid Oxide Fuel Cells," *Journal of The Electrochemical Society,* vol. 155, pp. B36-B41, January 1, 2008 2008.